



UNIVERSIDADE ESTADUAL DE CAMPINAS  
FACULDADE DE ENGENHARIA MECÂNICA  
E INSTITUTO DE GEOCIÊNCIAS

MARCO ANTONIO SALCEDO ARCINIEGA

**OPTIMIZATION OF THE PARAMETERS  
IN COMPLEX-PADÉ FOURIER  
FINITE-DIFFERENCE MIGRATION**

**OTIMIZAÇÃO DOS PARÂMETROS NA  
MIGRAÇÃO POR DIFERENÇAS FINITAS E  
FOURIER UTILIZANDO A EXPANSÃO  
DE PADÉ COMPLEXA**

CAMPINAS, SP  
2016

MARCO ANTONIO SALCEDO ARCINIEGA

**OPTIMIZATION OF THE PARAMETERS  
IN COMPLEX-PADÉ FOURIER  
FINITE-DIFFERENCE MIGRATION**

**OTIMIZAÇÃO DOS PARÂMETROS NA  
MIGRAÇÃO POR DIFERENÇAS FINITAS E  
FOURIER UTILIZANDO A EXPANSÃO  
DE PADÉ COMPLEXA**

Dissertation presented to the Mechanical Engineering Faculty and Geosciences Institute of the University of Campinas in partial fulfillment of the requirements for the degree of Master in Petroleum Sciences and Engineering in the area of Reservoirs and Management.

Dissertação apresentada à Faculdade de Engenharia Mecânica e Instituto de Geociências da Universidade Estadual de Campinas como parte dos requisitos exigidos para a obtenção do título de Mestre em Ciências e Engenharia de Petróleo na área de Reservatórios e Gestão.

Orientador: Profa. Dra. Maria Amélia Novais Schleicher

Este exemplar corresponde à versão final da Dissertação defendida pelo aluno Marco Antonio Salcedo Arciniega, e orientada pela Profa. Dra. Maria Amélia Novais Schleicher.



Assinatura do Orientador

CAMPINAS, SP  
2016

**Agência(s) de fomento e nº(s) de processo(s):** CAPES, 33003017

Ficha catalográfica  
Universidade Estadual de Campinas  
Biblioteca da Área de Engenharia e Arquitetura  
Elizangela Aparecida dos Santos Souza - CRB 8/8098

Sa31o Salcedo Arciniega, Marco Antonio, 1990-  
Optimization of the parameters in complex-Padé Fourier finite-difference migration / Marco Antonio Salcedo Arciniega. – Campinas, SP : [s.n.], 2016.

Orientador: Maria Amélia Novais Schleicher.  
Dissertação (mestrado) – Universidade Estadual de Campinas, Faculdade de Engenharia Mecânica e Instituto de Geociências.

1. Fourier, Transformações de - Processamento de dados. 2. Sistemas de imagens em geofísica. 3. Geofísica - Matemática. 4. Padé, Aproximação de. I. Schleicher, Maria Amélia Novais, 1967-. II. Universidade Estadual de Campinas. Faculdade de Engenharia Mecânica. III. Título.

Informações para Biblioteca Digital

**Título em outro idioma:** Otimização dos parâmetros na migração por diferenças finitas e Fourier utilizando a expansão de Padé complexa

**Palavras-chave em inglês:**

Fourier transformations - Data processing

Imaging systems in geophysics

Geophysics - Mathematics

Pade approximation

**Área de concentração:** Reservatórios e Gestão

**Titulação:** Mestre em Ciências e Engenharia de Petróleo

**Banca examinadora:**

Maria Amélia Novais Schleicher [Orientador]

Lúcio Tunes dos Santos

Daniela Rêgo Amazonas

**Data de defesa:** 20-06-2016

**Programa de Pós-Graduação:** Ciências e Engenharia de Petróleo

UNIVERSIDADE ESTADUAL DE CAMPINAS  
FACULDADE DE ENGENHARIA ELÉTRICA  
E INSTITUTO DE GEOCIÊNCIAS

DISSERTAÇÃO DE MESTRADO ACADÊMICO

**OPTIMIZATION OF THE PARAMETERS  
IN COMPLEX-PADÉ FOURIER  
FINITE-DIFFERENCE MIGRATION**

Autor: Marco Antonio Salcedo Arciniega

Orientador: Profa. Dra. Maria Amélia Novais Schleicher

A Banca Examinadora composta pelos membros abaixo aprovou esta Dissertação:

Profa. Dra. Maria Amélia Novais Schleicher  
DMA/IMECC/UNICAMP

Prof. Dr. Lúcio Tunes dos Santos  
DMA/IMECC/UNICAMP

Profa. Dra. Daniela Rêgo Amazonas  
Consultora Independente

A ata da defesa com as respectivas assinaturas dos membros encontra-se no processo de vida acadêmica do aluno.

Campinas, 20 de junho de 2016

*Dedico este trabajo a mis padres, Freddy y Cecilia, como un testimonio de cariño y eterno agradecimiento por el apoyo moral y estímulos brindados con infinito amor.  
Mis felicitaciones a ellos por el objetivo logrado.*

“Nada soy, nada valgo, nada pretendo, nada quiero para mi, todo para vosotros, que sois el pueblo que se ha hecho digno de ser libre”.

*José Eloy Alfaro Delgado*  
*President of Ecuador: 1897-1901 and 1907-1911*

# Acknowledgements

I would like to thank my advisors, Amélia Novais and Jörg Schleicher for their advice, and valuable directions during this work. Their guidance, academic confidence and all the support that I have received from them have been crucial during my study period in Brazil.

I also thank Jessé Costa and Lucio Santos for fruitful suggestions in my pre-defense.

I would like to specially thank Gustavo Gomes (Petrobras) for his constructive suggestions, for his availability, his contribution and his friendship during my thesis.

I would like to express my gratitude to Alexandre Camargo and Alan Souza for their suggestions, their advice and discussions during this work.

I thank all the members of LGC for good working environment and cooperation during this time. Special thanks to Thonia, Yuri, Otavio, Diego and Paulo for their wonderful friendship and for every happy time we spent together. I also thank Edwin Fagua from LGA for his great friendship, support and suggestions the last year of my thesis.

I would like to thank CAPES for the financial support.

# Resumo

A migração pelas diferenças finitas e Fourier utilizando a expansão de Padé complexa (CPFFD) é uma técnica que usa a equação de onda unidireccional e permite um melhor tratamento das ondas evanescentes que sua versão real. Da mesma forma que ocorre no método Real FFD, os parâmetros da migração CPFFD também podem ser otimizados para melhorar as imagens de refletores inclinados. A limitação para imagear refletores inclinados do FFD depende da variação do campo de velocidade. Nós mostramos uma aproximação de grande abertura angular para o operador de continuação unidireccional através de uma otimização do parâmetro mais importante e que é dependente da velocidade. Avaliamos a qualidade baseados na aproximação da relação de dispersão de diferentes funções considerando o número de termos da aproximação de Padé e o ângulo de rotação da linha de corte. Os parâmetros otimizados são escolhidos com base nos resultados da migração e dos custos computacionais. As implementações são validadas no modelo Marmousi e no modelo de sal SEG/EAGE.

**Palavras Chave:** Migração em profundidade, diferenças finitas e Fourier, expansão de Padé complexa, otimização de parâmetros, refletores inclinados.

# Abstract

Complex-Padé Fourier finite difference (CPFFD) migration is a one-way wave-equation technique that allows for a better treatment of evanescent modes than its real counterpart. As for real FFD migration, its parameters can be optimized in order to improve the imaging steeply dipping reflectors. The dip limitation of the FFD operator depends on the variation of the velocity field. We provide a wide-angle approximation for the one-way continuation operator by means of optimization of the most important velocity-dependent parameter. We discuss the achieved quality of the approximate dispersion relation for different functions under consideration of the number of terms in the Padé approximation and the branch-cut rotation angle. The optimized parameters are chosen based on the migration results and the computational cost. The implementations are validated on the Marmousi data set and SEG/EAGE salt model data.

**Key Word:** Depth migration, Fourier finite-difference, complex Padé approximation, parameter optimization, steep dips.

# List of Figures

2.1	Branch cut rotation angle in the complex plane . . . . .	26
3.1	Complex Padé approximations to the dispersion relation with branch-cut rotation angle of $\alpha = 5^\circ$ . . . . .	28
3.2	Complex Padé approximations to the dispersion relation with branch-cut rotation angle of $\alpha = 45^\circ$ . . . . .	28
3.3	Complex Padé approximations to the dispersion relation with branch-cut rotation angle of $\alpha = 90^\circ$ . . . . .	29
3.4	Relative error as a function of propagation angle. . . . .	30
3.5	Relative error as a function of propagation angle (detail). . . . .	31
3.6	Maximum dip angle with $N = 1$ for best possible values of $\sigma$ and different values of $\alpha$ . . . . .	32
3.7	Maximum dip angle with $N = 2$ for best possible values of $\sigma$ and different values of $\alpha$ . . . . .	33
3.8	Maximum dip angle with $N = 3$ for best possible values of $\sigma$ and different values of $\alpha$ . . . . .	33
3.9	Maximum dip angle with $\alpha = 10^\circ$ for best possible values of $\sigma$ and different values of $N$ . . . . .	34
3.10	Maximum dip angle with $\alpha = 25^\circ$ for best possible values of $\sigma$ and different values of $N$ . . . . .	35
3.11	Maximum dip angle with $\alpha = 30^\circ$ for best possible values of $\sigma$ and different values of $N$ . . . . .	36
3.12	Maximum dip angle with $\alpha = 35^\circ$ for best possible values of $\sigma$ and different values of $N$ . . . . .	36
3.13	Defining the optimal value of $\alpha$ to be used with 2 terms. . . . .	37
3.14	Optimized $\sigma$ compared with the theoretical and heuristical $\sigma$ functions using $\alpha = 10^\circ$ and $N = 1$ . . . . .	38
3.15	Optimized $\sigma$ compared with the theoretical and heuristical $\sigma$ functions using $\alpha = 27^\circ$ and $N = 2$ . . . . .	38
3.16	Maximum dip angles obtained with CPFFD using the optimized $\sigma$ compared with real FFD of Ristow and Rühl (1994). . . . .	39

3.17	Maximum dip-angle values as a function of $p$ and $\sigma$ for the complex Padé approximation using $\alpha = 10^\circ$ and $N = 1$ .	42
3.18	Dispersion relation with strong lateral velocity variation, $p = 0.25$ , $\alpha = 10^\circ$ and $N = 1$ .	42
3.19	Dispersion relation with intermediate lateral velocity variation, $p = 0.5$ , $\alpha = 10^\circ$ and $N = 1$ .	43
3.20	Dispersion relation with small lateral velocity variation, $p = 0.9$ , $\alpha = 10^\circ$ and $N = 1$ .	43
3.21	Relative error of optimized $\sigma$ , using intermediate lateral velocity variation, $p = 0.5$ .	44
3.22	Optimized $\sigma$ function versus least-squares.	45
3.23	Maximum dip-angle values as a function of $p$ and $\sigma$ for the complex Padé approximation using $\alpha = 27^\circ$ and $N = 2$ .	47
3.24	Dispersion relation with strong lateral velocity variation, $p = 0.25$ , $\alpha = 27^\circ$ and $N = 2$ .	47
3.25	Dispersion relation with intermediate lateral velocity variation, $p = 0.5$ , $\alpha = 27^\circ$ and $N = 2$ .	48
3.26	Dispersion relation with small lateral velocity variation, $p = 0.9$ , $\alpha = 27^\circ$ and $N = 2$ .	48
3.27	Relative error of optimized $\sigma$ , using intermediate lateral velocity variation, $p = 0.5$ .	49
3.28	Optimized $\sigma$ function versus our custom equation with $N = 2$ .	50
3.29	Maximum dip-angle values as a function of $p$ and $\sigma$ for the complex Padé approximation using $\alpha = 25^\circ$ and $N = 3$ .	52
3.30	Dispersion relation with strong lateral velocity variation, $p = 0.25$ , $\alpha = 25^\circ$ and $N = 3$ .	52
3.31	Dispersion relation with intermediate lateral velocity variation, $p = 0.5$ , $\alpha = 25^\circ$ and $N = 3$ .	53
3.32	Dispersion relation with small lateral velocity variation, $p = 0.9$ , $\alpha = 25^\circ$ and $N = 3$ .	53
3.33	Relative error of optimized $\sigma$ , using intermediate lateral velocity variation, $p = 0.5$ , $\alpha = 25^\circ$ and $N = 3$ .	54
3.34	Optimized $\sigma$ function versus our custom equation with $N = 3$ .	55
3.35	Marmousi velocity model.	56
3.36	Pre-SDM of Marmousi data set using optimized $\sigma$ , $N = 1$ , $\alpha = 5^\circ$ .	57
3.37	Pre-SDM of Marmousi data set using $\sigma$ from equation 3.4, $N = 1$ , $\alpha = 10^\circ$ .	57
3.38	Pre-SDM of Marmousi data set using optimized $\sigma$ , $N = 1$ , $\alpha = 15^\circ$ .	58
3.39	Pre-SDM of Marmousi data set using $\sigma = 1 + p^3$ , $N = 3$ , $\alpha = 45^\circ$ .	58
3.40	Pre-SDM of Marmousi data set using $\sigma$ from equation 3.5, $N = 2$ , $\alpha = 27^\circ$ .	59
3.41	A 2D slice of the SEG/EAGE salt model.	60
3.42	Pre-SDM from SEG/EAGE 2D data set using $\sigma = 1 + p^3$ , $N = 3$ and $\alpha = 45^\circ$ .	60
3.43	Pre-SDM from SEG/EAGE 2D data set using $\sigma$ from equation 3.4, $N = 1$ and $\alpha = 10^\circ$ .	61
3.44	Pre-SDM from SEG/EAGE 2D data set using $\sigma$ from equation 3.5, $N = 2$ and $\alpha = 27^\circ$ .	61

3.45	Color-coded image evaluating all the possible values of $a$ and $b$ . . . . .	63
3.46	Approximation of the real part . . . . .	63
3.47	Approximation of the square root, improving the imaginary part, first attempt, optimizing only alpha . . . . .	65
3.48	Approximation of the square root, improving the imaginary part, second attempt, optimizing alpha and beta . . . . .	66
3.49	Approximation of the square root, using the optimized $a$ and $b$ parameters, and the original complex Padé coefficients with $\alpha = 10^\circ$ . . . . .	67
3.50	Angles obtained with CPFFD using the optimized $\sigma$ , $a$ and $b$ , compared with last results and real FFD of Ristow and Rühl (1994). . . . .	68
3.51	Maximum dip-angle values as a function of $p$ and $\sigma$ for the complex Padé approximation using $\alpha = 10^\circ$ , $N = 1$ , $a$ and $b$ optimized. . . . .	70
3.52	Dispersion relation with strong lateral velocity variation, $p = 0.25$ , $a$ and $b$ optimized. . . . .	70
3.53	Dispersion relation with intermediate lateral velocity variation, $p = 0.5$ , $a$ and $b$ optimized. . . . .	71
3.54	Dispersion relation with small lateral velocity variation, $p = 0.9$ , $a$ and $b$ optimized. . . . .	71
3.55	Relative error of optimized $\sigma$ , using intermediate lateral velocity variation, $p = 0.5$ , $a$ and $b$ optimized. . . . .	72
3.56	Optimized $\sigma$ function versus least-squares using $a$ and $b$ optimized. . . . .	73
3.57	Pre-SDM of Marmousi data set using $\sigma$ from polynomial in equation 3.10, $N = 1$ , $\alpha = 10^\circ$ , and the optimized $a$ and $b$ parameters. . . . .	74
3.58	Pre-SDM of Marmousi data set using $\sigma$ from equation 3.4, $N = 1$ , $\alpha = 10^\circ$ . . . . .	75
3.59	Pre-SDM of Marmousi data set using $\sigma$ from equation 3.5, $N = 2$ , $\alpha = 27^\circ$ . . . . .	75
3.60	Pre-SDM of Marmousi data set using $\sigma = 1 + p^3$ , $N = 3$ , $\alpha = 45^\circ$ . . . . .	76
3.61	Pre-SDM of Marmousi data set using Real FFD and optimized $\sigma$ . . . . .	76
3.62	Pre-SDM from SEG/EAGE 2D data set using $\sigma$ from polynomial in equation 3.10, $N = 1$ , $\alpha = 10^\circ$ , and the optimized $a$ and $b$ parameters. . . . .	77
3.63	Pre-SDM from SEG/EAGE 2D data set using $\sigma$ from equation 3.5, $N = 2$ and $\alpha = 27^\circ$ . . . . .	77
3.64	Pre-SDM from SEG/EAGE 2D data set using $\sigma = 1 + p^3$ , $N = 3$ , $\alpha = 45^\circ$ . . . . .	78

# List of Tables

3.1	Maximum dip angle using the optimal value of $\sigma$ , $N = 1$ and $\alpha = 10^\circ$ . . . . .	41
3.2	Maximum dip angle using the optimal value of $\sigma$ , $N = 2$ and $\alpha = 27^\circ$ . . . . .	46
3.3	Maximum dip angle using the optimal value of $\sigma$ , $N = 3$ and $\alpha = 25^\circ$ . . . . .	51
3.4	Maximum dip angle using the optimal value of $\sigma$ , optimized $a$ and $b$ parameters and $\alpha = 10^\circ$ . . . . .	69

# Contents

<b>Aknowledgements</b>	<b>7</b>
<b>Resumo</b>	<b>8</b>
<b>Abstract</b>	<b>9</b>
<b>List of Figures</b>	<b>10</b>
<b>List of Tables</b>	<b>13</b>
<b>1 Introduction</b>	<b>16</b>
<b>2 Downward-continuation migration</b>	<b>18</b>
2.1 One-way wave equation . . . . .	18
2.2 Phase-Shift Migration . . . . .	20
2.3 Split-Step Migration . . . . .	21
2.4 Finite-Difference Migration . . . . .	22
2.5 Fourier Finite-Difference Migration . . . . .	23
2.6 Complex Padé Expansion and Complex FFD Migration . . . . .	24
<b>3 Numerical Evaluations</b>	<b>27</b>
3.1 Methodology . . . . .	27
3.2 Error Analysis . . . . .	29
3.3 Defining the number of terms in the Padé expansion . . . . .	31
3.4 Defining the optimal value of $\alpha$ . . . . .	34
3.5 Comparison to earlier results . . . . .	37
3.6 Studying the optimized $\sigma$ values . . . . .	40
3.6.1 Optimal value of $\sigma$ for $N = 1$ . . . . .	40
3.6.2 Simple function $\sigma(p)$ for $N = 1$ . . . . .	44

3.6.3	Optimal value of $\sigma$ for $N = 2$ . . . . .	45
3.6.4	Simple function $\sigma(p)$ for $N = 2$ . . . . .	49
3.6.5	Optimal value of $\sigma$ for $N = 3$ . . . . .	50
3.6.6	Simple function $\sigma(p)$ for $N = 3$ . . . . .	54
3.7	Rotation angle for one-term complex Padé approximation . . . . .	55
3.8	Optimization of one-term complex Padé approximation . . . . .	62
3.8.1	Optimized $\sigma$ for the one-term complex Padé approximation, using the optimized Padé coefficients . . . . .	67
3.8.2	Simple function $\sigma(p)$ for $N = 1$ , $\alpha = 10^\circ$ and using the optimized $a$ and $b$ parameters . . . . .	72
3.9	Migration results . . . . .	73
3.10	Final recommendation for CPFFD migration . . . . .	78
<b>4</b>	<b>Conclusions</b>	<b>79</b>
	<b>References</b>	<b>81</b>
<b>A</b>	<b>Definition of the complex Padé coefficients</b>	<b>83</b>

# 1. Introduction

Fourier finite-difference (FFD) migration (Ristow and Rühl, 1994) is an hybrid migration method, wherein the downward-continuation operator is split into three partial operators: one operator is a phase-shift operator for a chosen constant background velocity, the second one is a split-step correction of the vertical wave-propagation component for a weak lateral variation, and the third one is a finite-difference operator for the strongly varying component of the velocity field. The aim of this method is to generalize and improve the split-step approach by Stoffa et al. (1990) for strong lateral velocity variations using, in addition, a finite-difference correction term. In contrast to standard finite-difference (FD) migration schemes with a fixed maximum dip angle, in FFD migration this angle depends on the velocity field. While one-way wave-equation migration methods have gone out of fashion with the advent of more powerful computers that allow for a broad use of two-way methods, the use of one-way propagators is still of interest for modern methods like Marchenko imaging (Wapenaar et al., 2014).

Unfortunately, when the original FFD method is applied in the presence of sharp discontinuities in the velocity model, it can generate numerical instability (Biondi, 2002). Stability is a necessary condition for a migration method to be useful. Biondi (2002) was able to decompose the FFD operator in such a way that it no longer requires the use of reference velocities that do not exceed the minimum medium velocity, which is a necessary condition in the original FFD. This allows to use it in a Fourier finite-difference plus interpolation (FFDPI) method that combines the advantages of the FFD technique with the advantages of interpolation. The FFDPI method is stable even when the medium velocity has sharp discontinuities. Because its propagation step uses multiple velocities for interpolation, the computational cost of FFDPI is much higher than that of simple FFD. However, FFDPI achieves higher accuracy than simple FFD.

Another approach to improve the FFD method with regard to stability was presented by Amazonas et al. (2007). They reinterpreted the original FFD operator as the first term of a real Padé expansion (Bamberger et al., 1988). Because to the use of real Padé coefficients, Amazonas et al. (2007) called the original FFD method “real FFD”. This method implies in a real approximation of the square-root operator even for evanescent waves, where the dispersion relation should become complex. As a

consequence, evanescent waves, which should propagate horizontally with damping in the vertical direction, are propagated into the medium without amplitude decay, causing acausal precursors to the wavefield. These are the cause for instabilities and frequently lead to artifacts or even spurious reflectors in the migrated image.

For this reason, Amazonas et al. (2007) replaced the real Padé approximation by the complex one of Milinazzo et al. (1997). This approximation is obtained by rotating the branch cut from the negative real line into the lower complex plane. The resulting Complex-Padé Fourier finite-difference (CPFFD) propagator achieves a natural attenuation of the evanescent part of the mode spectrum. While still presenting a nonzero real part of the vertical wave-vector component at large values of the horizontal component, i.e., still propagating evanescent waves into the medium, these are now damped vertically. In this way, the migrated images of Amazonas et al. (2007) contain less artifacts, becoming of comparable quality as the images obtained with the much more expensive FFDPI of Biondi (2002).

Both the real and complex versions of FFD depend on a velocity-dependent parameter, denoted by  $b$  in Ristow and Rühl (1994) or by  $\sigma$  in Amazonas et al. (2007). In this work, we use the latter notation. Ristow and Rühl (1994) derived the theoretical expression for this parameter as a function of the ratio between the reference and model velocities. They also showed for a single term in the expansion that an optimized function  $\sigma$  further increases the imageable dips. The stronger attenuation of high-angle propagation of the CPFFD propagator leads to a reduced maximum-dip angle in the image. Amazonas et al. (2007) tried to solve this problem by using three terms in the complex Padé expansion and by heuristically changing the way  $\sigma$  depends on the velocity ratio. However, they did not carry out an optimization of the  $\sigma$  function.

In this work, we carry out such an optimization. We discuss the behavior of CPFFD migration in dependence on the selected function for  $\sigma$ , as well as on the branch-cut rotation angle and the number of terms used in the Padé approximation. We exhibit an optimized  $\sigma$  function for the best possible choices of the rotation angle and show that for certain ratios between the reference and model velocities, the best dip-angle behavior is achieved with a single Padé term similarly to real FFD (Ristow and Rühl, 1994), while for other values of that ratio, two terms are advantageous. As we will see below, higher-order terms in the Padé series cannot be used to increase the maximum-dip angle over the one achieved by an optimized single or two-term approximations. We validate the optimized parameters on synthetic data sets from the Marmousi and SEG/EAGE salt models.

## 2. Downward-continuation migration

Since downward-continuation methods are based on a recursive solution of the one-way equation, we start this chapter with the definition of this equation and its characteristics, being of utmost importance the single square-root and its proper approximation. Then, we provide a thorough overview of the numerical methods that have been developed for downward-continuing wavefields. We use the theory in Biondi (2006) to explain the phase-shift and split-step migration, for finite-difference and Fourier finite-difference migration we use the theory in Han (2000), and for complex Padé Fourier finite-difference migration the reader is referred to Amazonas et al. (2007).

### 2.1 One-way wave equation

Let us start with the 2-D acoustic wave equation, which describes propagation of a compressional wavefield  $P(x, z, t)$  in a medium with constant material density and compressional wave velocity  $v(x, z)$ :

$$\left( \frac{\partial^2}{\partial x^2} + \frac{\partial^2}{\partial z^2} - \frac{1}{v^2} \frac{\partial^2}{\partial t^2} \right) P(x, z, t) = 0, \quad (2.1)$$

where  $x$  is the horizontal spatial axis,  $z$  is the depth axis (positive downward), and  $t$  is the time. The wavefield can always be Fourier transformed over the time  $t$ . If there is no lateral velocity variation, then the wavefield can be also Fourier transformed over the horizontal axis  $x$ . Thus,

$$P(k_x, z, \omega) = \int \int P(x, z, t) e^{(-ik_x x - i\omega t)} dx dt, \quad (2.2)$$

where  $\omega$  is the temporal frequency and  $k_x$  is the wave number in the  $x$  direction. When the differential operator in 2.1 is applied to equation 2.2 we get

$$\begin{aligned} \frac{\partial^2}{\partial z^2} P(k_x, z, \omega) - \left( \left( \frac{i\omega}{v} \right)^2 - (ik_x)^2 \right) P(k_x, z, \omega) &= 0 \\ \frac{\partial^2}{\partial z^2} P(k_x, z, \omega) - \left( \frac{i\omega}{v} \right)^2 \left( 1 - \left( \frac{vk_x}{\omega} \right)^2 \right) P(k_x, z, \omega) &= 0 \\ \frac{\partial^2}{\partial z^2} P(k_x, z, \omega) = \left( \frac{i\omega}{v} \right)^2 \left( 1 - \left( \frac{vk_x}{\omega} \right)^2 \right) P(k_x, z, \omega). \end{aligned} \quad (2.3)$$

We know the definition of a plane wave  $P = e^{i(\omega t \pm k_x x \pm k_z z)}$  with its first and second derivative are:

$$\frac{\partial P}{\partial z} = \pm ik_z P(k_x, z, \omega), \quad (2.4)$$

$$\frac{\partial^2 P}{\partial z^2} = \pm (ik_z)^2 P(k_x, z, \omega). \quad (2.5)$$

Here the  $\pm$  signs are for the downward and upward propagating wavefields, respectively. Substituting equation 2.5 in 2.3 the vertical wavenumber can be expressed by the following dispersion relation, which is often called the Single Square Root (SSR) equation:

$$k_z = SSR(k_x, \omega) = -\sqrt{\frac{\omega^2}{v^2} - k_x^2} = -\frac{\omega}{v} \sqrt{1 - \left( \frac{vk_x}{\omega} \right)^2}. \quad (2.6)$$

The minus sign in front of the square root means that we want to downward continue upward-propagating waves, in accordance with the sign convention of Claerbout (1985). By substituting equation 2.6 into equation 2.4, the one-way acoustic wave equation in the  $k_x$ - $\omega$  domain reads:

$$\frac{\partial P(k_x, z, \omega)}{\partial z} = -\frac{i\omega}{v} \sqrt{1 - \left( \frac{vk_x}{\omega} \right)^2} P(k_x, z, \omega). \quad (2.7)$$

Chapter 5 in Biondi (2006) presents a detailed overview of several methods that have been proposed to approximate equation 2.6.

## 2.2 Phase-Shift Migration

When the propagation velocity is assumed to be a function only of depth, the wavefield can be downward-continued efficiently in the frequency-wavenumber  $\omega$ - $k$  domain by simple multiplication with the SSR downward-continuation operator

$$P(k_x, z, \omega) = P(k_x, 0, \omega) e^{-\frac{i\omega}{v} \sqrt{1 - \left(\frac{vk_x}{\omega}\right)^2} z}. \quad (2.8)$$

The downward-continuation operator expressed in equation 2.8 describes a dip-dependent  $k_x/\omega$  phase shift of the wavefield; thus, it often is called the phase-shift operator (Gazdag, 1978). When the medium velocity is strictly a function of depth, application of equation 2.8 downward-continues the data without any approximation of the kinematics of waves propagating along one direction with respect to the vertical axis. (Depending on the sign of the exponential function, the waves can propagate either upward or downward). However, the effects that velocity variations along the depth direction exert on geometric spreading are not taken into account correctly by the phase-shift operator, and consequently the amplitudes of the downward-continued wavefield are not correct. For details, see Amazonas et al. (2010).

In order to handle lateral velocity variations, Gazdag and Sguazzero (1984) proposed an approach, known as the phase-shift plus interpolation (PSPI) method. It uses the central features of the phase-shift method. Instead of only one velocity at each depth step, they made use of several reference velocities to account for the lateral velocity variation. The true wavefield is obtained by linearly interpolating the reference wavefields based on the relationship of the local velocity to the reference velocities. Up to a limit, the accuracy of PSPI downward continuation can be increased at will simply by increasing the number of reference velocities (Biondi, 2006).

## 2.3 Split-Step Migration

A more elegant approach to improve wave simulation in the presence of lateral velocity variations was provided by split-step migration (Stoffa et al., 1990). The application of a split-step correction can be interpreted as application of a first-order (with respect to velocity perturbations) correction operator to the phase-shift operator. Instead of using multi-reference velocities to propagate the wavefield, split-step uses only one reference velocity, which can be an average velocity, the minimum velocity, the root-mean-square velocity or an inverse of the average of the slowness at each depth step. The choice of the reference velocity among these alternatives is not critical for the migration results. Split-step downward continuation is based on the following approximation of the SSR equation:

$$k_z = SSR(k_x, \omega) \approx \left( \sqrt{\frac{\omega^2}{v_{ref}^2} - k_x^2} \right) + \left( \frac{\omega}{v(x, z)} - \frac{\omega}{v_{ref}} \right), \quad (2.9)$$

where  $v_{ref}$  is called the reference velocity. The operator implementing the first term in expression 2.9 is applied in the  $\omega$ - $k$  domain, whereas the second term represents a spatially varying time shift that easily can be applied in the  $\omega$ - $x$  domain.

At every depth step, the wavefield first is transformed into the wavenumber domain by a forward FFT (Fast Fourier Transform). The transformed wavefield then is downward-propagated with the SSR operator, on the assumption that the velocity is constant and equal to the reference velocity. The subsequent, spatially varying time shift corrects for (at least to first order) the discrepancies between the reference velocity and the medium's actual velocity.

The steeper the reflections and the stronger the lateral variations in velocity are, the greater the error introduced by the split-step operator is. The accuracy of split-step migration can be improved by using more than one reference velocity. In such a modified scheme, often called split-step plus interpolation (SSPI) migration (Kessinger, 1992), the number of reference wavefields generated equals the number of reference velocities used. A single wavefield is estimated then at each depth step by an interpolation in the space domain of the reference wavefields corresponding to all reference velocities. If the velocity variations are large, several reference velocities are needed to achieve accurate results.

## 2.4 Finite-Difference Migration

Unlike the phase-shift migration method, the FD method (Claerbout, 1985) works in the frequency-space domain, thus making it suitable to handle stronger lateral velocity variations. In deriving the FD method, one starts again from the one-way acoustic wave equation 2.7 in the frequency-wavenumber domain and approximates the Single Square Root 2.6 with continued fractions

$$\sqrt{1 - X^2} \approx 1 - \frac{X^2}{2 - \frac{X^2}{2}}. \quad (2.10)$$

This is the second-order approximation, where  $X = \frac{v_{ref} k_x}{\omega}$ . Using the inverse Fourier transform  $k_x^2 \iff -\frac{\partial^2}{\partial x^2}$ , we get the so-called 45° approximation of the one-way wave equation.

$$\begin{aligned} \frac{\partial P(x, z, \omega)}{\partial z} &\approx -\frac{\omega}{v(x, z)} \sqrt{1 + \frac{v(x, z)^2}{\omega^2} \frac{\partial^2}{\partial x^2}} P(x, z, \omega) \\ &\approx -\frac{\omega}{v(x, z)} \left( 1 + \frac{0.5 \frac{v(x, z)^2}{\omega^2} \frac{\partial^2}{\partial x^2}}{1 + 0.25 \frac{v(x, z)^2}{\omega^2} \frac{\partial^2}{\partial x^2}} \right) P(x, z, \omega). \end{aligned} \quad (2.11)$$

Now, as equation 2.11 is in the frequency-space  $\omega$ - $x$  domain,  $v$  can freely take the form  $v(x, z)$ ; i.e., velocity can vary from one grid cell of the model to another. Note that  $P$  is multiplying two terms. The first factor  $i\frac{\omega}{v}$  is solved analytically and the other factor is solved by finite differences. Based on the implicit finite-difference approximation, the second term is formulated into a tridiagonal linear system that can be solved efficiently by the Crank-Nicolson method (Claerbout, 1985). The cost of solving a tridiagonal system is substantially smaller than that of solving the full banded system, because the width of the diagonal band is only three.

Because we used only the second-order continued-fractions approximation, the implicit FD method is accurate for dips up to about only 45°. Therefore, operator 2.11 is often called 45°-migration. The structure of the continued-fractions approximation further makes it hard to implement high-order approximations efficiently. On the other hand, many situations require that migration handle dips beyond 45°.

The implicit Finite-Difference method has the important theoretical and practical advantage of being unconditionally stable when the velocity functions (the reference velocity and the medium's velocity) are smooth. However, numerical instability may arise when either of the velocity functions has sharp discontinuities (Ristow and Rühl, 1994).

## 2.5 Fourier Finite-Difference Migration

Ristow and Rühl (1994) introduced the Fourier finite-difference method as an extension of the split-step Fourier method. In addition to the split-step operator, an adaptive FD operator is introduced into the wave-propagator. The expression for the SSR equation is:

$$\sqrt{\frac{\omega^2}{v(x, z)^2} - k_x^2} = A + B + C, \quad (2.12)$$

with

$$\begin{aligned} A &= \sqrt{\frac{\omega^2}{v_{ref}^2} - k_x^2}, \\ B &= \left( \frac{\omega}{v(x, z)} - \frac{\omega}{v_{ref}} \right), \\ C &= -\frac{\omega}{v(x, z)} \left( 1 - \frac{v_{ref}}{v(x, z)} \right) \frac{\frac{v(x, z)^2}{\omega^2} k_x^2}{a - b \frac{v(x, z)^2}{\omega^2} k_x^2}. \end{aligned}$$

Here  $v_{ref}$  is a reference velocity and should be chosen to be the minimum velocity along the layer  $(z, z + \Delta z)$  i.e.,  $v_{ref} \leq v(x, z)$ . With  $a$  set to 2 and  $b = \frac{1}{2} \left[ 1 + \frac{v_{ref}}{v(x, z)} + \frac{v_{ref}^2}{v(x, z)^2} \right]$ .

The approximation is made in two steps. The first is  $A$  which represents the downward continuation with a reference velocity and is applied in the  $\omega$ - $k$  domain. The second step is  $B + C$ , where  $B$  is the split-step correction and is applied as a simple phase shift in the  $\omega$ - $x$  domain, and  $C$  is also applied in the  $\omega$ - $x$  domain as an implicit finite-difference operator.

The  $C$  factor is a higher-order term that improves the accuracy of the approximated dispersion relationship in the FFD algorithm.  $C$  can also be formulated as a tridiagonal linear system and solved by a Crank-Nicolson method (Claerbout, 1985). The  $b$  coefficient is adapted to the velocity variation in the FFD method because it depends on both the actual propagation velocity  $v(x, z)$  and the reference velocity  $v_{ref}$ .

As shown by Ristow and Rühl (1994), conventional FFD schemes become unstable if  $\frac{v_{ref}}{v(x, z)} > 1$ . Biondi (2002) was able to overcome that problem by an intelligent symmetrical decomposition of the operator in term  $C$ .

FFD has three different cases:

1. No lateral velocity variation: in this case,  $v(x, z) = v_{ref}$ , then automatically operators  $B$  and  $C$  vanish and a simple phase shift migration results.
2. Very strong lateral velocity variation: in this case,  $v_{ref} \ll v(x, z)$ , then (assuming  $v_{ref} \approx 0$ ) the phase-shift operator  $A$  becomes  $\omega/v(x, z)$  and a pure finite-difference operator remains:

$$\frac{\omega}{v(x, z)} \left( 1 - \frac{\frac{v(x, z)^2}{\omega^2} k_x^2}{a - b \frac{v(x, z)^2}{\omega^2} k_x^2} \right).$$

3. Intermediate lateral velocity variation,  $0 < v_{ref}/v(x, z) < 1$ .

## 2.6 Complex Padé Expansion and Complex FFD Migration

The target of all these methods is the approximation of the Single Square Root 2.6, i.e. approximations of the function  $\sqrt{1 - X^2}$ , where  $X = \frac{vk_x}{\omega}$ . The approximation of this operator is based on rational approximations of the form

$$\sqrt{1 - X^2} \approx 1 - \sum_{n=1}^N \frac{a_n X^2}{1 - b_n X^2}. \quad (2.13)$$

They provide good estimates for use in the one-way wave equation 2.7 and allow efficient numerical implementations. Equation 2.13 is the formal representation for the operator in a laterally inhomogeneous medium (Bamberger et al., 1988). Here the real-valued coefficients

$$a_n = \frac{2}{2N + 1} \sin^2 \left( \frac{n\pi}{2N + 1} \right) \quad \text{and} \quad b_n = \cos^2 \left( \frac{n\pi}{2N + 1} \right), \quad (2.14)$$

correspond to Padé approximations of the Single Square Root with branch cut along the positive real line from  $X = 1$ .

Amazonas et al. (2007) reinterpreted the original FFD using the first term of the real Padé expansion. They divided both the numerator and the denominator by 2 in the finite-difference operator, i.e., the  $C$  factor in equation 2.12. Because of the use of real Padé coefficients, they called the FFD method “real FFD”, described by

$$p\sqrt{1 - X^2} \approx \sqrt{1 - p^2 X^2} + (p - 1) - \frac{p(1 - p)a_1 X^2}{1 - b_1 \sigma X^2}, \quad (2.15)$$

where  $a_1$  and  $b_1$  are the Padé coefficients with  $n = N = 1$ , i.e.,  $a_1 = 1/2$  and  $b_1 = 1/4$ . Moreover,  $p = \frac{v_{ref}}{v(x,z)}$  (Ristow and Rühl, 1994) is the ratio between the actual propagation velocity  $v(x, z)$  and the propagation velocity in a homogeneous background medium  $v_{ref}$ , and  $\sigma = 1 + p + p^2$  in the notation of Amazonas et al. (2007).

The real-valued coefficients given in equation 2.14, while useful for certain problems, result in a square-root approximation which maps the real axis onto itself. In equation 2.13 if  $X > 1$ , the left side is a purely imaginary number but the right side remains a real-valued quantity. In other words the approximation breaks down. In the context of wave propagation, this leads to inappropriate treatment of eigenvalues corresponding to evanescent modes in acoustic media. This difficulty can be overcome by using complex coefficients.

According to (Milinazzo et al., 1997), the Single Square Root 2.6 can be approximated using the complex Padé series

$$\sqrt{1 - X^2} \approx R_{\alpha,N}(X^2) = C_0 - \sum_{n=1}^N \frac{A_n X^2}{1 - B_n X^2}, \quad (2.16)$$

where

$$A_n = \frac{a_n e^{-\frac{i\alpha}{2}}}{[1 + b_n(e^{-i\alpha} - 1)]^2}, \quad B_n = \frac{b_n e^{-i\alpha}}{1 + b_n(e^{-i\alpha} - 1)},$$

and

$$C_0 = e^{i\frac{\alpha}{2}} \left[ 1 + \sum_{n=1}^N \frac{a_n(e^{-i\alpha} - 1)}{[1 + b_n(e^{-i\alpha} - 1)]} \right].$$

The complex Padé approximation allows a better treatment of evanescent modes by rotating the branch cut of the square root in the complex plane by an angle  $\alpha$  (Appendix A). Figure 2.1 shows the rotation of the branch cut in the complex plane.

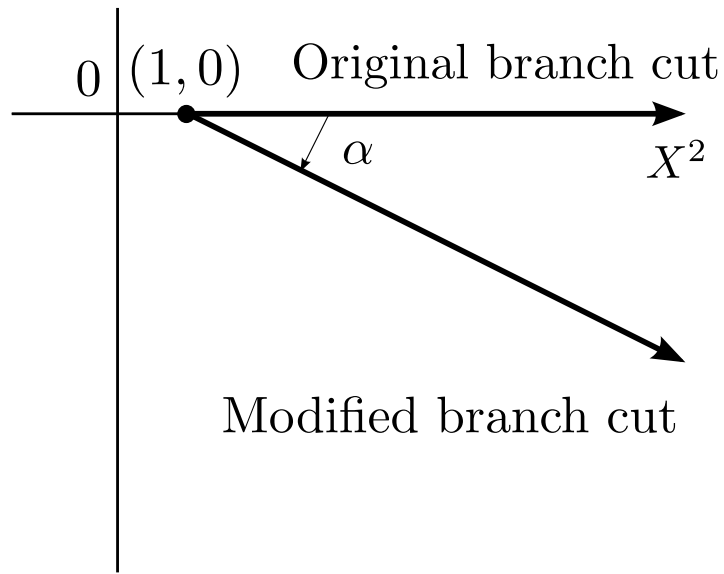


Figure 2.1: Branch cut rotation angle in the complex plane

Furthermore,  $C_0$  turns out to be a sophisticated approximation to one that gets the better the more terms  $N$  are used. Therefore, it can be directly replaced by  $C_0 = 1$  (Costa et al., 2011).

The complex-Padé Fourier finite-difference (CPFFD) algorithm is deduced following the derivation proposed by Ristow and Rühl (1994). The final result is (Amazonas et al., 2007)

$$p\sqrt{1 - X^2} \approx \sqrt{1 - p^2 X^2} + (p - 1) - \sum_{n=1}^N \frac{p(1 - p)A_n X^2}{1 - B_n \sigma X^2}. \quad (2.17)$$

As numerically demonstrated by Amazonas et al. (2007), this Complex-Padé approximation results in a better representation of the evanescent part of the mode spectrum than its real counterpart.

## 3. Numerical Evaluations

There are three important parameters to choose when implementing a CPFFD migration. These are the branch-cut rotation angle  $\alpha$ , the number of terms in the Padé expansion, and the function  $\sigma$ . Below we discuss the influence of these parameters on the dispersion relation. The optimized parameters are chosen based on the migration results and the computational cost. The implementations are validated on the Marmousi data set and SEG/EAGE salt model data.

### 3.1 Methodology

The Single Square Root in equation 2.6 may be written as

$$\frac{k_z v}{\omega} = \sqrt{1 - \left(\frac{v k_x}{\omega}\right)^2}, \quad (3.1)$$

thus being easily related with the familiar definition  $\cos \theta = \sqrt{1 - (\sin \theta)^2}$ , where  $\theta$  is the phase angle or the propagation angle, measured against the vertical, with which a plane-wave propagates through the medium. Using this relation, the CPFFD approximation reads

$$\cos \theta \approx \frac{\sqrt{1 - (p \sin \theta)^2}}{p} + \frac{(p - 1)}{p} - \sum_{n=1}^N \frac{(1 - p) A_n (\sin \theta)^2}{1 - B_n \sigma (\sin \theta)^2}. \quad (3.2)$$

Before the optimization we shall first show the results of Amazonas et al. (2007) to evaluate the quality of the CPFFD approximation by means of a comparison of its dispersion relation to that of the exact operator. In their numerical tests, they assumed a rather large deviation of  $p = 0.5$  and 3 terms in the complex Padé expansion. Figures 3.1, 3.2 and 3.3 show the corresponding comparison of dispersion relation in equation 3.2 using the CPFFD approximation for the downward-continuation operator with three different rotation angles  $\alpha$  of  $5^\circ$ ,  $45^\circ$  and  $90^\circ$ , respectively. We show the results using two different values of  $\sigma$ :  $\sigma = 1 + p + p^2$  (standard approximation of Ristow and Rühl (1994)) and  $\sigma = 1 + p^3$  (heuristic wide-angle approximation of Amazonas et al. (2007)).

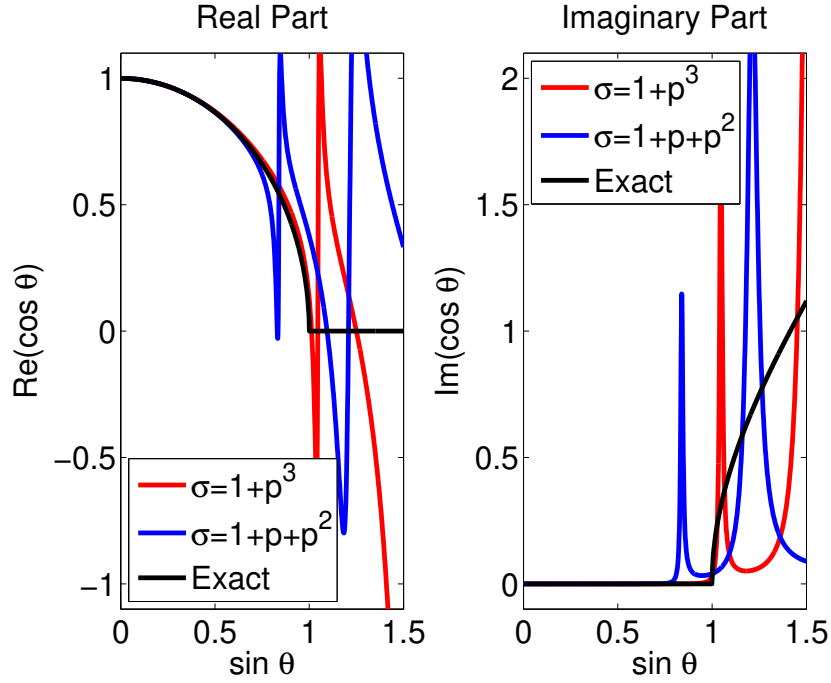


Figure 3.1: Complex Padé approximations to the dispersion relation with branch-cut rotation angle of  $\alpha = 5^\circ$ .

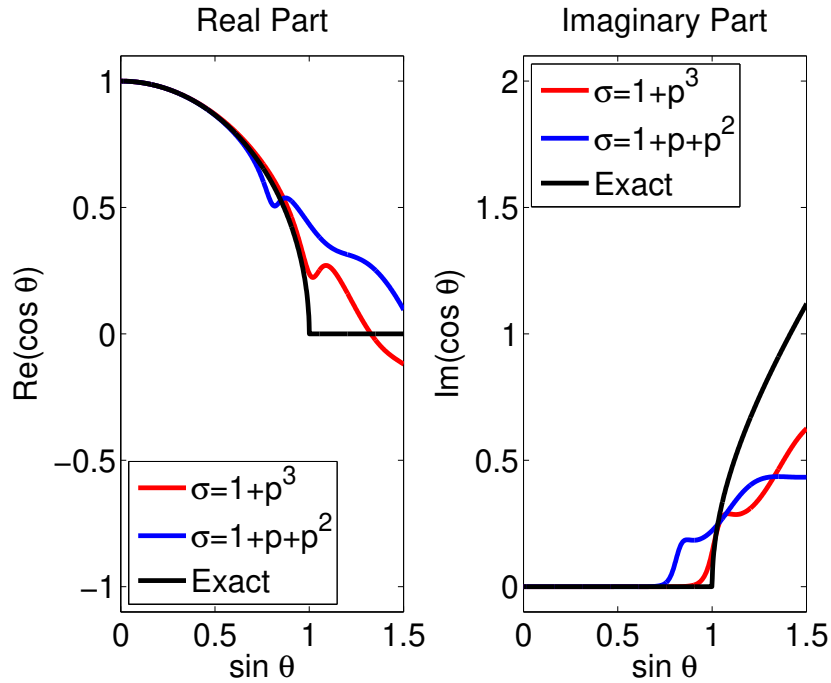


Figure 3.2: Complex Padé approximations to the dispersion relation with branch-cut rotation angle of  $\alpha = 45^\circ$ .

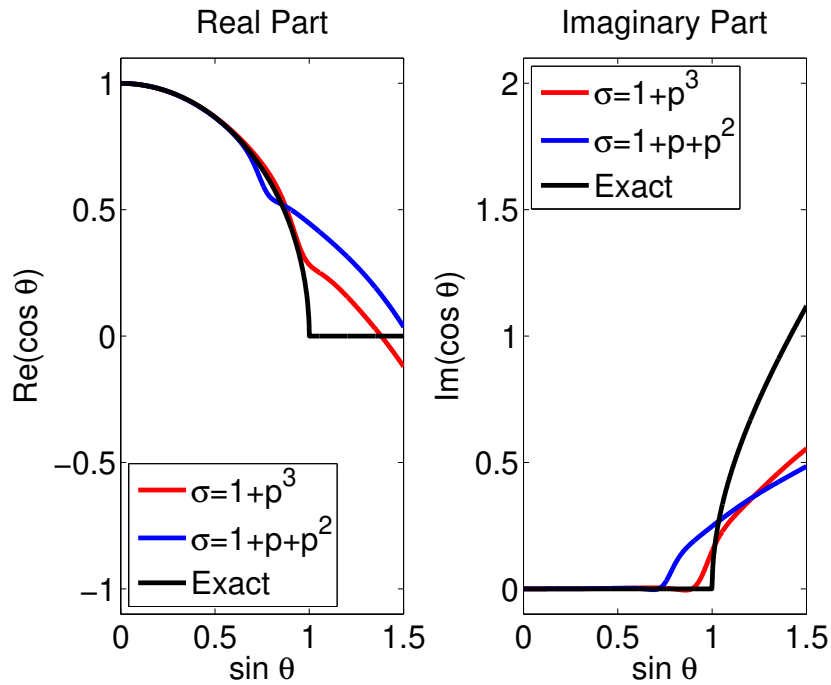


Figure 3.3: Complex Padé approximations to the dispersion relation with branch-cut rotation angle of  $\alpha = 90^\circ$ .

From this analysis, Amazonas et al. (2007) concluded that the best rotation angle was  $45^\circ$ , and they recommended  $\sigma = 1 + p^3$  over the theoretical function  $\sigma = 1 + p + p^2$  to reach higher dip angles. However, as we will see below, there are better functions  $\sigma$ , and for those, the choice of the rotation angle must be revisited.

## 3.2 Error Analysis

To find the optimal choice for the CPFFD parameters, we follow the fairly simple idea proposed by Ristow and Rühl (1994). Basically, we systematically study the relative error behavior for a series of values of  $\sigma$  for each chosen but fixed value of  $p$ . Since the tolerable positioning error of migration is often associated with one percent error of the dispersion relation (Ristow and Rühl, 1994), we look for a combination of parameters that will maximize the dip angle where this error of one percent occurs.

The relative error is defined by

$$E(X) = E(\sin \theta) = \frac{\varepsilon}{\sqrt{1 - \left(\frac{k_x v}{\omega}\right)^2}} * 100, \quad (3.3)$$

where  $\varepsilon$  is the difference between the square root and its approximation. The maximum dip angle  $\theta_m$  of a migration operator is then defined as that angle that gives a relative error of one percent,  $E(\sin \theta_m) = 0.01$ .

Figure 3.4 is the relative error plotted versus  $\sin \theta$  and the horizontal lines indicate an error of  $\pm 1\%$ . The first intersection of one of these lines with the error curve is often taken as a reasonable value of the maximum angle of accurate wave propagation with tolerable error.

Figures 3.4 and 3.5 (detail) show the relative error for  $\sigma = 1 + p^3$  and  $p = 0.5$ . Here the intersection with the one-percent error line gives us a value of  $\sin \theta = 0.6285$ , which corresponds to a maximum dip angle of  $\theta = 38.94^\circ$ . In the work of Amazonas et al. (2007), all tests were done with  $\alpha = 45^\circ$  and  $N = 3$ . Our goal is to find the optimized  $\sigma$  values for all the different values of  $p$ . Using these results we can find the best option for the branch-cut rotation angle  $\alpha$  and the number of  $N$  terms in the Padé expansion.

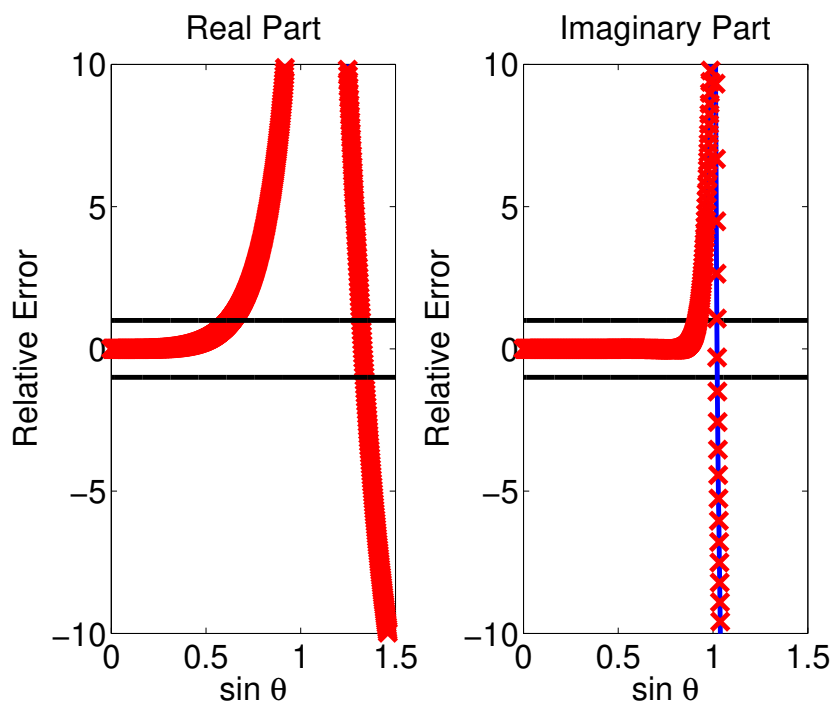


Figure 3.4: Relative error as a function of propagation angle.

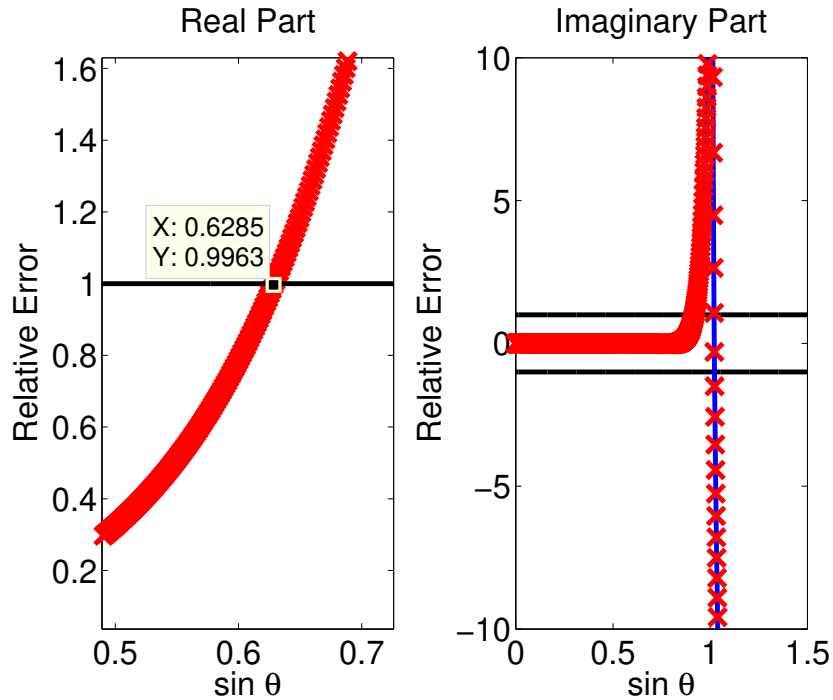


Figure 3.5: Relative error as a function of propagation angle (detail).

### 3.3 Defining the number of terms in the Padé expansion

We decided to evaluate the number of terms in the Padé expansion, that means, to check if  $N = 3$  terms is really the best option to approximate the downward-continuation operator. For this analysis, we determine for each value of  $p$  the value of  $\sigma$  that maximizes the dip angle  $\theta_m$  in dependence on the number  $N$  of terms used and on the rotation angle  $\alpha$ . Figure 3.6 plots the so-obtained maximum dip angle for  $N = 1$  for four different rotation angles. Note that each of the curves in this figure was determined with the specific function  $\sigma$  which maximizes the dip for that rotation angle. We can immediately see that the maximum dip angle decreases with increasing rotation angle, indicating that  $45^\circ$  is probably not the best choice for the rotation angle for  $N = 1$  as concluded for  $N = 3$  by Amazonas et al. (2007). The variation for small angles below  $10^\circ$  are rather small. Since a too small angle reintroduces propagating evanescent waves, we believe that  $10^\circ$  is the best possible choice for  $N = 1$ . This choice is also motivated by the analysis of migrated images shown in section 3.7.

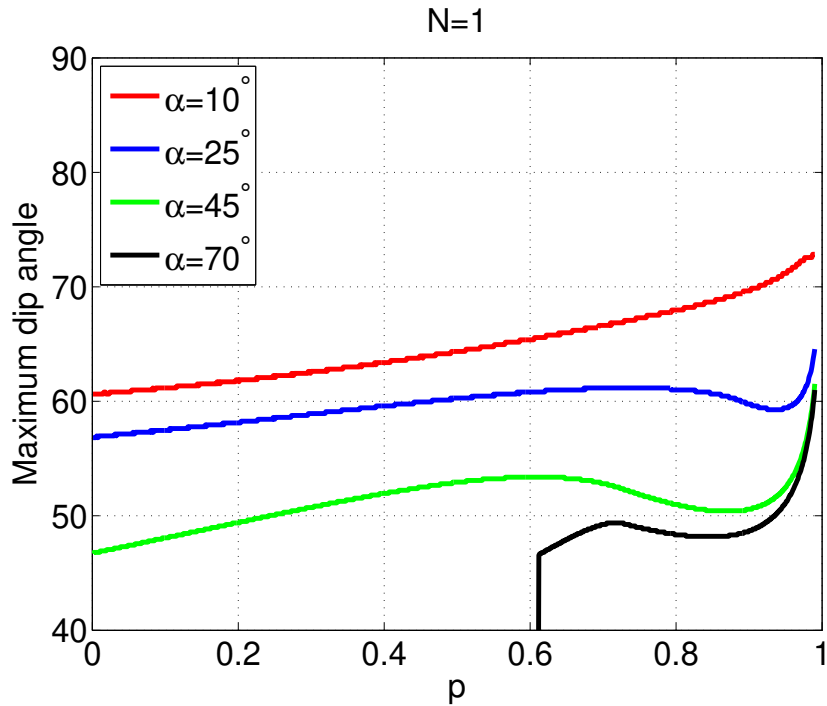


Figure 3.6: Maximum dip angle with  $N = 1$  for best possible values of  $\sigma$  and different values of  $\alpha$ .

Figure 3.7 and 3.8 show the same kind of analysis but with 2 and 3 terms in the Padé expansion, respectively. Now we can conclude that for rotation angles higher than  $45^\circ$  we get lower maximum dip angles, even with the optimal values of  $\sigma$ . Let us first analyse Figure 3.7. Our best result is with  $\alpha = 25^\circ$  but we can see a weird “valley” in the middle, where the maximum dip angle suddenly decreases. Therefore, we needed to test other angles between  $25^\circ$  and  $45^\circ$  to find the optimal value of  $\alpha$ .

In Figure 3.8 we include a comparison of the dip angles reached by the heuristic function  $\sigma = 1 + p^3$  of Amazonas et al. (2007). We see that there are still better values of  $\sigma$  than those, which allow to reach even higher dip angles. The choice of the rotation angles is less critical for  $N = 3$ . All values between  $10^\circ$  and  $45^\circ$  lead to approximately the same dip-angle behavior, except for  $p$  values between 0.8 and 1.

We already recognise from these figures that except for a small range of not very realistic values of  $p$  below 0.18, the CPFFD approximation reaches a higher dip angle with one or two terms than with three. That is actually good news because less terms in the Padé expansion mean lower computational cost.

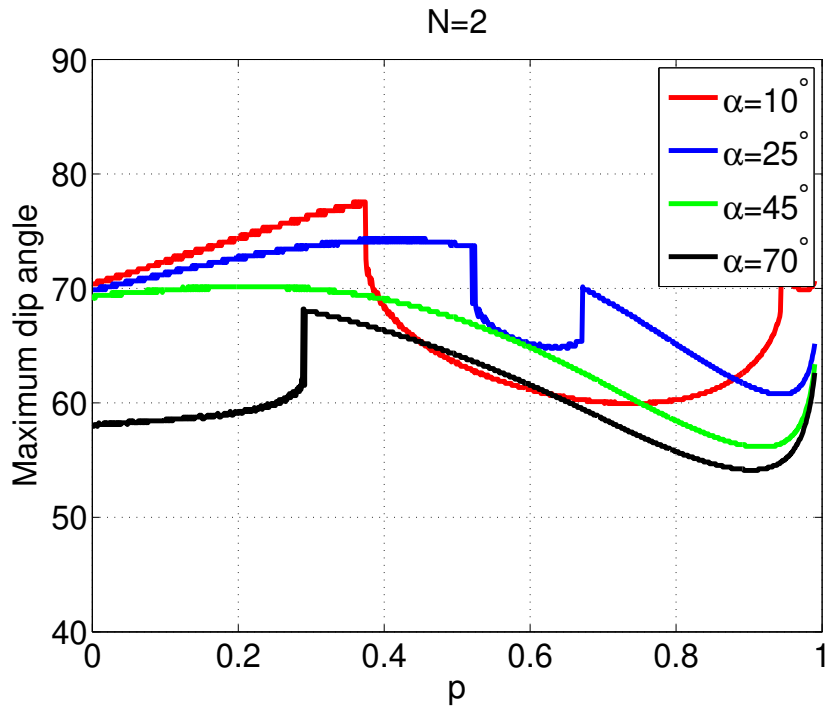


Figure 3.7: Maximum dip angle with  $N = 2$  for best possible values of  $\sigma$  and different values of  $\alpha$ .

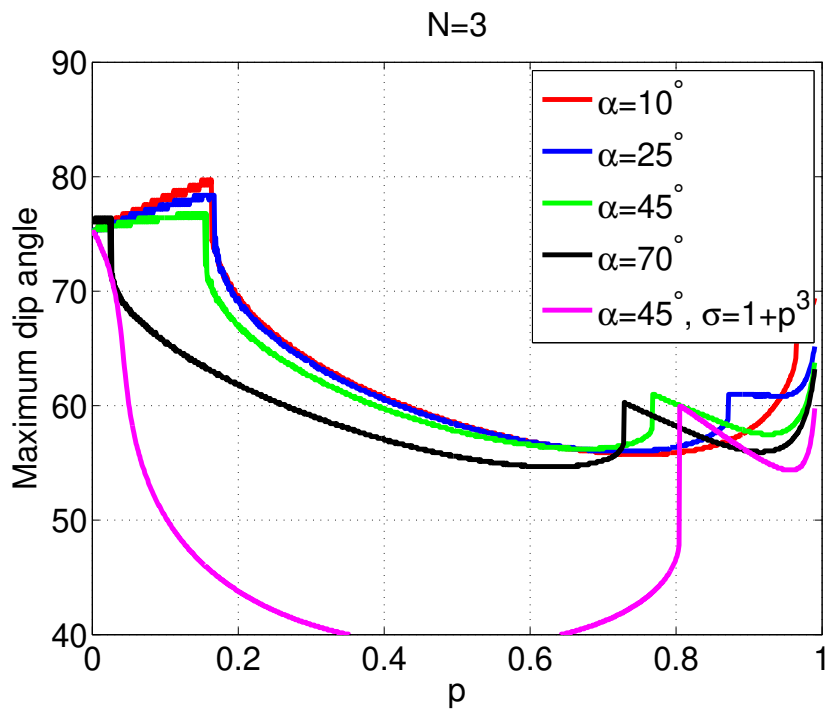


Figure 3.8: Maximum dip angle with  $N = 3$  for best possible values of  $\sigma$  and different values of  $\alpha$ .

### 3.4 Defining the optimal value of $\alpha$

In the last section we defined the optimal number of terms that should be used in the Padé expansion. Now we must find the optimal value of  $\alpha$  for one and two terms respectively. Again we plotted the maximum dip angles obtained using the optimized  $\sigma$  versus the different values of  $p$  but now we just focus on one and two terms.

In Figure 3.9 we fix  $\alpha = 10^\circ$  and unfortunately, it shows a poor outcome using 2, in contrast to 1 term which, at least in the range of  $p$  between 0.45 and 1.0 reaches dip angles of more than  $65^\circ$ . We must evaluate other angles to find the optimal  $\alpha$ , but by now using only one term allows to reach higher dip angles for the most important values of  $p$ .

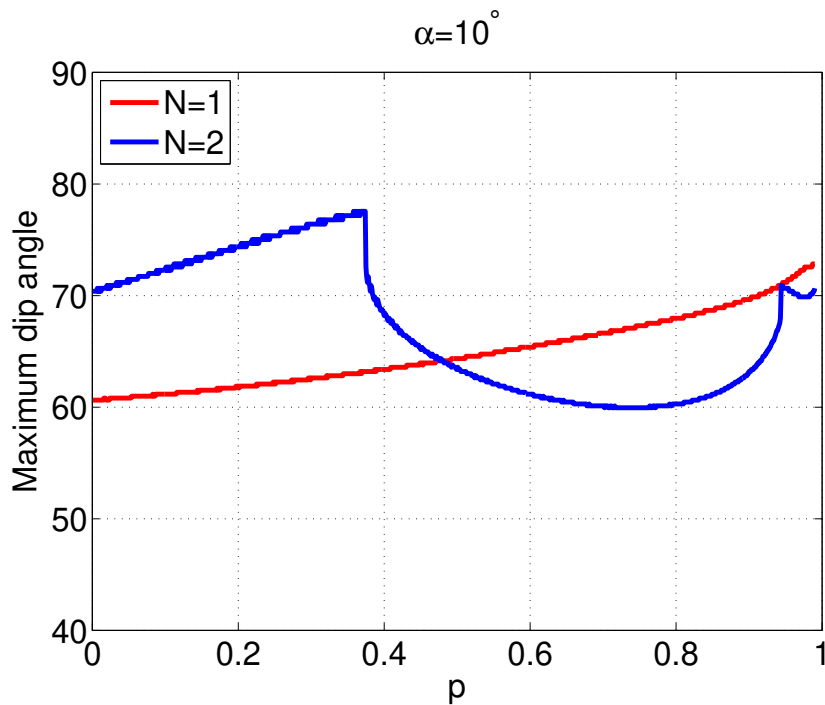


Figure 3.9: Maximum dip angle with  $\alpha = 10^\circ$  for best possible values of  $\sigma$  and different values of  $N$ .

Figure 3.10 shows the corresponding maximum dip angle for  $\alpha = 25^\circ$ . We note a downward trend using one term and increasing  $\alpha$  to  $25^\circ$ , thus concluding that we must remain with  $\alpha = 10^\circ$  when we want to use only one term in the Padé expansion. On the other hand, as the rotation angle increases we notice an improvement using two terms. The only problem is the presence of that “valley” which becomes smaller when we increase  $\alpha$ .

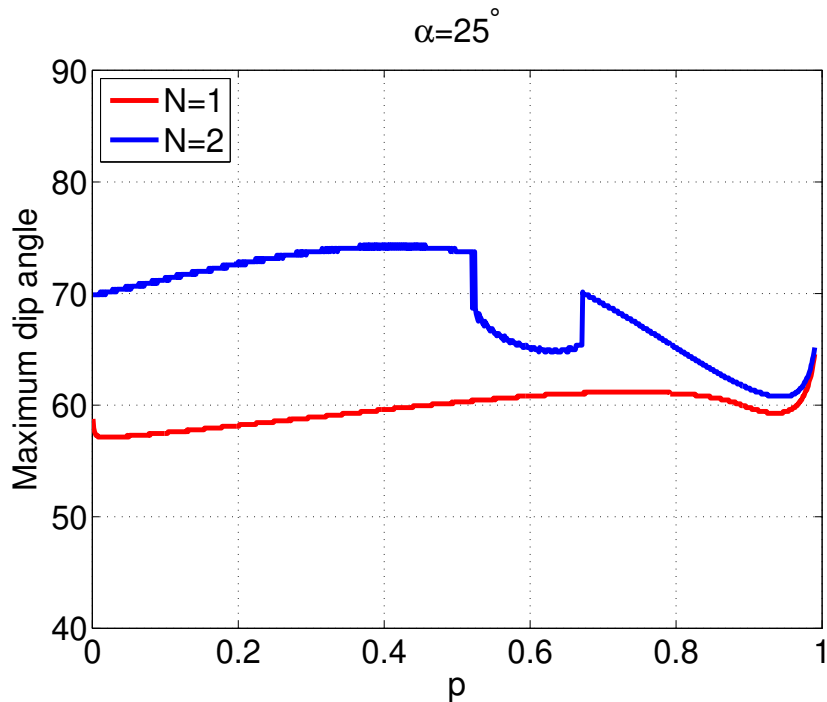


Figure 3.10: Maximum dip angle with  $\alpha = 25^\circ$  for best possible values of  $\sigma$  and different values of  $N$ .

Looking for the optimal value for two terms in the Padé expansion, we use Figure 3.10 and 3.11 to notice that the “valley” vanishes between  $25^\circ$  and  $30^\circ$ , respectively, while between  $30^\circ$  and  $35^\circ$  (see Figure 3.12) we notice a downward tendency in the curve. Therefore, we must focus on the angles between  $25^\circ$  and  $30^\circ$  to study the tendency of the curve and define the optimal value of  $\alpha$ .

Figure 3.13 helps us to define the optimal value of  $\alpha$ . As expected, the downward tendency continues and the “valley” vanishes at  $\alpha = 27^\circ$ . Thus, this is the best choice for the rotation angle when using two terms in the complex Padé approximation.

We recognise that while two terms attain higher dip angles for  $p$  values below 0.45, the one-term approximation is actually better for higher values of  $p$ . However, for a final conclusion, we have to analyse migrated images because they show the level of quality that is actually achieved with a certain approximation. Despite the fact that the approximation of the dispersion relation using one term attains higher dip angles for realistic values of  $p$ , the use of two terms in the complex Padé expansion might result in a reasonable approximation of the downward-continuation operator but so far one term seems to give better results. We will show such results in section 3.7.

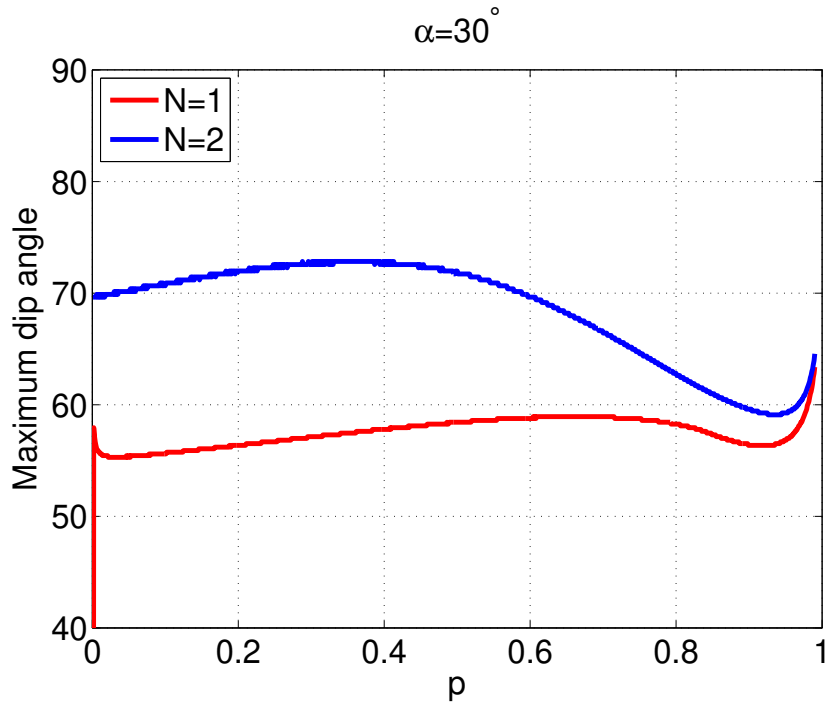


Figure 3.11: Maximum dip angle with  $\alpha = 30^\circ$  for best possible values of  $\sigma$  and different values of  $N$ .

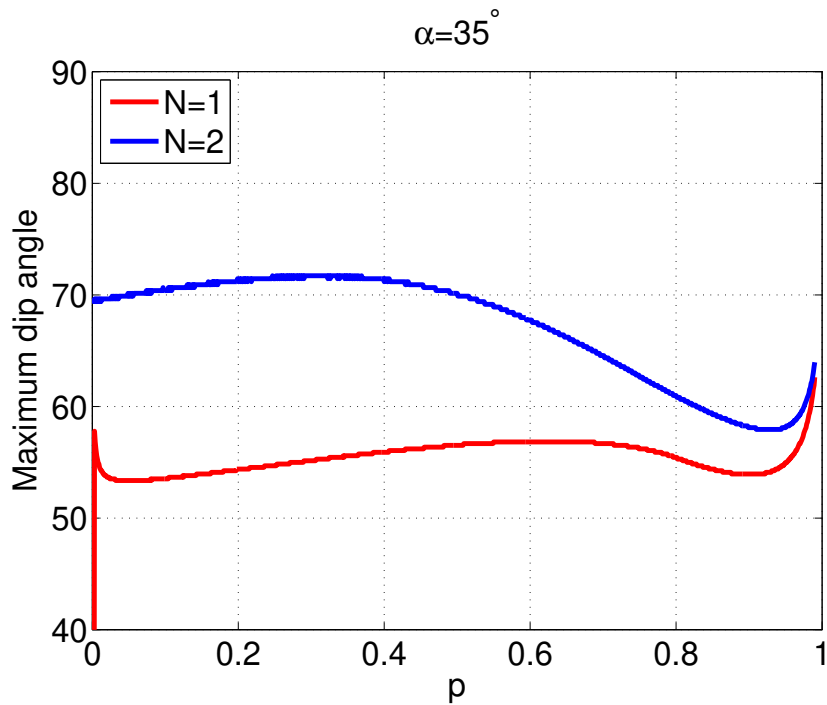


Figure 3.12: Maximum dip angle with  $\alpha = 35^\circ$  for best possible values of  $\sigma$  and different values of  $N$ .

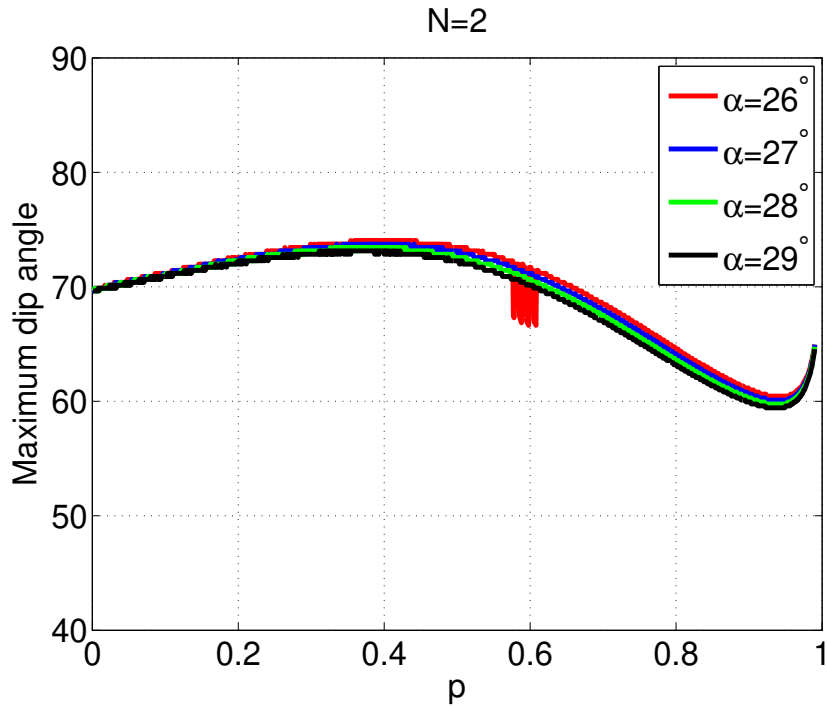


Figure 3.13: Defining the optimal value of  $\alpha$  to be used with 2 terms.

### 3.5 Comparison to earlier results

The next analysis is to compare our results with the maximum dip angles attained by the approximations of Ristow and Rühl (1994) and Amazonas et al. (2007), each one with the same condition, i.e., the dip angle obtained by the intersection of the relative error function with the one-percent error line.

Figure 3.14 shows the angles obtained with our optimized  $\sigma$  for a branch rotation angle of  $10^\circ$  and only one term in the Padé expansion. Using the same parameters, we can see that angles obtained using  $\sigma = 1 + p + p^2$  gives better results compared with the  $\sigma = 1 + p^3$  used by Amazonas et al. (2007), but none achieves the quality of the optimized  $\sigma$ .

On the other hand, Figure 3.15 presents our second result, that is, using  $27^\circ$  and two terms. In this case  $\sigma = 1 + p^3$  achieves better dip angles than  $\sigma = 1 + p + p^2$ .

Comparing the two figures, we also recognise that even for the best rotation angle of  $27^\circ$ , the 2-term approximation achieves higher dip angles only for  $p$  up to 0.7. For higher  $p$  values, the best 1-term approximation is still superior.

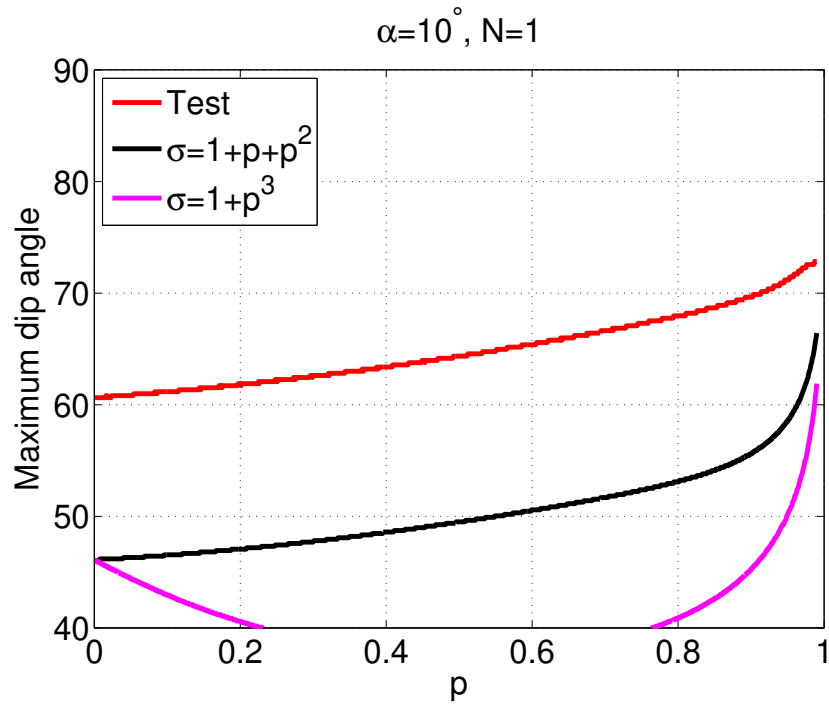


Figure 3.14: Optimized  $\sigma$  compared with the theoretical and heuristical  $\sigma$  functions using  $\alpha = 10^\circ$  and  $N = 1$ .

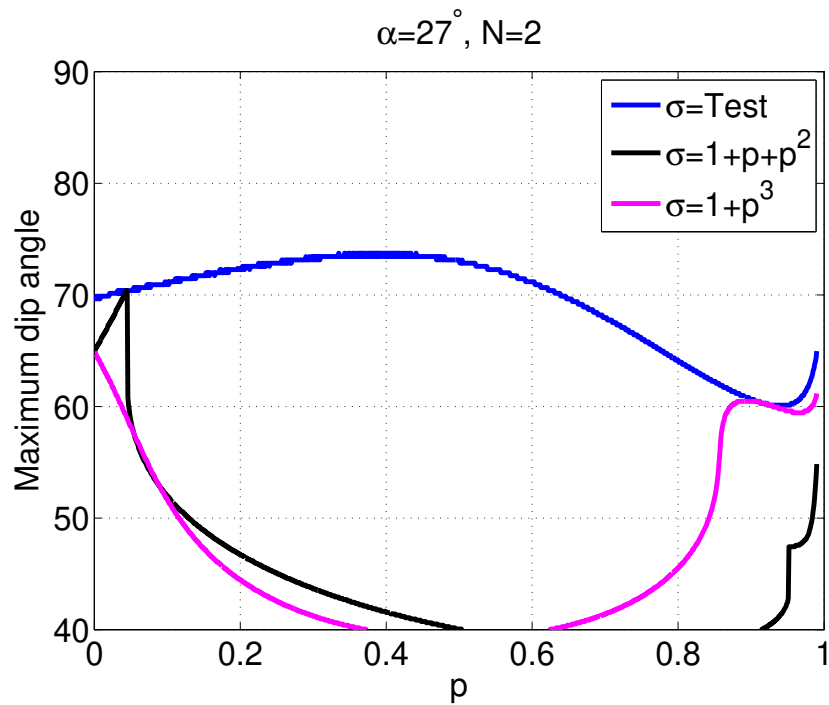


Figure 3.15: Optimized  $\sigma$  compared with the theoretical and heuristical  $\sigma$  functions using  $\alpha = 27^\circ$  and  $N = 2$ .

To finish our analysis, we present in Figure 3.16 the three results for the optimal  $\sigma$  functions for the one, two and three-term CPFFD approximation them to the one for real FFD. As explained above, the choice of the rotation angles is less critical for  $N = 3$  and we decided to chose  $\alpha = 25^\circ$  only to justify that it is not necessary to use three terms in the Padé expansion. Interestingly, the maximum dip angles obtained by the optimized  $\sigma$  curve of Ristow and Rühl (1994) for real-FFD are practically identical to those obtained for the  $N = 1, \alpha = 10^\circ$  case. This indicates that the branch-cut rotation reduces the ability of FFD migration to image steep dips, but small rotation angles can still preserve the angles achieved in the real case. The problem is that Real FFD cannot properly handle evanescent modes. Note that even small rotation angles introduce damping of the evanescent modes and should be preferred over a completely real procedure.

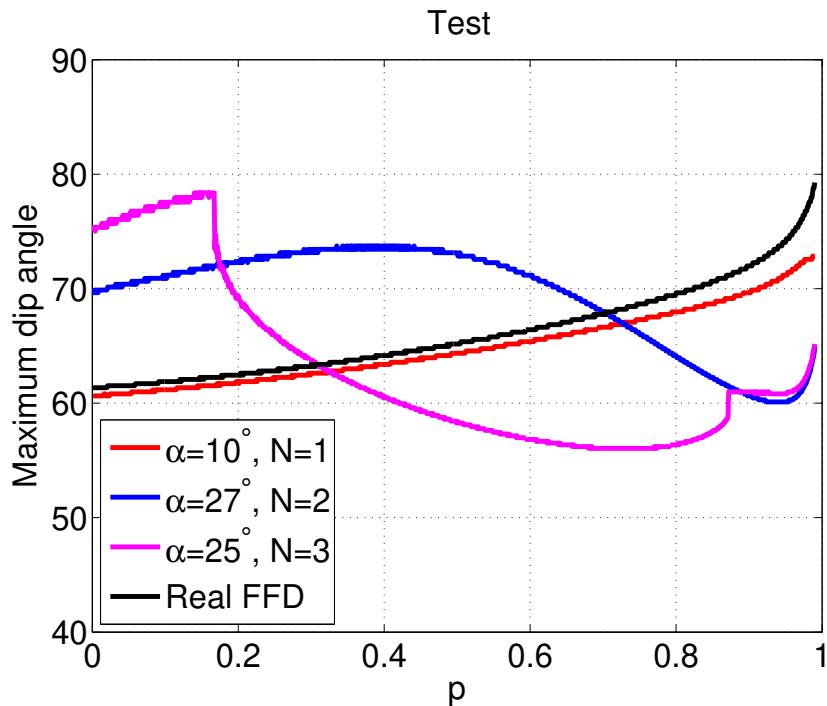


Figure 3.16: Maximum dip angles obtained with CPFFD using the optimized  $\sigma$  compared with real FFD of Ristow and Rühl (1994).

Figure 3.16 also points out our second option to handle rather strong lateral velocity variations, that is, using  $\alpha = 27^\circ$  and  $N = 2$ . These parameters values allow to reach maximum dip angles of more than  $70^\circ$  for  $p$  values below 0.7. This curve would be a good option with a velocity model in the presence of strong lateral velocity variation. The only problem of this parameters' choice is the dip angle loss for  $p$  values closer to 1.0. In any case, even that loss could represent acceptable migrated images taking into account the use of one more term. At the same time this choice will represent an increase in computational cost.

The two options present angles higher than  $60^\circ$  that in practice, would represent an improvement for imaging dipping reflectors.

Until now, we have found the appropriate values of  $\alpha$  for one and two terms, respectively. Recall that for all the tests we used the optimized value of  $\sigma$  for each value of  $p$ . Also, such optimization led to a increased maximum-dip angle. In the next section we start to evaluate this parameter  $\sigma$ .

### 3.6 Studying the optimized $\sigma$ values

In this section we analyse the optimal  $\sigma$  parameter using one, two and three terms in the complex-Padé expansion, based on the maximum dip angle attained with the analysis of one-percent error, the dispersion relation depending of the  $p$  parameter, the relative error and the behavior of the  $\sigma$  function. In all the cases we exhibit first a table with the optimal  $\sigma$  values for each value of  $p$  and also the maximum dip angle attained ( $\theta_m$ ).

Second, we present a color-coded image of the maximum dip angle as a function of  $p$  and  $\sigma$ .

Third, we show the dispersion relation following the same pattern of Ristow and Rühl (1994), i.e., we separate three different cases based on the lateral velocity variation. For a strong velocity variation we fixed the value of  $p = 0.25$ , for intermediate  $p = 0.5$  and for small velocity variation  $p = 0.9$ . And for each test, we use the corresponding optimal value of  $\sigma$ .

Fourth, we analyse the relative error at an intermediate lateral velocity variation ( $p = 0.5$ ) and we show the maximum dip angle attained for that particular case, i.e., its intersection with the one-percent line.

Fifth, we adjust a function to the numerical values of  $\sigma$  so as to determine them without the need of a table of values.

#### 3.6.1 Optimal value of $\sigma$ for $N = 1$

Figure 3.17 depicts a color-coded image of the maximum dip angle as a function of  $p$  and  $\sigma$  for a single term in the complex-Padé approximation with a branch-cut rotation angle of  $\alpha = 10^\circ$ , which we recognized as our best choice in the previous set of examples. The color bar on the right represent the maximum dip angle achieved for each pair of values  $p$  and  $\sigma$ . The curve of optimal values is clearly visible only for a small range of  $\sigma$  values for each  $p$  and, furthermore, high maximum dip angles over  $60^\circ$  (red parts of the image) are reached. We recognize from this figure that for smaller values of  $p$ , a good choice of  $\sigma$  is rather important, while at values larger than 0.8, the region of high angles broadens, indicating that a perfect choice of the optimized  $\sigma$  is less crucial here. We notice that the range of optimum  $\sigma$  values is between 1.3 and 3.7. Table 3.1 summarises the best values of  $\sigma$

for a set of  $p$  values between 0.001 and 0.99.

$p$	$\sigma$	$\theta_m$
0.001	1.298	60.63
0.05	1.354	60.81
0.10	1.415	61.16
0.15	1.481	61.52
0.20	1.551	61.88
0.25	1.626	62.25
0.30	1.705	62.62
0.35	1.789	63.00
0.40	1.878	63.38
0.45	1.973	63.96
0.50	2.073	64.36
0.55	2.178	64.76
0.60	2.291	65.37
0.65	2.411	65.99
0.70	2.539	66.64
0.75	2.677	67.29
0.80	2.829	67.97
0.85	2.999	68.67
0.90	3.198	69.64
0.95	3.467	71.17
0.99	3.723	72.84

Table 3.1: Maximum dip angle using the optimal value of  $\sigma$ ,  $N = 1$  and  $\alpha = 10^\circ$

Now we continue with the second analysis, that is, the dispersion relation using the optimized  $\sigma$ , compared with the exact operator,  $\sigma = 1 + p^3$  (Amazonas et al., 2007) and  $\sigma = 1 + p + p^2$  (Ristow and Rühl, 1994).

Figures 3.18, 3.19 and 3.20 show the real part as well as the imaginary part and we see that in any case the approximation using our optimized sigma matches the exact operator better than the other functions.

Another property is that our best approximation is obtained in Figure 3.20 which coincides with our tests done before.

Something interesting is that for a single term in the expansion,  $\sigma = 1 + p + p^2$  is even better than  $\sigma = 1 + p^3$ , which was proposed as the best  $\sigma$  value known for  $N = 3$  (Amazonas et al., 2007). In other words, the chosen values of  $\alpha$  and  $N$  influence the convenient  $\sigma$  function to be used.

Furthermore, Figure 3.21 shows the behavior of the relative error using an intermediate lateral velocity variation ( $p = 0.5$ ). In this case, the maximum dip angle achieved was  $64.36^\circ$ .

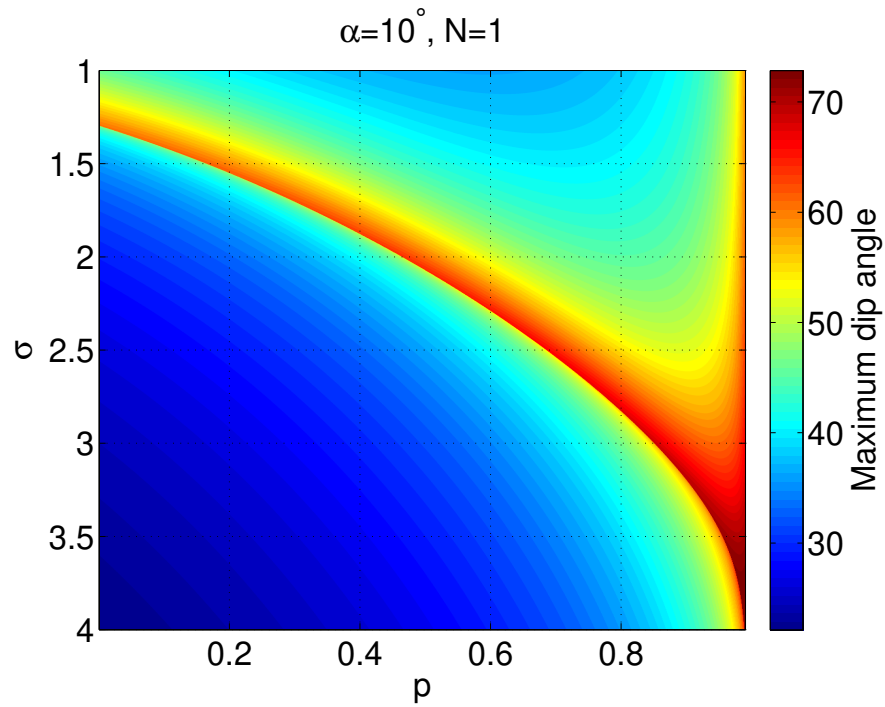


Figure 3.17: Maximum dip-angle values as a function of  $p$  and  $\sigma$  for the complex Padé approximation using  $\alpha = 10^\circ$  and  $N = 1$ .

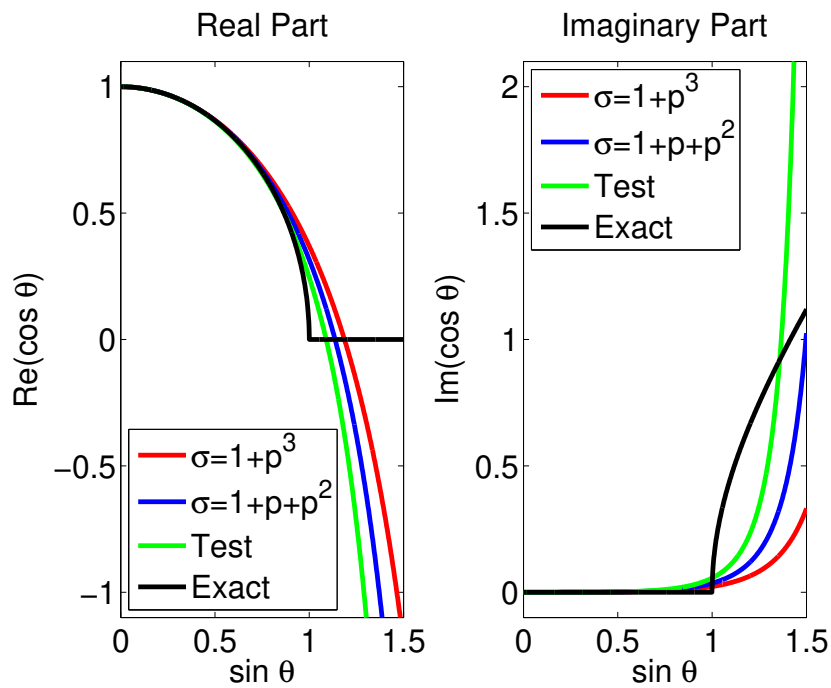


Figure 3.18: Dispersion relation with strong lateral velocity variation,  $p = 0.25$ ,  $\alpha = 10^\circ$  and  $N = 1$ .

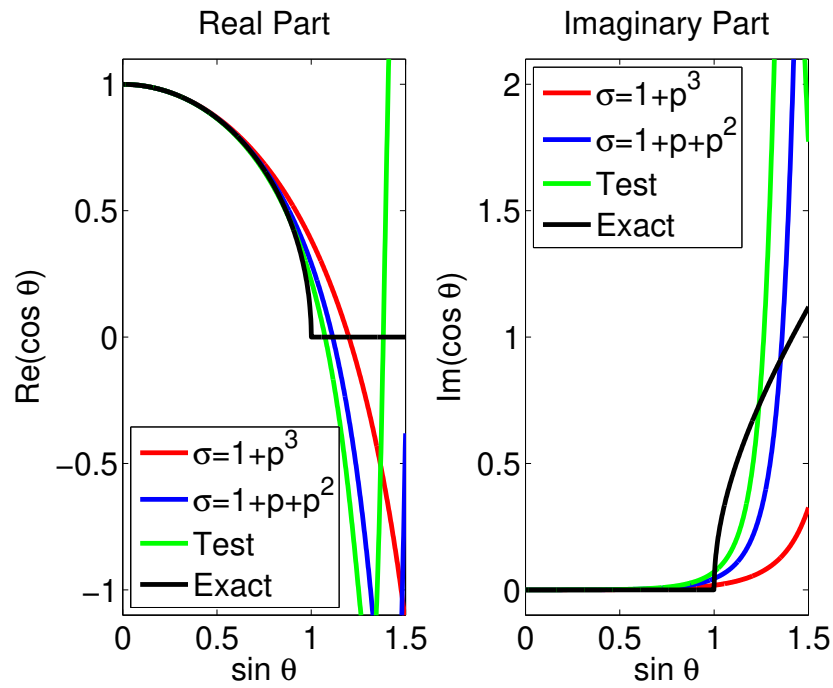


Figure 3.19: Dispersion relation with intermediate lateral velocity variation,  $p = 0.5$ ,  $\alpha = 10^\circ$  and  $N = 1$ .

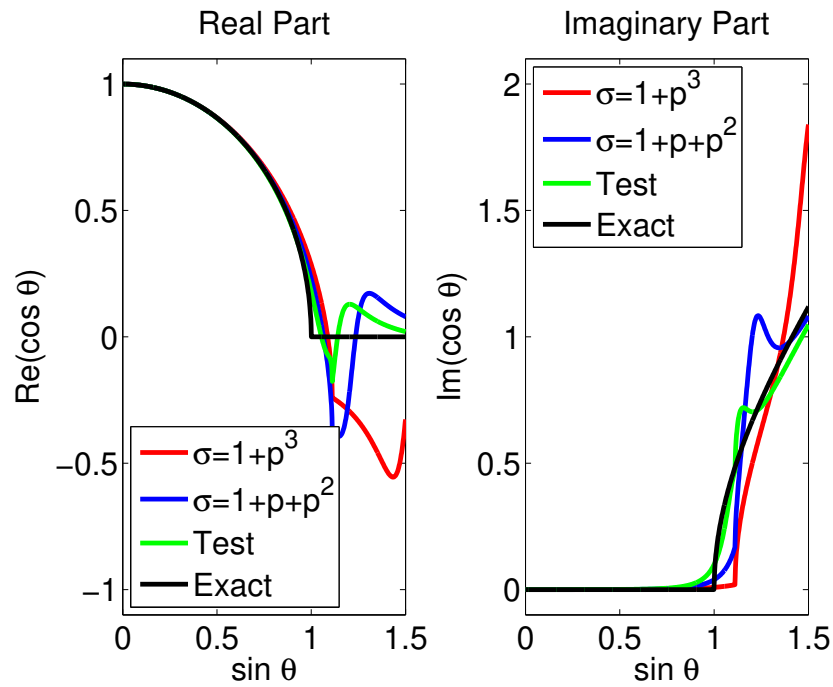


Figure 3.20: Dispersion relation with small lateral velocity variation,  $p = 0.9$ ,  $\alpha = 10^\circ$  and  $N = 1$ .

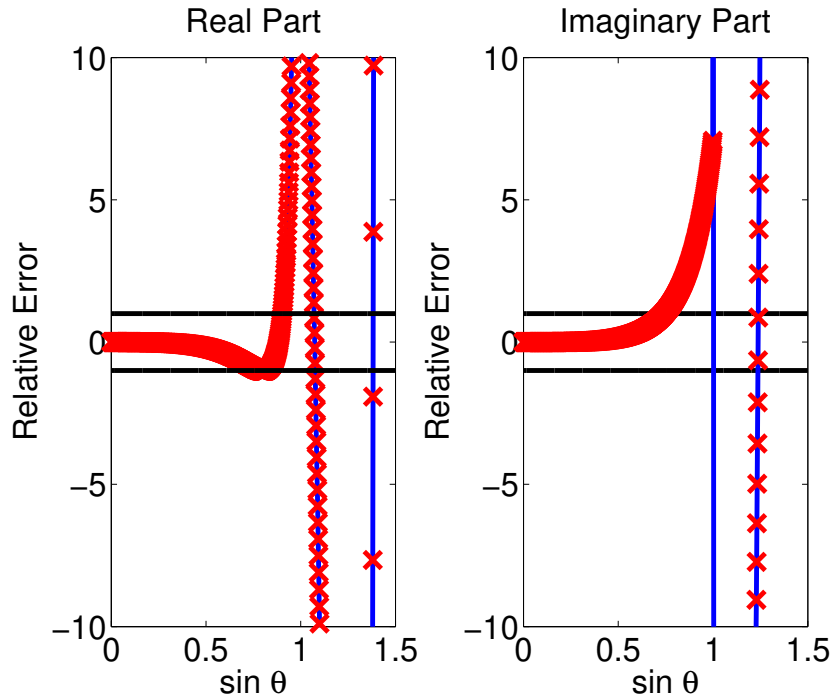


Figure 3.21: Relative error of optimized  $\sigma$ , using intermediate lateral velocity variation,  $p = 0.5$ .

### 3.6.2 Simple function $\sigma(p)$ for $N = 1$

Our next goal is to study the  $\sigma$  function, its behavior and decide a good option to approximate or adjust the numerical values.

Figure 3.22 shows the optimal  $\sigma$  values versus all the possible values of  $p$ . The function is smooth, thus being easily adjustable with a polynomial function using least-squares. We use the Curve Fitting Toolbox 3.5.3 from Matlab, there we define the  $X$  and  $Y$  data which are  $p$  and  $\sigma$ , respectively. Then, we select the option polynomial from the fit category list, and define the degree. Finally, Matlab give us the corresponding coefficients (with 95% confidence bounds) to be used in the new  $\sigma$  function. We achieved excellent fit with the 4th-order polynomial

$$\sigma = 1.319 + 0.4981p + 4.259p^2 - 6.596p^3 + 4.292p^4. \quad (3.4)$$

The only visible deviation from the numerical curve occurs in the region of  $p > 0.9$ , where perfect adjustment is not crucial as explained in section 3.6.1.

Recall that this  $\sigma$  must be used together with the two parameters that were optimized, that is,  $\alpha = 10^\circ$  and  $N = 1$ .

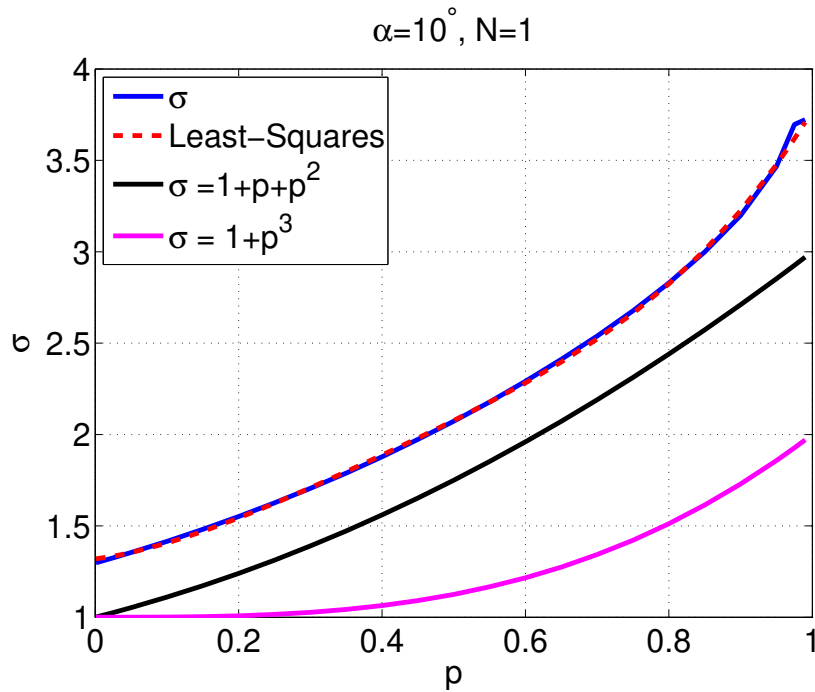


Figure 3.22: Optimized  $\sigma$  function versus least-squares.

### 3.6.3 Optimal value of $\sigma$ for $N = 2$

Now we look for the optimized  $\sigma$  using  $N = 2$  and  $\alpha = 27^\circ$ . Figure 3.23 shows the maximum dip angle as a function of  $p$  and  $\sigma$ , and Table 3.2 summarises the optimal  $\sigma$  values for  $p$  between 0.001 and 0.99 together with the achieved maximum dip angle. We see that under these conditions the best angles are attained for  $p$  below 0.5. The lowest maximum dip angles are reached for  $p > 0.7$ . Another feature is that the range of optimum  $\sigma$  values is between 1 and 1.8.

Figures 3.24 to 3.26 show the improved quality of the achieved approximation of the dispersion relation for strong, intermediate and weak velocity variations, as compared to  $\sigma = 1 + p^3$  and  $\sigma = 1 + p + p^2$ .

$p$	$\sigma$	$\theta_m$
0.001	1.023	69.88
0.05	1.049	70.39
0.10	1.077	70.91
0.15	1.106	71.71
0.20	1.135	72.27
0.25	1.164	72.84
0.30	1.195	73.44
0.35	1.226	73.44
0.40	1.259	73.74
0.45	1.293	73.44
0.50	1.330	73.14
0.55	1.370	72.27
0.60	1.414	71.17
0.65	1.464	69.64
0.70	1.520	67.97
0.75	1.586	65.99
0.80	1.659	64.16
0.85	1.710	62.25
0.90	1.760	60.63
0.95	1.790	60.11
0.99	1.640	64.96

Table 3.2: Maximum dip angle using the optimal value of  $\sigma$ ,  $N = 2$  and  $\alpha = 27^\circ$

Second, we study the dispersion relation and unlike our first result using  $N = 1$ , here our best angle is obtained with strong lateral velocity variation, as we see in Figure 3.24, while an increase in  $p$  leads to reduced angles (see Figure 3.25 and 3.26). In addition, Figure 3.26 shows that  $\sigma = 1 + p^3$  has the same behavior as our optimized  $\sigma$  but not for other values of  $p$ . On the other hand, it is not clear which of the older functions ( $\sigma = 1 + p^3$  and  $\sigma = 1 + p + p^2$ ) is better but in any case, our optimized  $\sigma$  is always the best approximation to the exact operator.

Additionally, Figure 3.27 shows the relative error for the particular case of intermediate lateral velocity variation, which presents an angle of  $73^\circ$ , that means, higher than with the use of only one term as expected.

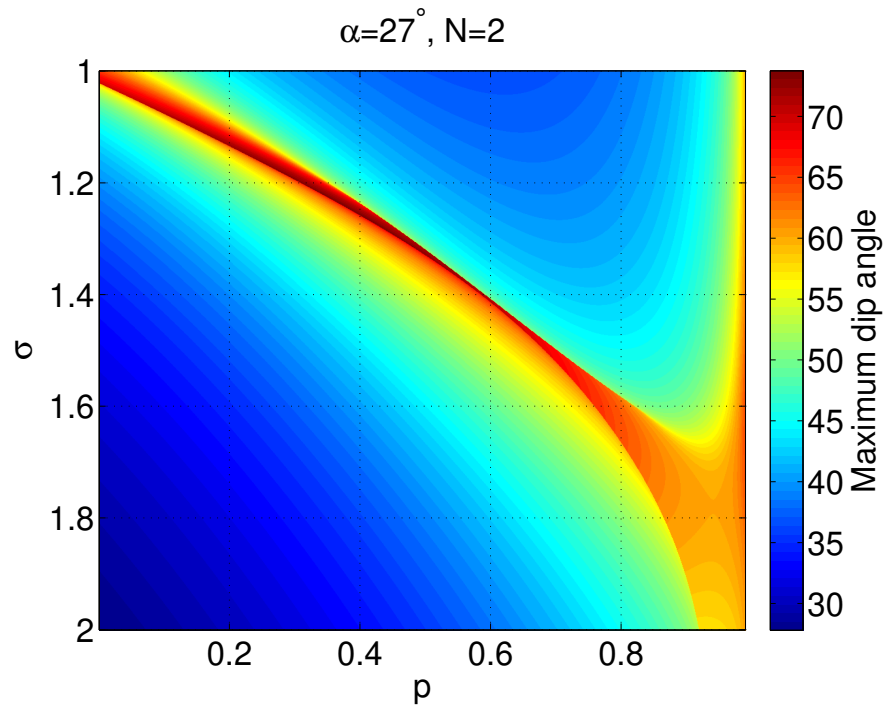


Figure 3.23: Maximum dip-angle values as a function of  $p$  and  $\sigma$  for the complex Padé approximation using  $\alpha = 27^\circ$  and  $N = 2$ .

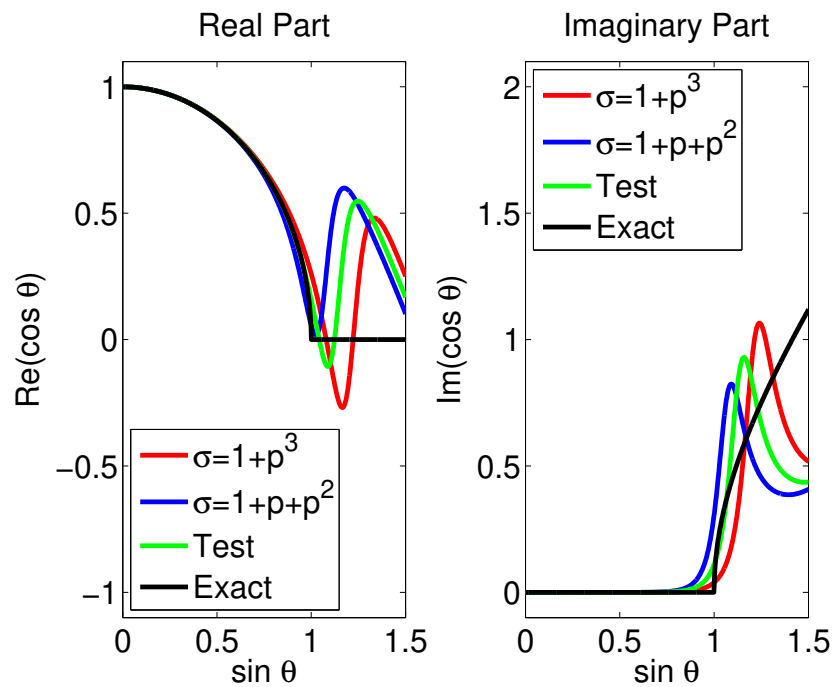


Figure 3.24: Dispersion relation with strong lateral velocity variation,  $p = 0.25$ ,  $\alpha = 27^\circ$  and  $N = 2$ .

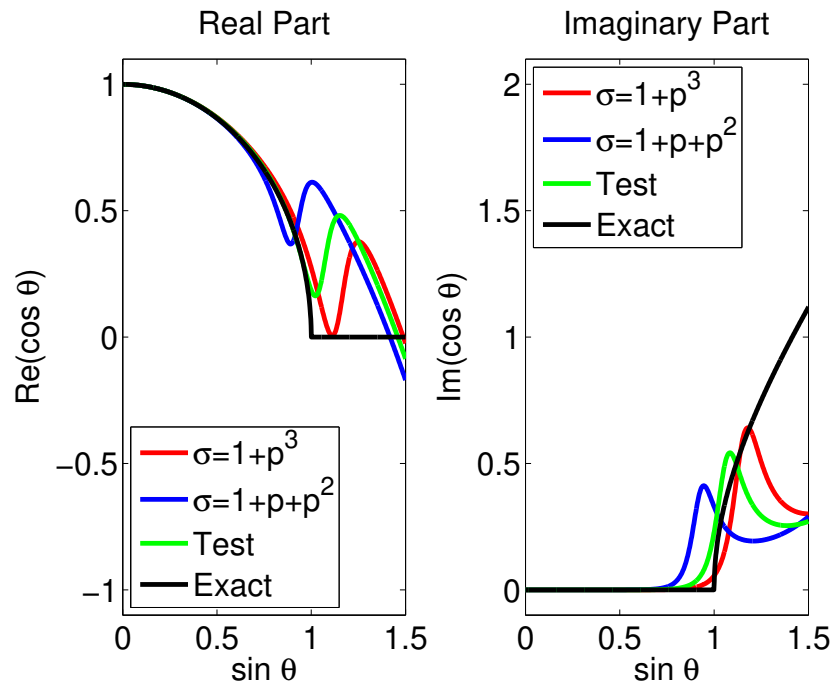


Figure 3.25: Dispersion relation with intermediate lateral velocity variation,  $p = 0.5$ ,  $\alpha = 27^\circ$  and  $N = 2$ .

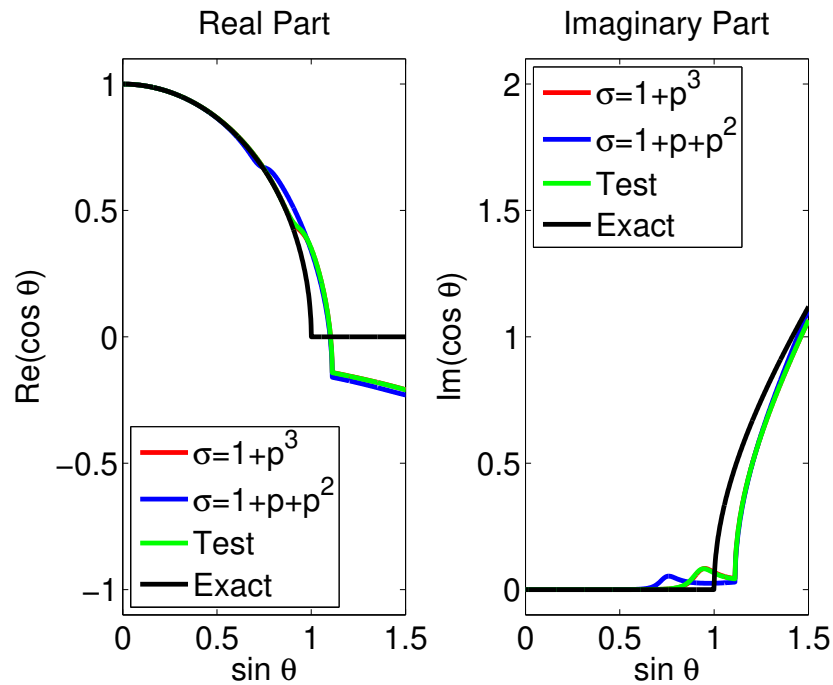


Figure 3.26: Dispersion relation with small lateral velocity variation,  $p = 0.9$ ,  $\alpha = 27^\circ$  and  $N = 2$ .

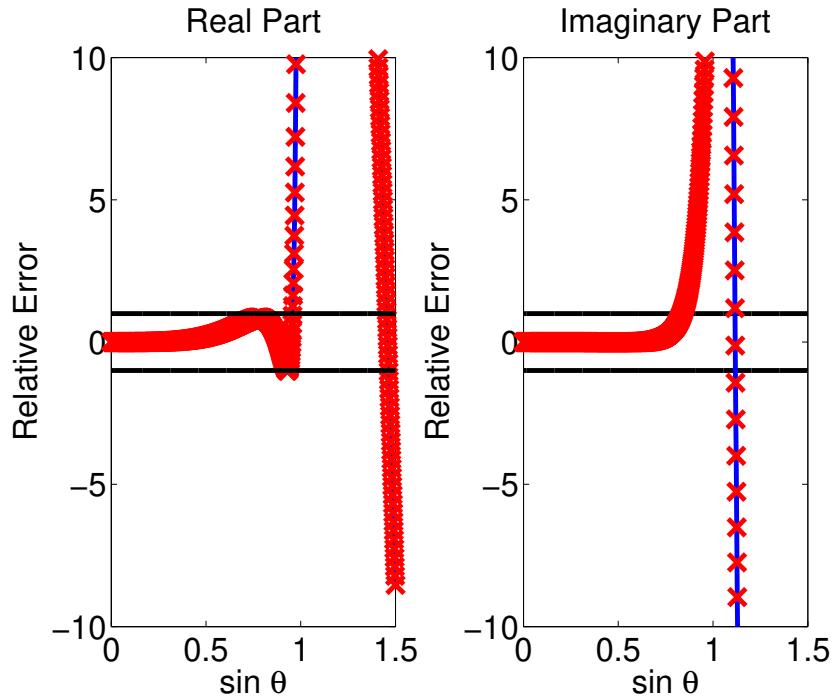


Figure 3.27: Relative error of optimized  $\sigma$ , using intermediate lateral velocity variation,  $p = 0.5$ .

### 3.6.4 Simple function $\sigma(p)$ for $N = 2$

Finally, we study the  $\sigma$  function in order to adjust the numerical values, looking for a function able to fit the values of  $\sigma$ . The procedure was the same as in section 3.6.3 but now a polynomial fit is not the best option. Based on the numerical values in Figure 3.28 we propose to use a 3rd-order polynomial and add a logarithmic term to fit the behavior of the optimized  $\sigma$  curve for values of  $p$  close to one. To obtain such a function we select in Matlab the custom equation fit instead of polynomial, then we define the suggested function and Matlab gives us the new coefficients according to the proposed  $\sigma$  function. The equation able to fit almost perfect the numerical values as shown in Figure 3.28 is

$$\sigma = 1.018 + 0.8381p - 0.5324p^2 + 1.101p^3 + 0.1636 \ln(1.0001 - p) . \quad (3.5)$$

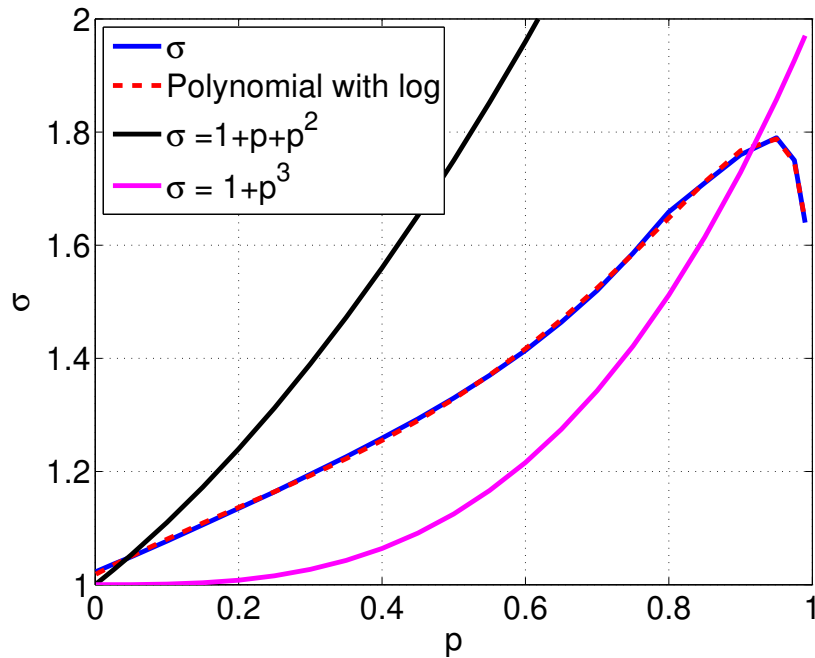


Figure 3.28: Optimized  $\sigma$  function versus our custom equation with  $N = 2$

### 3.6.5 Optimal value of $\sigma$ for $N = 3$

As we explained before, the choice of the rotation angle is less critical for  $N = 3$  and, again we decided to use  $\alpha = 25^\circ$  basically to show the scopes of the CPFFD using 3 terms. Table 3.3 shows good angles only for values of  $p$  up to 0.15 which, in practice, are not significant because the actual propagation velocity would be almost sixfold higher than the reference velocity. On the other hand, for realistic values of  $p$ , we find a poor outcome for the angles attained, much less than our results using  $N = 1$  and  $N = 2$ .

In order to complement the analysis for  $N = 3$ , Figure 3.29 shows the optimal value of  $\sigma$  for each value of  $p$ . It is possible to see a red region with high angles only for the first values of  $p$ . Also, this image allows us to see the  $\sigma$  function. Its shape is similar to the case of  $N = 2$ . In the next section we discuss the  $\sigma$  function based on the numerical values.

$p$	$\sigma$	$\theta_m$
0.001	1.009	75.02
0.05	1.027	76.05
0.10	1.045	77.16
0.15	1.062	77.96
0.20	1.087	69.39
0.25	1.119	65.99
0.30	1.154	63.77
0.35	1.192	61.88
0.40	1.229	60.63
0.45	1.269	59.43
0.50	1.310	58.43
0.55	1.353	57.46
0.60	1.394	56.82
0.65	1.434	56.36
0.70	1.473	56.05
0.75	1.505	56.05
0.80	1.535	56.36
0.85	1.551	57.46
0.90	1.546	60.99
0.95	1.503	60.81
0.99	1.380	65.16

Table 3.3: Maximum dip angle using the optimal value of  $\sigma$ ,  $N = 3$  and  $\alpha = 25^\circ$

Figure 3.30, 3.31 and 3.32 show the dispersion relation taking into account the lateral velocity variation. Something interesting about these tests is the fact that  $\sigma = 1 + p^3$  of Amazonas et al. (2007) is a great approximation for both the real and the imaginary part, unlike the use of  $\sigma = 1 + p + p^2$  which exhibit a poor outcome. Nevertheless, the green line representing our optimal  $\sigma$  is always the best approximation.

Finally, Figure 3.33 shows the relative error using an intermediate lateral velocity variation ( $p = 0.5$ ), which gives an angle of  $58.43^\circ$ , much less than our outcomes using  $N = 1$  or  $N = 2$ .

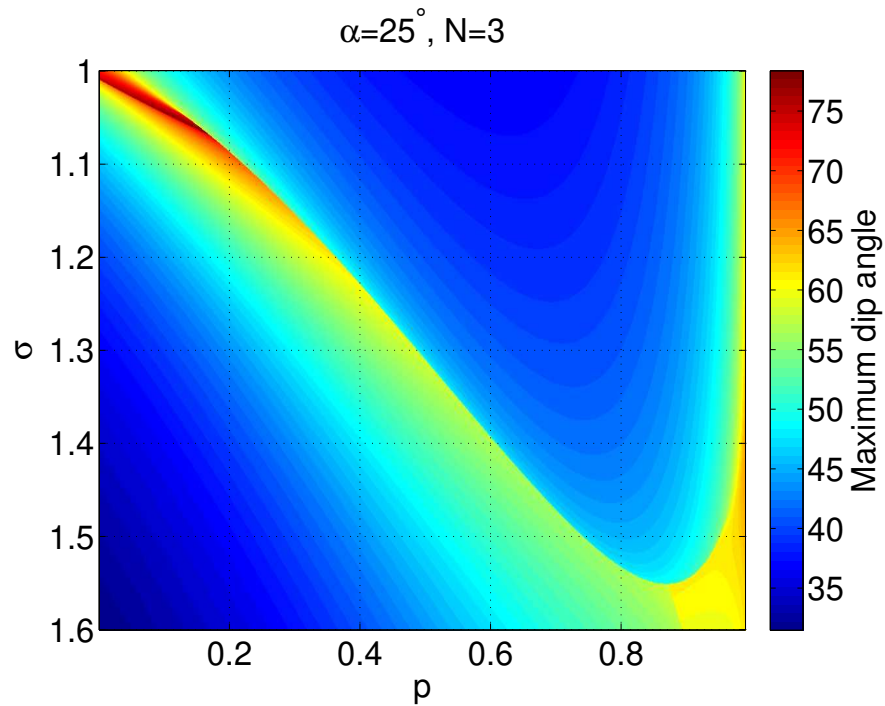


Figure 3.29: Maximum dip-angle values as a function of  $p$  and  $\sigma$  for the complex Padé approximation using  $\alpha = 25^\circ$  and  $N = 3$ .

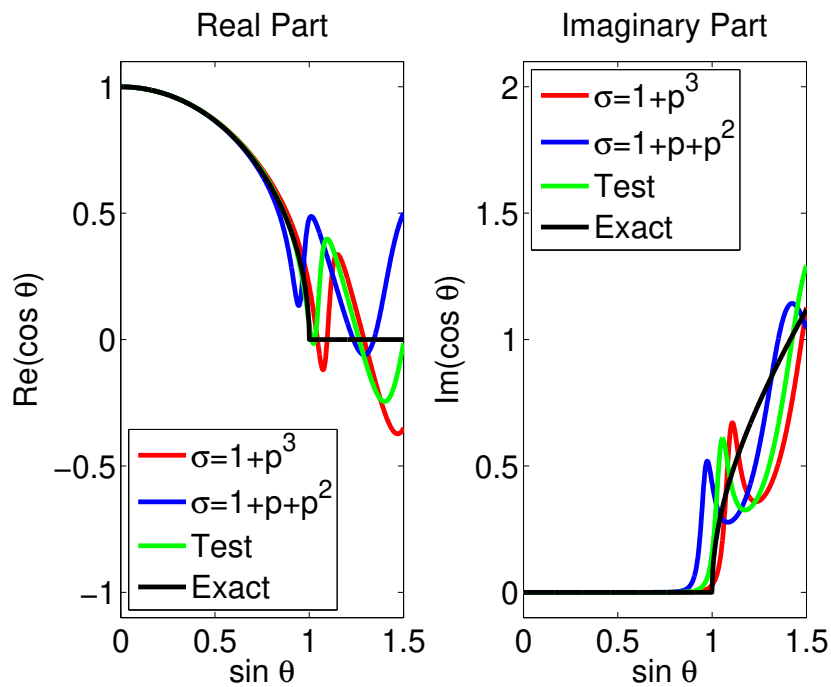


Figure 3.30: Dispersion relation with strong lateral velocity variation,  $p = 0.25$ ,  $\alpha = 25^\circ$  and  $N = 3$ .

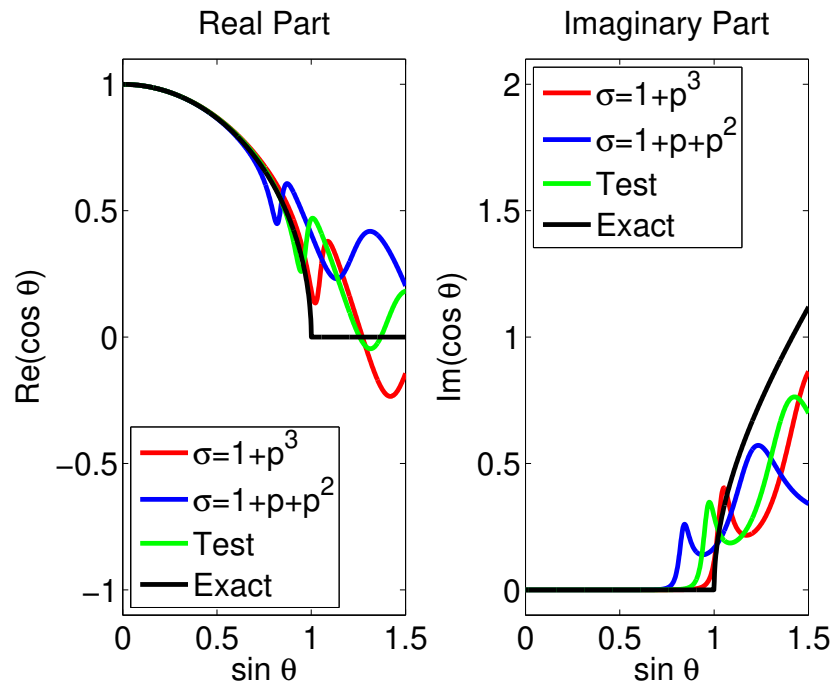


Figure 3.31: Dispersion relation with intermediate lateral velocity variation,  $p = 0.5$ ,  $\alpha = 25^\circ$  and  $N = 3$ .

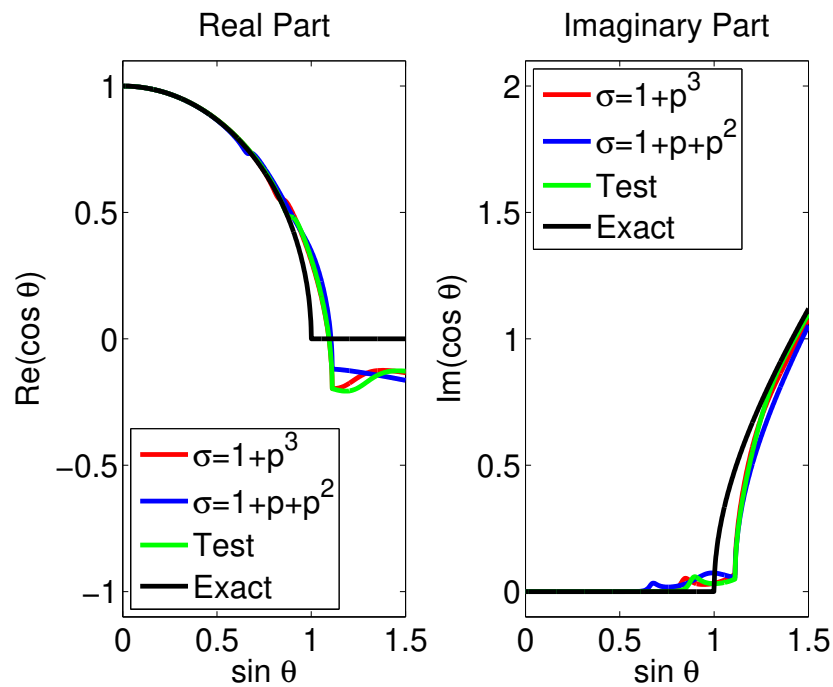


Figure 3.32: Dispersion relation with small lateral velocity variation,  $p = 0.9$ ,  $\alpha = 25^\circ$  and  $N = 3$ .

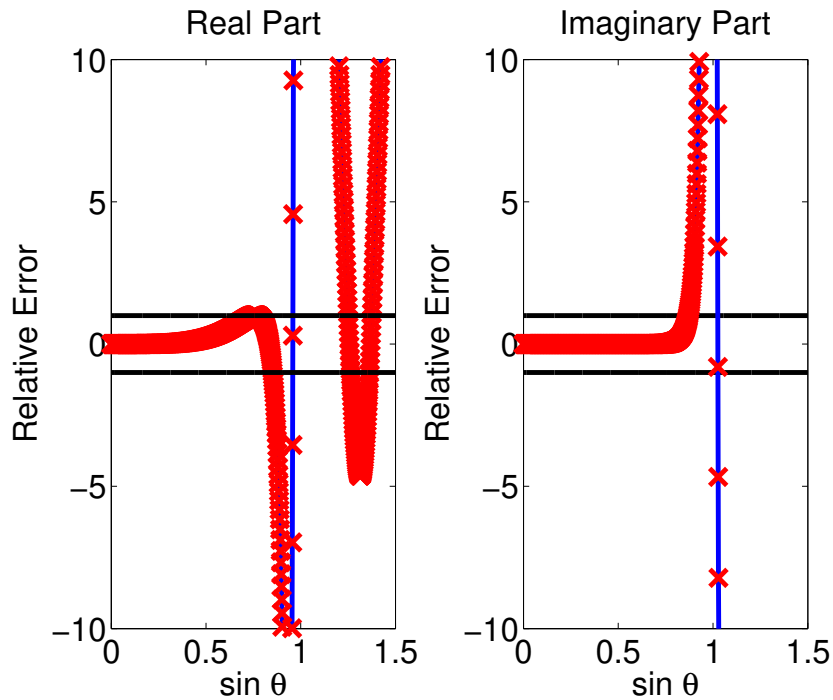


Figure 3.33: Relative error of optimized  $\sigma$ , using intermediate lateral velocity variation,  $p = 0.5$ ,  $\alpha = 25^\circ$  and  $N = 3$ .

### 3.6.6 Simple function $\sigma(p)$ for $N = 3$

Figure 3.34 shows the optimal values of  $\sigma$  and the function that almost perfectly fits the numerical values. Again, like in section 3.6.4 we needed a logarithmic term and the procedure to obtain the coefficients was the same, i.e., using the custom equation fit in the Curve Fitting Toolbox. The equation for  $\sigma$  using three terms and with its corresponding coefficients is

$$\sigma = 1.018 + 0.2054p + 1.466p^2 - 0.8386p^3 + 0.101 \ln(1.0001 - p). \quad (3.6)$$

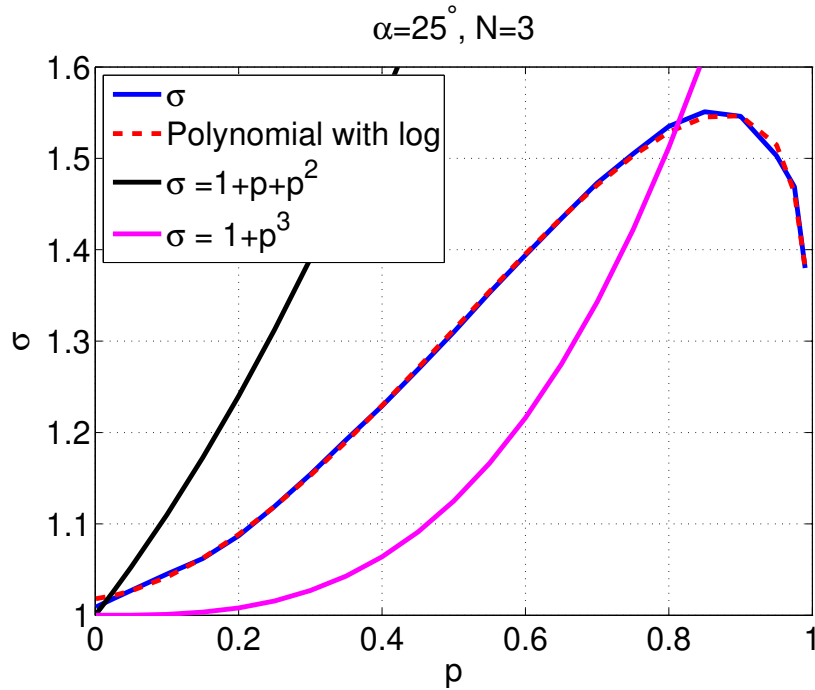


Figure 3.34: Optimized  $\sigma$  function versus our custom equation with  $N = 3$

### 3.7 Rotation angle for one-term complex Padé approximation

We have seen above that the maximum dip angle that can be reached with a one-term Padé approximation does not vary very much for rotation angles between  $0^\circ$  and  $10^\circ$ . To define which branch-cut rotation angle to recommend, we decided to look at migrated images in order to evaluate the artifacts. For this purpose, we modified the implementation of the wide-angle complex FFD approximations of Amazonas et al. (2007) to perform prestack depth migration in 2D to test different choices. The imaging condition is a crosscorrelation of the downward-continued upgoing wavefield and the downgoing wavefield from the source at zero time lag. The source wavefield is modeled using a Ricker wavelet with 25-Hz peak frequency and a depth sampling interval of 12 m. We then migrated the Marmousi data (Versteeg, 1994) using the true velocity model without any smoothing (see Figure 3.35).

Figure 3.36, 3.37 and 3.38 show the images for  $5^\circ$ ,  $10^\circ$  and  $15^\circ$  values of  $\alpha$  respectively. Initially, our choice was  $5^\circ$ , but as we can see, the image presents artifacts similar to real FFD (particularly visible in the areas indicated by red frames), because the damping of evanescent modes is incomplete. That lead us to increase the angle of the branch cut, but always considering that an increase represents loss of maximum dip angle. Comparing Figure 3.36 with our choice, i.e.,  $10^\circ$  in Figure 3.37, we see an improvement regarding the artifacts. Finally, the use of  $15^\circ$  in Figure 3.38 doesn't show a remarkable improvement of the evanescent modes, but we start seeing the loss of the principal faults. Therefore,

we concluded that  $10^\circ$  represents the best angle for the one-term approximation. We compare the corresponding migration result with the image obtained using the heuristic function of Amazonas et al. (2007) (Figure 3.39) and our best result using two terms (Figure 3.40).

The three migrated images appear to resolve the faults equally well. The deeper parts are virtually identical. The migration in Figure 3.37 was 42% faster than the one in Figure 3.39. Furthermore, the image in Figure 3.40 was obtained with two terms at 13% reduced computational cost. Comparing our two best results, i.e., using either one or two terms, with Figure 3.39, though there are some slight differences between the images, it is hard to tell which one is better.

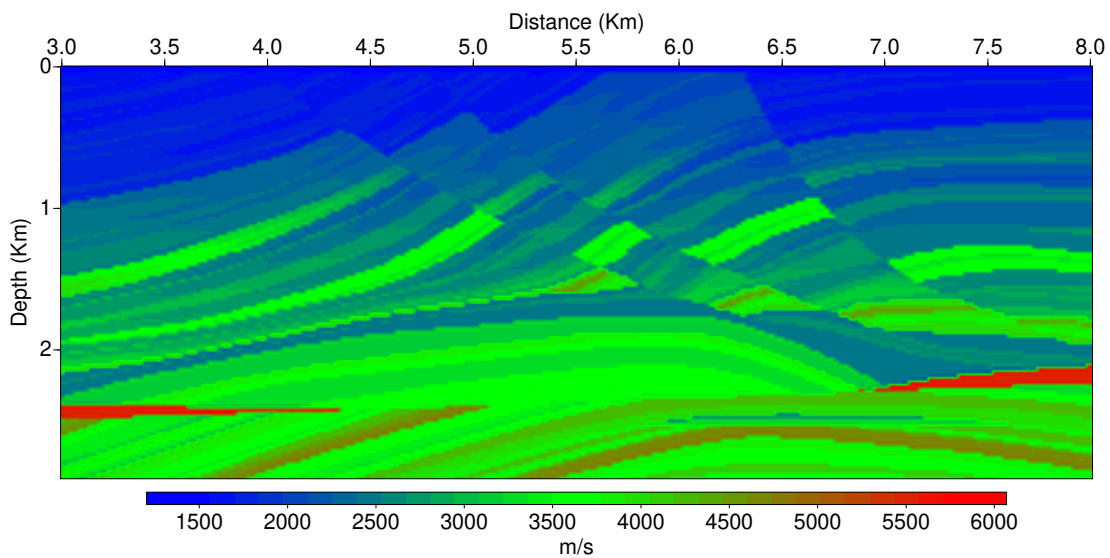


Figure 3.35: Marmousi velocity model.

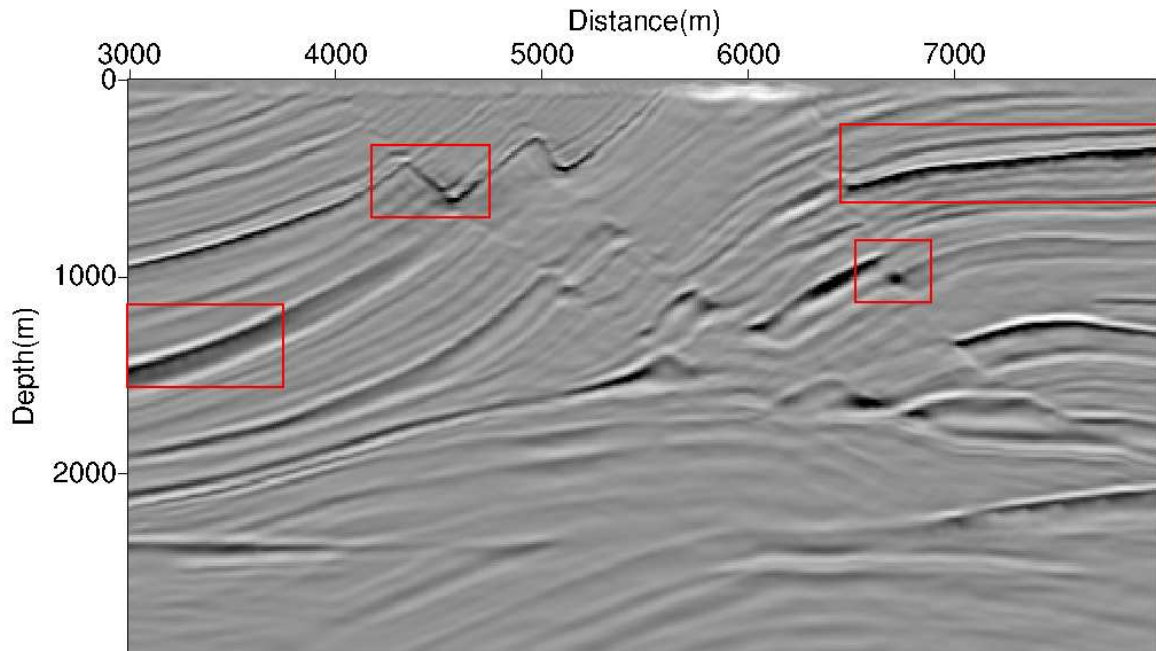


Figure 3.36: Pre-SDM of Marmousi data set using optimized  $\sigma$ ,  $N = 1$ ,  $\alpha = 5^\circ$ .

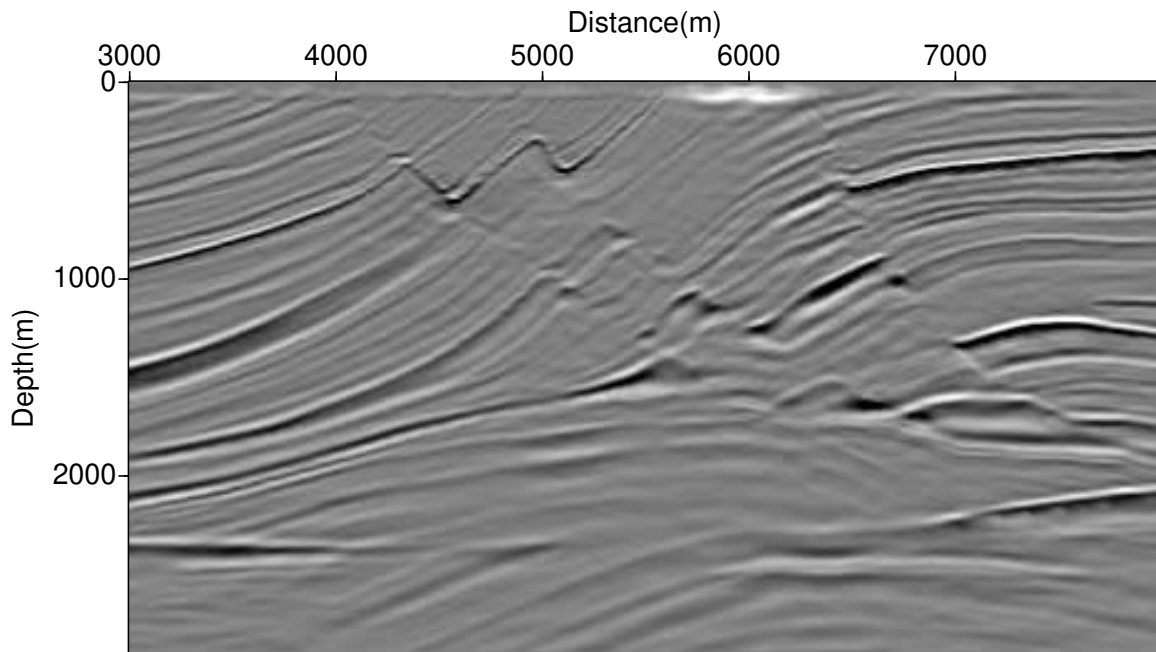


Figure 3.37: Pre-SDM of Marmousi data set using  $\sigma$  from equation 3.4,  $N = 1$ ,  $\alpha = 10^\circ$ .

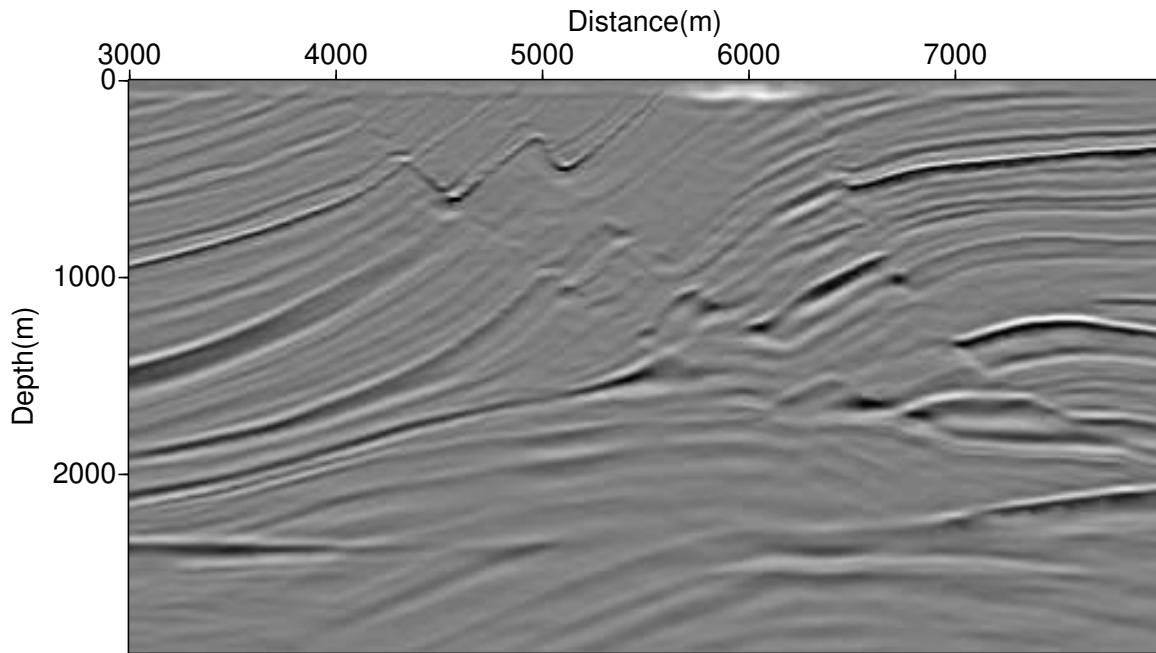


Figure 3.38: Pre-SDM of Marmousi data set using optimized  $\sigma$ ,  $N = 1$ ,  $\alpha = 15^\circ$ .

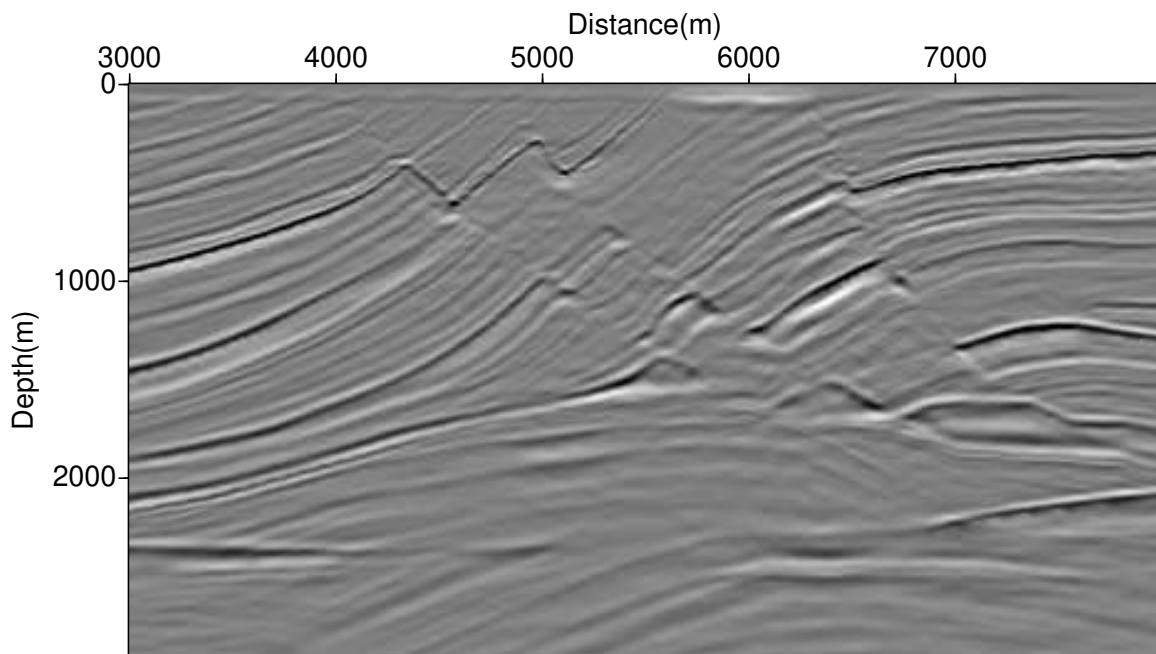


Figure 3.39: Pre-SDM of Marmousi data set using  $\sigma = 1 + p^3$ ,  $N = 3$ ,  $\alpha = 45^\circ$ .

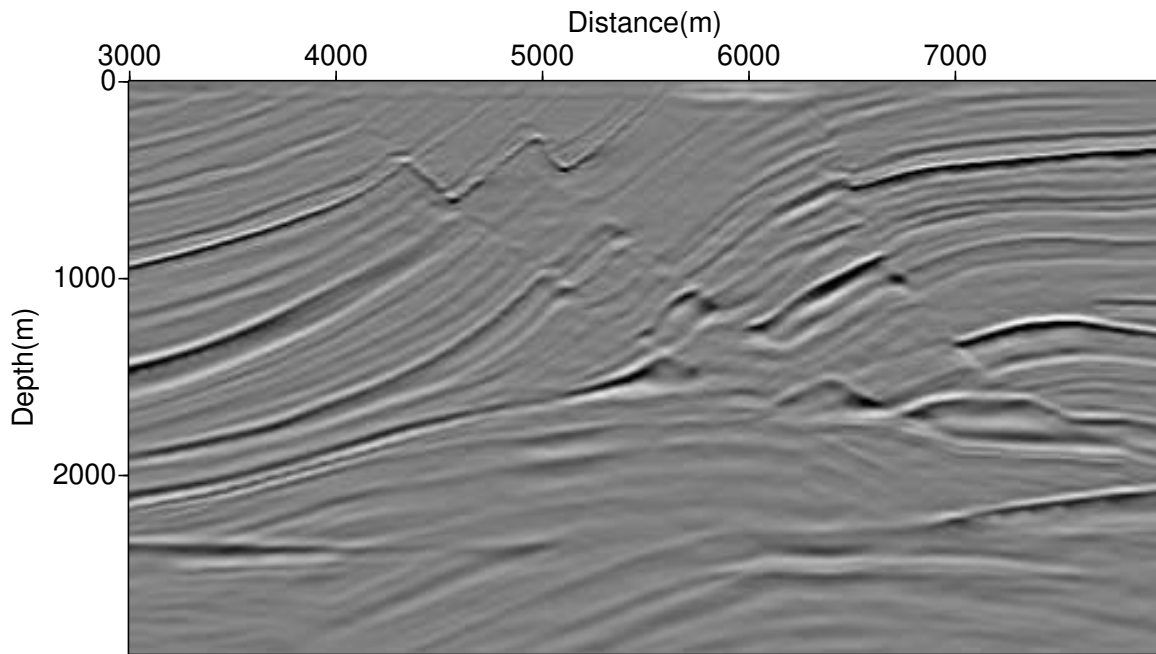


Figure 3.40: Pre-SDM of Marmousi data set using  $\sigma$  from equation 3.5,  $N = 2$ ,  $\alpha = 27^\circ$ .

To make sure that our conclusions did not apply only to a single data set, we also applied the CPFFD algorithms to synthetic data from the SEG/EAGE salt model (Aminzadeh et al., 1995) (see Figure 3.41). For this model the sampling interval is 24.384 m (80 ft). The three migrated images allow identifying all the major faults position. At the top of salt, like the tall crest and the sharp valleys, we see slight differences, but, even so, the three migrations are completely acceptable. Furthermore, beneath the salt the three images are nearly indistinguishable while the savings in computation time are the same in both models (about 42% for  $N = 1$  and 13% for  $N = 2$ ).

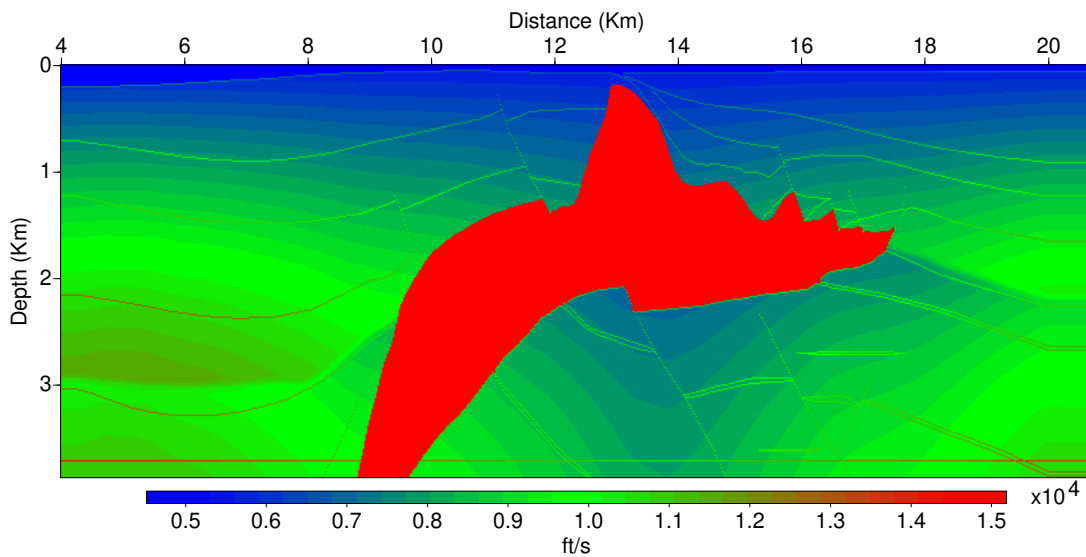


Figure 3.41: A 2D slice of the SEG/EAGE salt model.

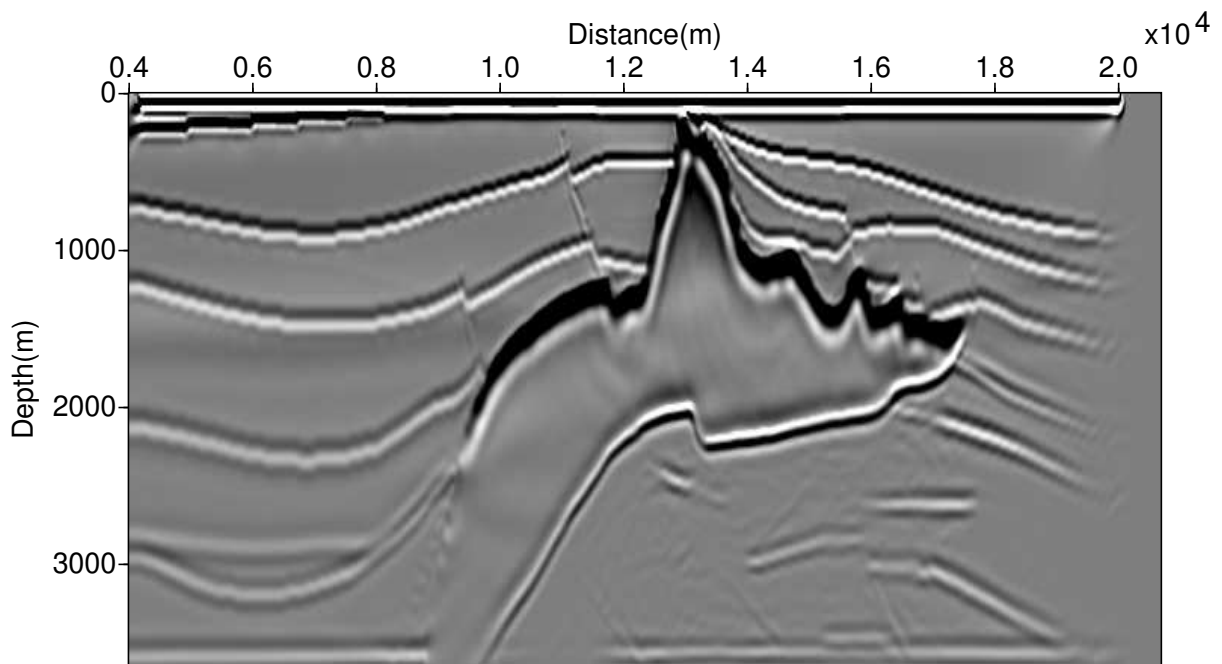


Figure 3.42: Pre-SDM from SEG/EAGE 2D data set using  $\sigma = 1 + p^3$ ,  $N = 3$  and  $\alpha = 45^\circ$ .

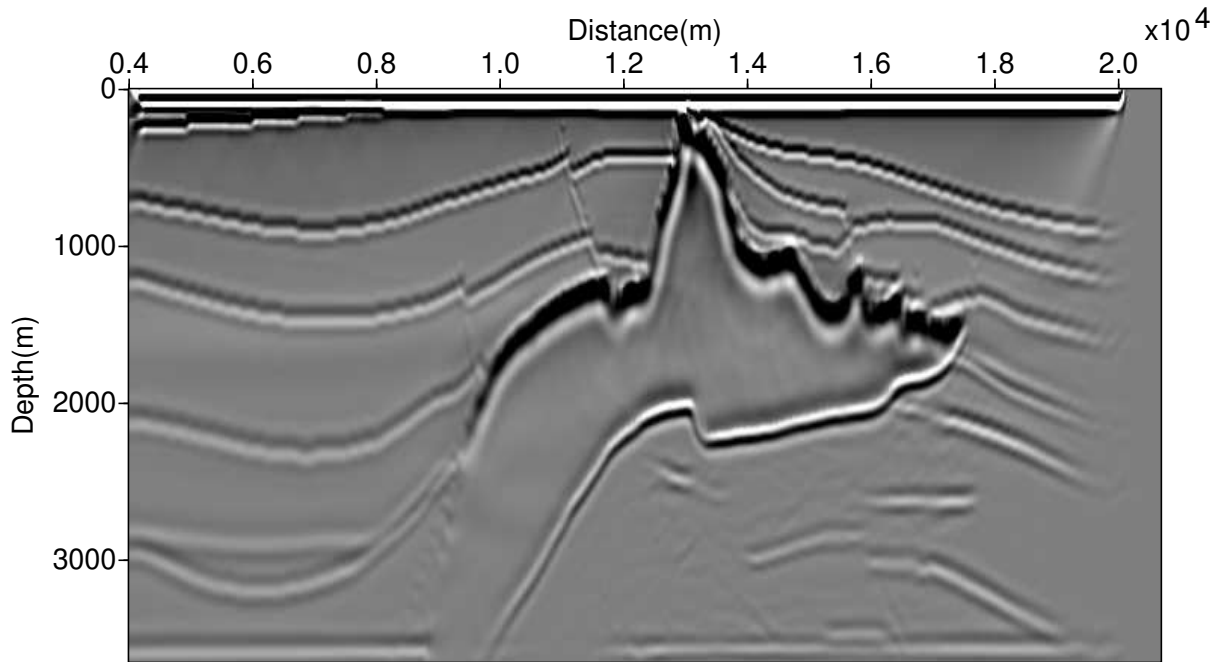


Figure 3.43: Pre-SDM from SEG/EAGE 2D data set using  $\sigma$  from equation 3.4,  $N = 1$  and  $\alpha = 10^\circ$ .

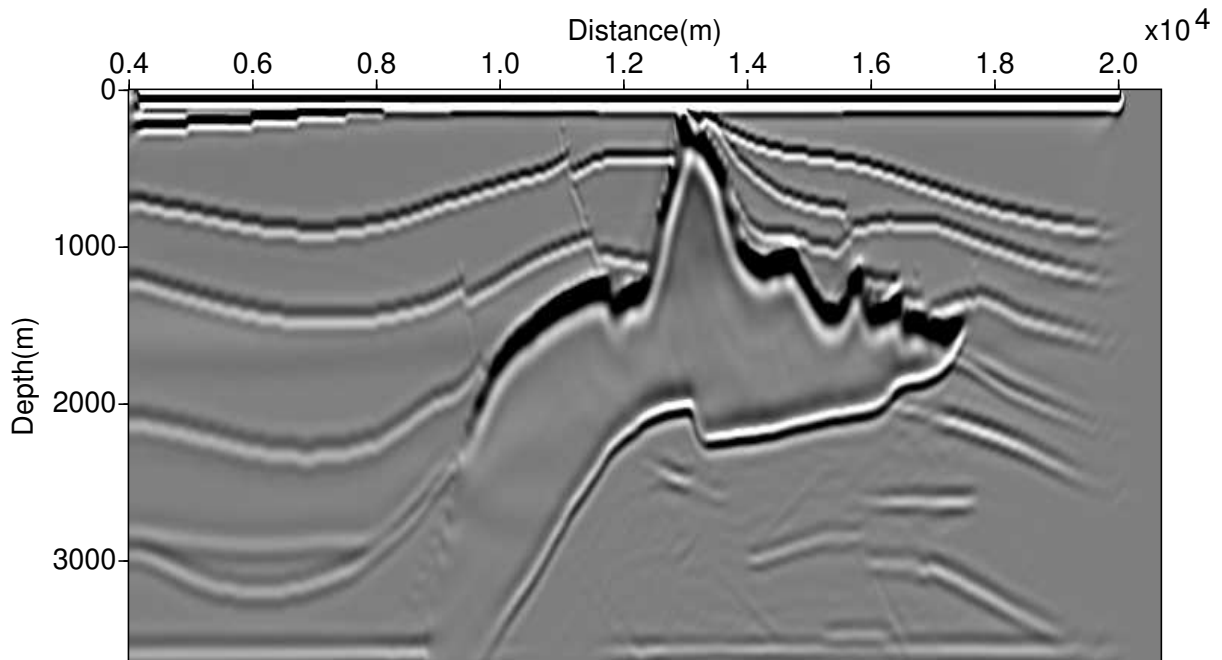


Figure 3.44: Pre-SDM from SEG/EAGE 2D data set using  $\sigma$  from equation 3.5,  $N = 2$  and  $\alpha = 27^\circ$ .

### 3.8 Optimization of one-term complex Padé approximation

In order to further increase the maximum imageable dip using the algorithm with the lowest computational cost, we looked into optimizing the one-term complex Padé approximation itself. In this section we explain the experiments done. First, we begin with a general approximation of the form

$$\sqrt{1-X} \approx 1 - \frac{aX}{1-bX}, \quad (3.7)$$

where now  $a$  and  $b$  are numerical values instead of the theoretical real Padé coefficients using one term, i.e.,  $a_1 = 1/2$  and  $b_1 = 1/4$ . First we study the real part, then we explain our decision for the imaginary part.

Based on the theoretical definition of the real Padé coefficients,  $a$  and  $b$  have values only between 0 and 1. Considering this, we do again a relative error analysis, testing all the possible values of both  $a$  and  $b$ , between 0 and 1, that make the one percent error possible. The relative error is defined by

$$E(X) = \frac{\varepsilon}{\sqrt{1-X}} * 100, \quad (3.8)$$

where  $\varepsilon$  is the difference between the square root and its approximation in equation 3.7. In Figure 3.45 we find the optimal values of which are

$$a = 0.448$$

$$b = 0.445$$

and using them in equation 3.7, we obtain Figure 3.46 that also shows the curve using the first term of the real Padé expansion.

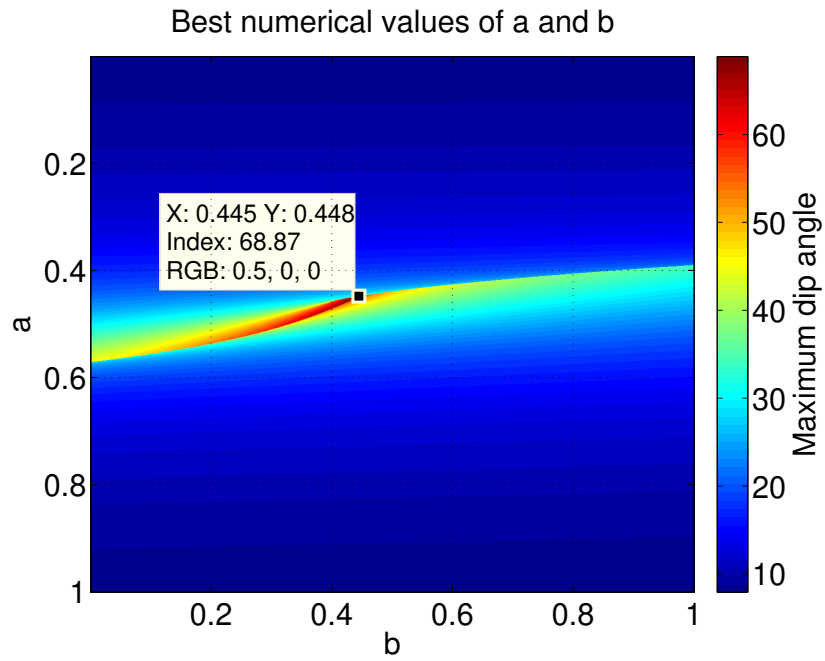


Figure 3.45: Color-coded image evaluating all the possible values of  $a$  and  $b$

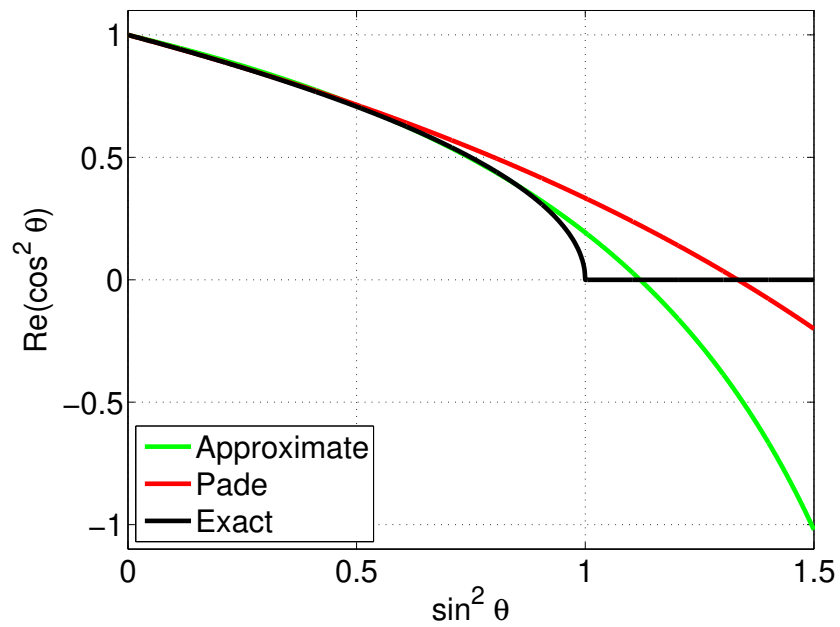


Figure 3.46: Approximation of the real part

Now, we look into the imaginary part. For this, we use the  $a$  and  $b$  optimized parameters in the complex Padé coefficients of Milinazzo et al. (1997) defined as  $A$  and  $B$  respectively.

We minimized the Euclidean norm of the exact square root and the approximation in equation 3.7, testing all the possible values of alpha between 0 and  $\pi/2$ . Additionally, we considered the real and the imaginary part, even from the exact square root as well as the complex Padé approximation. Our objective function contained the variables

$$\begin{aligned}
 A &= \frac{ae^{-\frac{i\alpha}{2}}}{[1 + b(e^{-i\alpha} - 1)]^2} \\
 B &= \frac{be^{-i\alpha}}{1 + b(e^{-i\alpha} - 1)} \\
 fre &= \sqrt{1 - X}, \quad 0 < X < 1 \\
 fim &= \sqrt{1 - X}, \quad 1 < X < 1.5 \\
 Aux1 &= \left\| fre - \operatorname{Re} \left( 1 + \frac{AX}{1 - BX} \right) \right\|_2, \quad 0 < X < 1 \\
 Aux2 &= \left\| fre - \operatorname{Im} \left( 1 + \frac{AX}{1 - BX} \right) \right\|_2, \quad 0 < X < 1 \\
 Aux3 &= \left\| fim - \operatorname{Re} \left( 1 + \frac{AX}{1 - BX} \right) \right\|_2, \quad 1 < X < 1.5 \\
 \text{Objective function} &= Aux1 + Aux2 + Aux3
 \end{aligned} \tag{3.9}$$

The idea was to split the vector  $X$  between the real and the imaginary part, also considering the same for the complex coefficients. Then, find the value of alpha that gives us the minimum value of our objective function. The result was the minimum value of alpha, i.e., the first value, almost zero

$$\alpha = 0.01,$$

the result is presented on Figure 3.47.

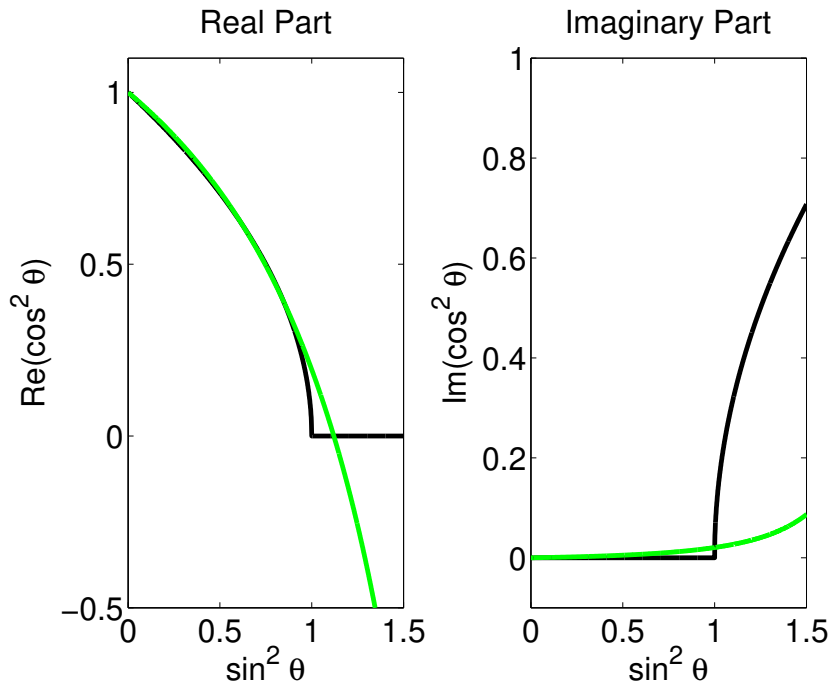


Figure 3.47: Approximation of the square root, improving the imaginary part, first attempt, optimizing only alpha

As we demonstrated before, the use of a very small alpha is not enough in order to damp the evanescent modes. One of our conclusions was the use of  $\alpha = 10^\circ$  based on the quality of the migrated images. Since our first experiment didn't work, we redefined the complex coefficients, now using the general expression for complex numbers, i.e.,

$$\begin{aligned} A &= ae^{-i\alpha}, \\ B &= be^{-i\beta}. \end{aligned}$$

We then performed the same experiment as before, i.e., we used the same objective function of equation 3.9. The idea was to have one more degree of freedom by using the new parameter  $\beta$ . Unfortunately, again, the result was the same as our first experiment, i.e., the optimum values of  $\alpha$  and  $\beta$  were always the minimum possible value. For this second experiment, the values were

$$\begin{aligned} \alpha &= 0.01, \\ \beta &= 0.02. \end{aligned}$$

The resulting approximation of the square root in Figure 3.48 is almost the same as the one in Fig-

ure 3.47. Thus, we concluded that there is no need for the use of another parameter. Indeed, using only  $\alpha$  we obtain almost the same effect on the imaginary part and we may continue with the theoretical definition of the complex Padé coefficients.

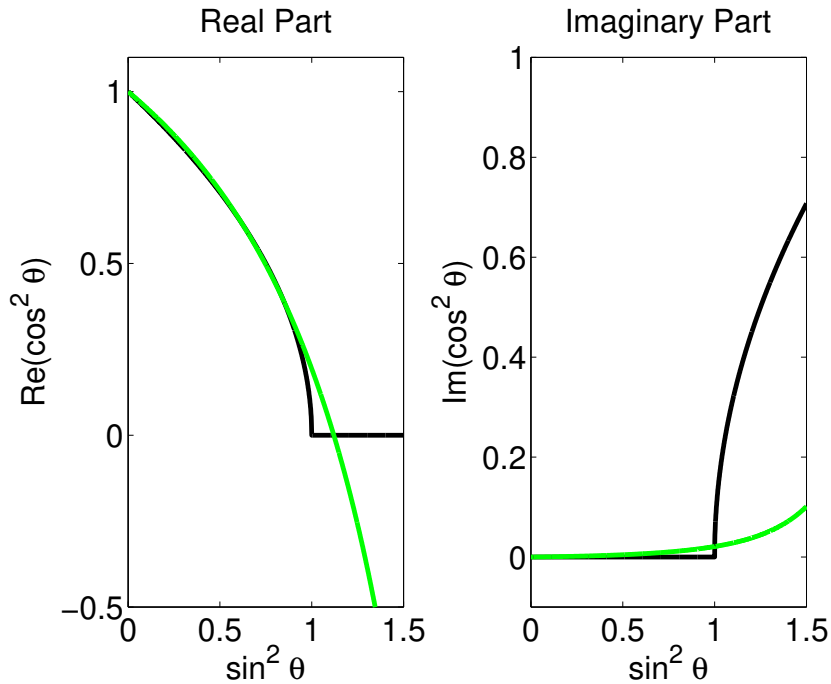


Figure 3.48: Approximation of the square root, improving the imaginary part, second attempt, optimizing alpha and beta

Thus, we decided to fix  $\alpha = 10^\circ$  because of our previous results on the migrated images, but now using  $a = 0.448$  and  $b = 0.445$  as our optimized parameters, in our complex coefficients

$$A = \frac{ae^{-\frac{i\alpha}{2}}}{[1 + b(e^{-i\alpha} - 1)]^2}, \quad B = \frac{be^{-i\alpha}}{1 + (e^{-i\alpha} - 1)}.$$

The resulting approximation of the square root is shown in Figure 3.49.

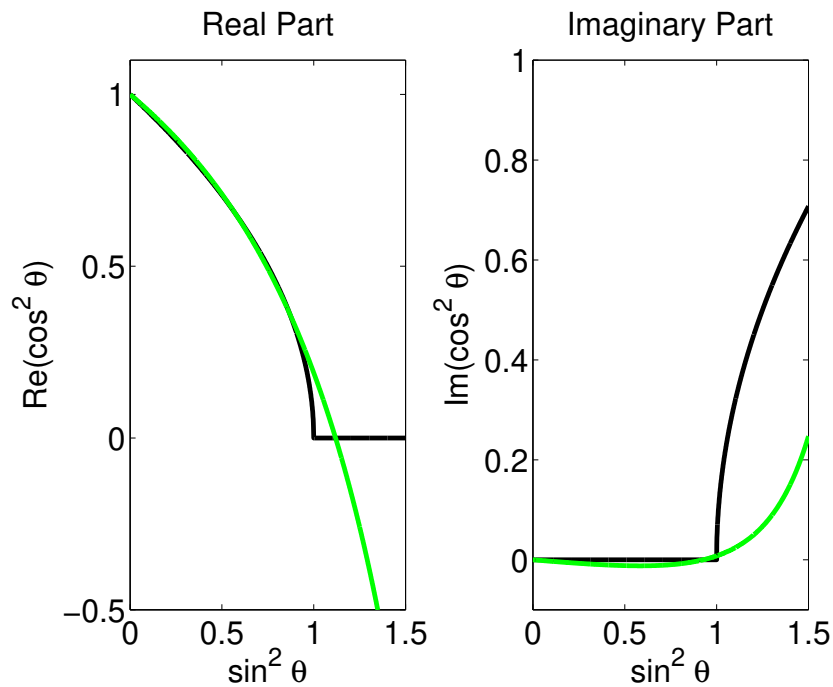


Figure 3.49: Approximation of the square root, using the optimized  $a$  and  $b$  parameters, and the original complex Padé coefficients with  $\alpha = 10^\circ$ .

### 3.8.1 Optimized $\sigma$ for the one-term complex Padé approximation, using the optimized Padé coefficients

Having the optimization of  $a$ ,  $b$  and considering  $\alpha = 10^\circ$ , the idea is introduce these parameters in the CPFFD algorithm, then find the optimal value of  $\sigma$  using the same analysis explained before, i.e., based on the one percent relative error. The outcomes were positive, and the maximum dip angles attained were even higher than those obtained using the Real FFD algorithm, and not really far from the angles using two terms in the Padé expansion which is greater only for not very realistic values of  $p$ . Figure 3.50 is one of the most important figures in our research because it shows a comparison of all our best outcomes.

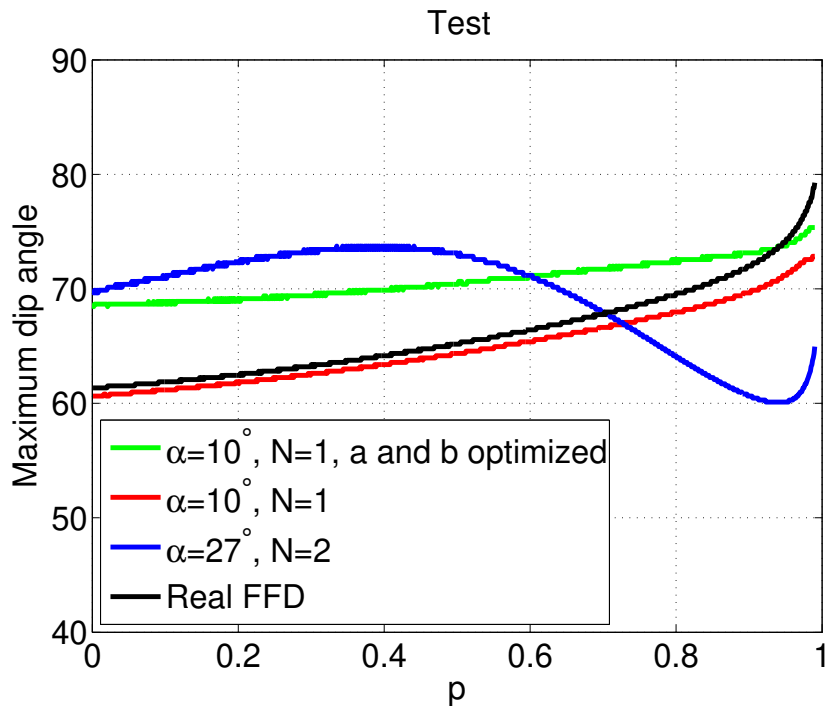


Figure 3.50: Angles obtained with CPFFD using the optimized  $\sigma$ ,  $a$  and  $b$ , compared with last results and real FFD of Ristow and Rühl (1994).

In order to follow the same pattern, Figure 3.51 shows the maximum dip angle obtained for each value of  $\sigma$  and  $p$ , and Table 3.4 summarises the optimum  $\sigma$  values for  $p$  between 0.001 and 0.99. Unlike the outcome without the optimization of the Real Padé coefficients, now  $\sigma$  is between 1 and 2.2. Furthermore, it is possible to observe the superiority on the red color compared with our past results, with maximum dip angles higher than  $69^\circ$  and reaching values up to  $75^\circ$ .

Then, we may analyse the algorithm's behavior, in dependence of the lateral velocity variation, using for this, Figures 3.52, 3.53 and 3.54. Something interesting is the fact that the new approximation achieves almost  $70^\circ$  in the presence of strong velocity variations as we may see in Figure 3.52, completely different from our past result using one term and without the optimization of the Real Padé coefficients.

$p$	$\sigma$	$\theta_m$
0.001	0.991	68.67
0.05	1.017	68.67
0.10	1.049	68.67
0.15	1.077	68.91
0.20	1.109	68.91
0.25	1.144	69.15
0.30	1.181	69.39
0.35	1.220	69.64
0.40	1.261	69.88
0.45	1.305	70.14
0.50	1.351	70.39
0.55	1.400	70.91
0.60	1.452	71.17
0.65	1.507	71.44
0.70	1.566	71.71
0.75	1.630	71.99
0.80	1.700	72.27
0.85	1.778	72.84
0.90	1.869	73.14
0.95	1.984	73.74
0.99	2.128	75.35

Table 3.4: Maximum dip angle using the optimal value of  $\sigma$ , optimized  $a$  and  $b$  parameters and  $\alpha = 10^\circ$

Furthermore, the angles obtained, while the value of  $p$  increases, follow the same pattern as in the previous analysis, i.e., an increasing tendency of the maximum dip angles, which matches with the theory of Ristow and Rühl (1994) because in their work they showed that a small value of  $p$  represents also a small dip angle attained, conversely a high value of  $p$  gives a high value of the dip angle, using the optimal value of  $\sigma$ . It should be emphasized that our results using  $N = 2$  do not match with this theory.

On the other hand, an important analysis is always concerning the relative error, Figure 3.55 shows a maximum dip angle of  $70.39^\circ$  which is not really far from the much expensive two-term CPFFD which obtained  $73^\circ$ .

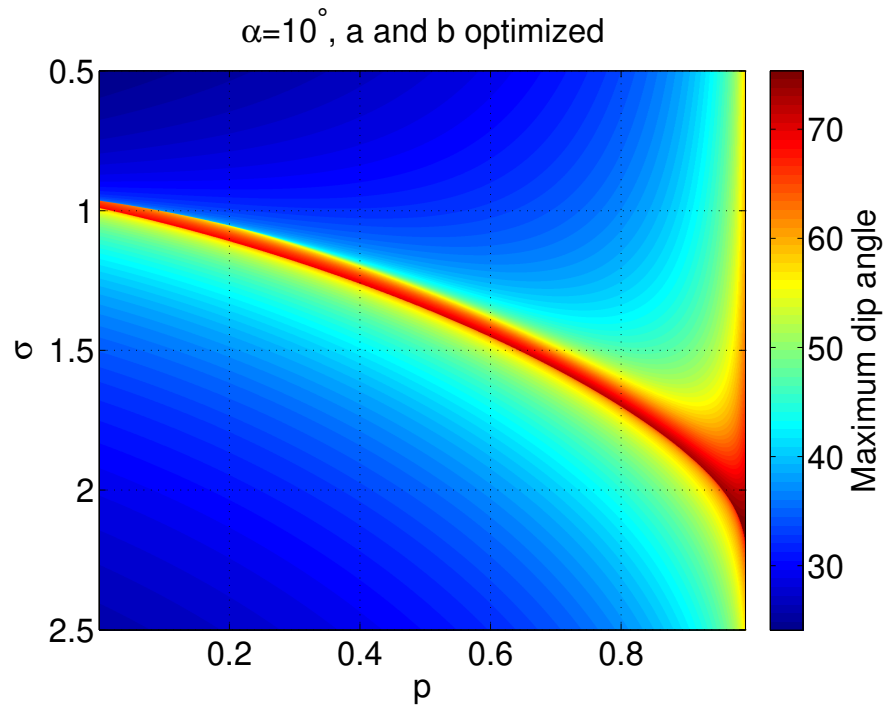


Figure 3.51: Maximum dip-angle values as a function of  $p$  and  $\sigma$  for the complex Padé approximation using  $\alpha = 10^\circ$ ,  $N = 1$ ,  $a$  and  $b$  optimized.

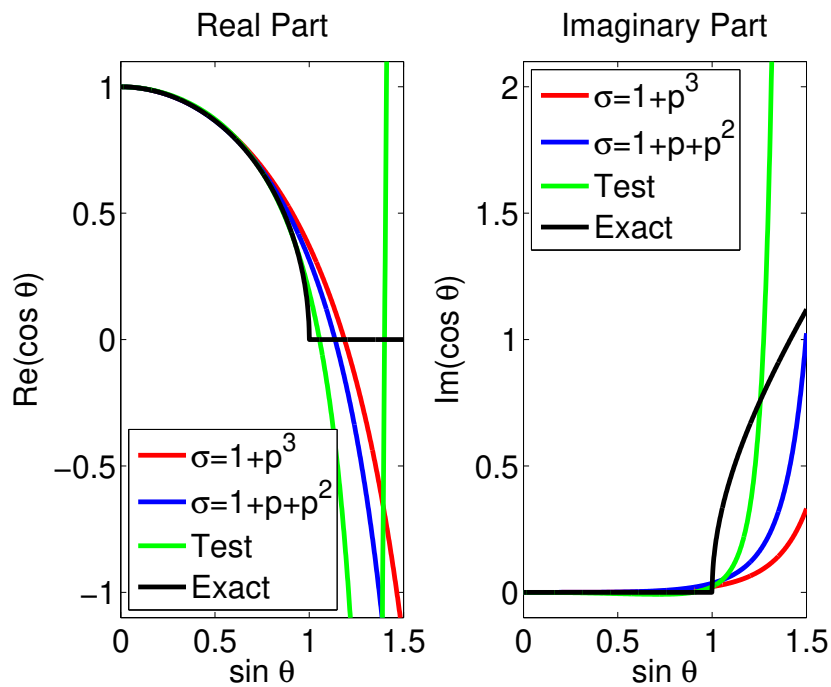


Figure 3.52: Dispersion relation with strong lateral velocity variation,  $p = 0.25$ ,  $a$  and  $b$  optimized.

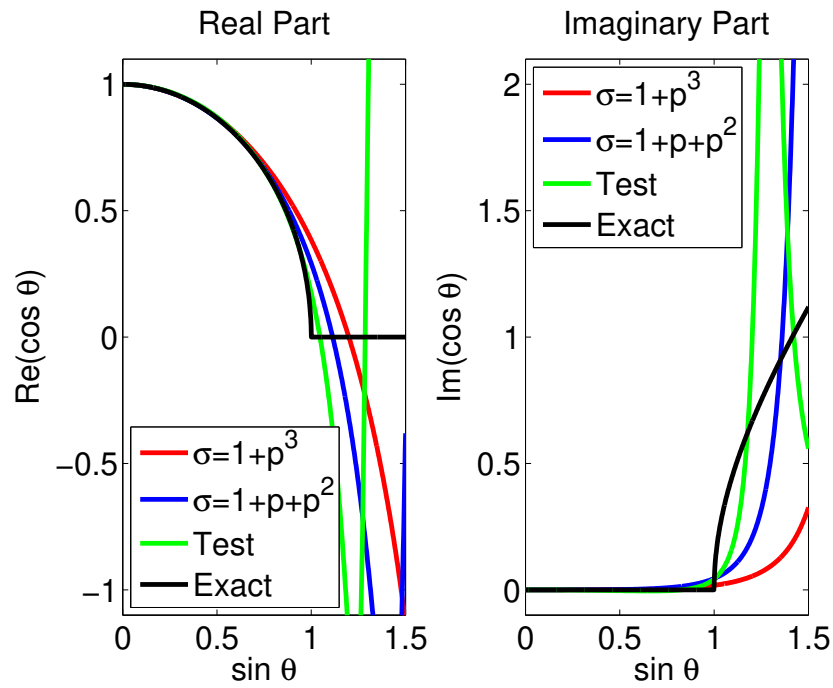


Figure 3.53: Dispersion relation with intermediate lateral velocity variation,  $p = 0.5$ ,  $a$  and  $b$  optimized.

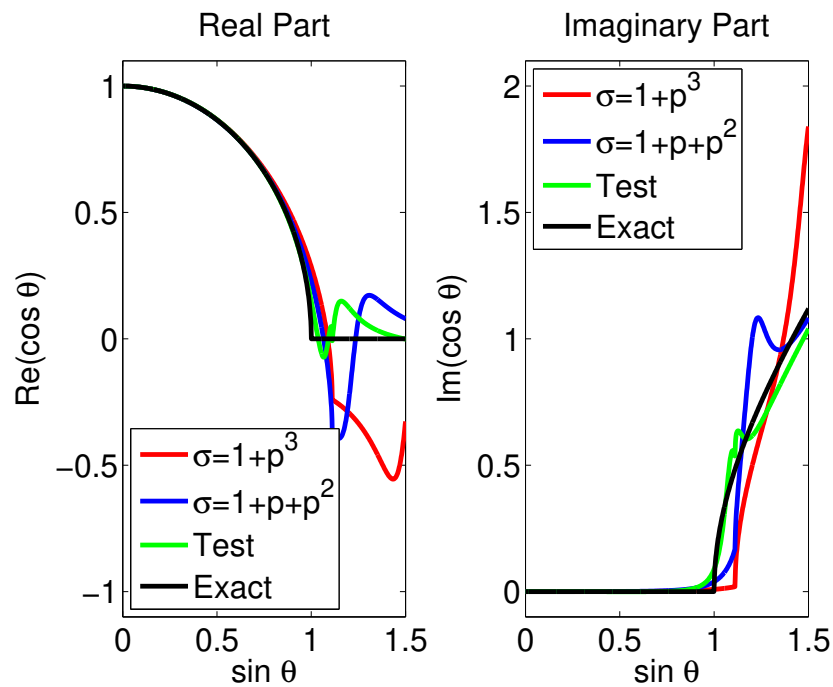


Figure 3.54: Dispersion relation with small lateral velocity variation,  $p = 0.9$ ,  $a$  and  $b$  optimized.

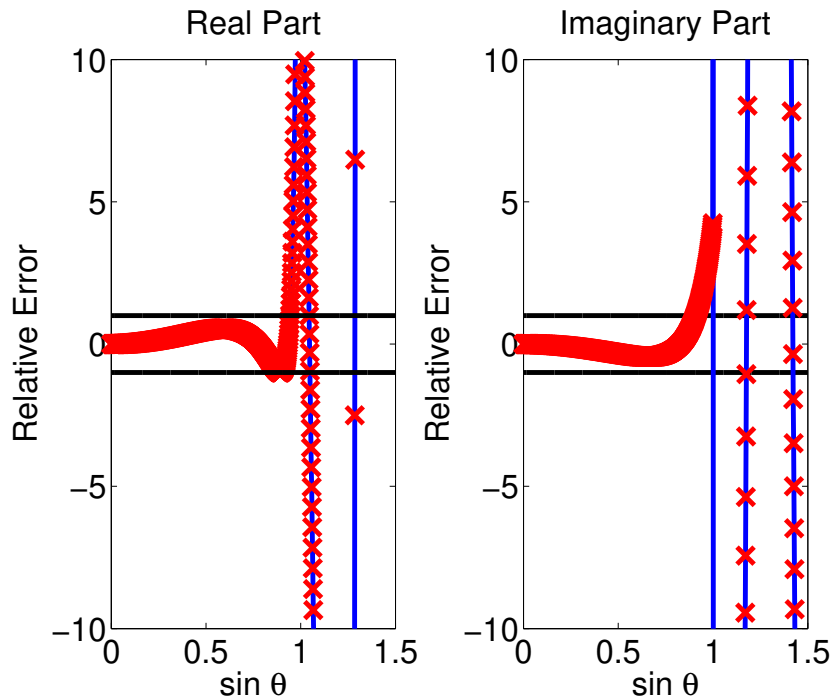


Figure 3.55: Relative error of optimized  $\sigma$ , using intermediate lateral velocity variation,  $p = 0.5$ ,  $a$  and  $b$  optimized.

### 3.8.2 Simple function $\sigma(p)$ for $N = 1$ , $\alpha = 10^\circ$ and using the optimized $a$ and $b$ parameters

Finally, it is time to define a function for our new values of  $\sigma$ , and fortunately, as our previous test for  $N = 1$ , was easily adjusted with a polynomial fit, using also a 4rd-order polynomial

$$\sigma = 0.9996 + 0.276p + 1.745p^2 - 2.64p^3 + 1.74p^4. \quad (3.10)$$

Figure 3.56 shows the fitting of our new polynomial.

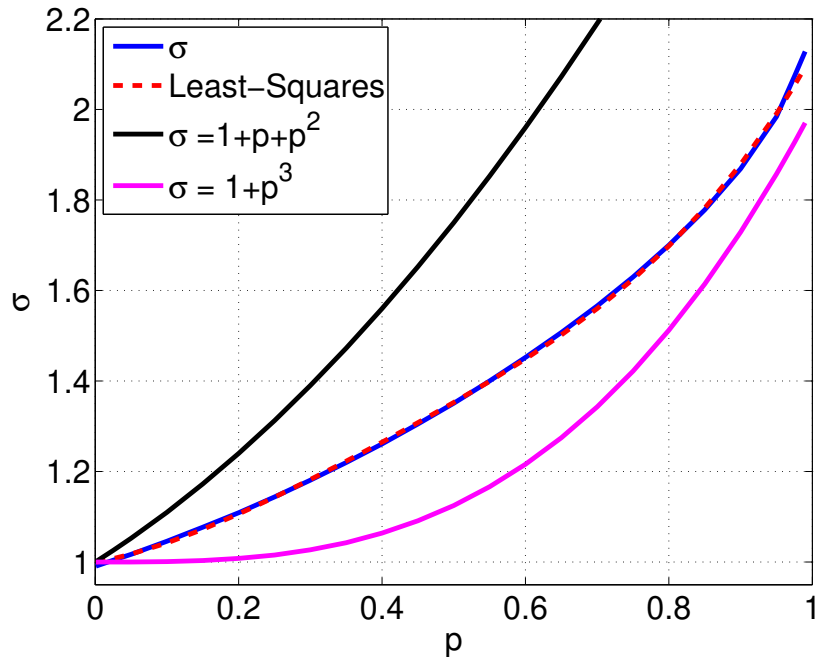


Figure 3.56: Optimized  $\sigma$  function versus least-squares using  $a$  and  $b$  optimized.

### 3.9 Migration results

In this section we present the CPFFD migrated image using the optimized  $a$  and  $b$  parameters. The imaging condition, peak frequency and sampling interval is the same as in section 3.7. We expect to get a better image than the one with the theoretical Real Padé values. For this, we start migrating the Marmousi velocity model, the first comparison is between Figure 3.57 and Figure 3.58, and the improvement is remarkable, there are critical areas that are much better using  $a$  and  $b$  optimized which are marked with red frames. In general Figure 3.57 is superior to Figure 3.58.

Secondly, Figure 3.57 should be compared with the much more expensive two and three-terms CPFFD presented in Figure 3.59 and Figure 3.60, respectively. Here, the three images have only small differences, it is impossible to decide which one is better, but again, an important factor besides the quality, is the computational cost, because using  $a$  and  $b$  optimized, implies the use of only one term, and as we may see, the faults and critical points are completely visible.

On the other hand, Figure 3.61 shows the migrated image of the same model, using now the Real FFD of Ristow and Rühl (1994), additionally, we use the optimized  $\sigma$  instead of the theoretical function ( $\sigma = 1 + p + p^2$ ), and we use only one term. We chose the parameters in this way because these are the same parameters used by Ristow and Rühl (1994). In terms of compare migrations under the same conditions, we found it only fair to use the optimized  $\sigma$ . Basically, the purpose was to show the effect of the evanescent modes, and even if we may see the faults, something remarkable is the

presence of many artifact which are marked with red frames in Figure 3.61.

We migrated also the SEG/EAGE salt model, comparing first the algorithm using the optimized  $a$  and  $b$  parameters in Figure 3.62 with the much more expensive two and three-term approximations, in Figure 3.63 and Figure 3.64, respectively. Again, it is possible to identify all the major faults position on the three images. At the top of the salt in Figure 3.62 we may see a slight improvement compared with the use of two terms in Figure 3.63, while the use of three terms don't represent significant differences. The savings in computation time over the three-term operator are the same as for the Marmousi data, i.e., 42% for  $N = 1$  and 13% for  $N = 2$ .

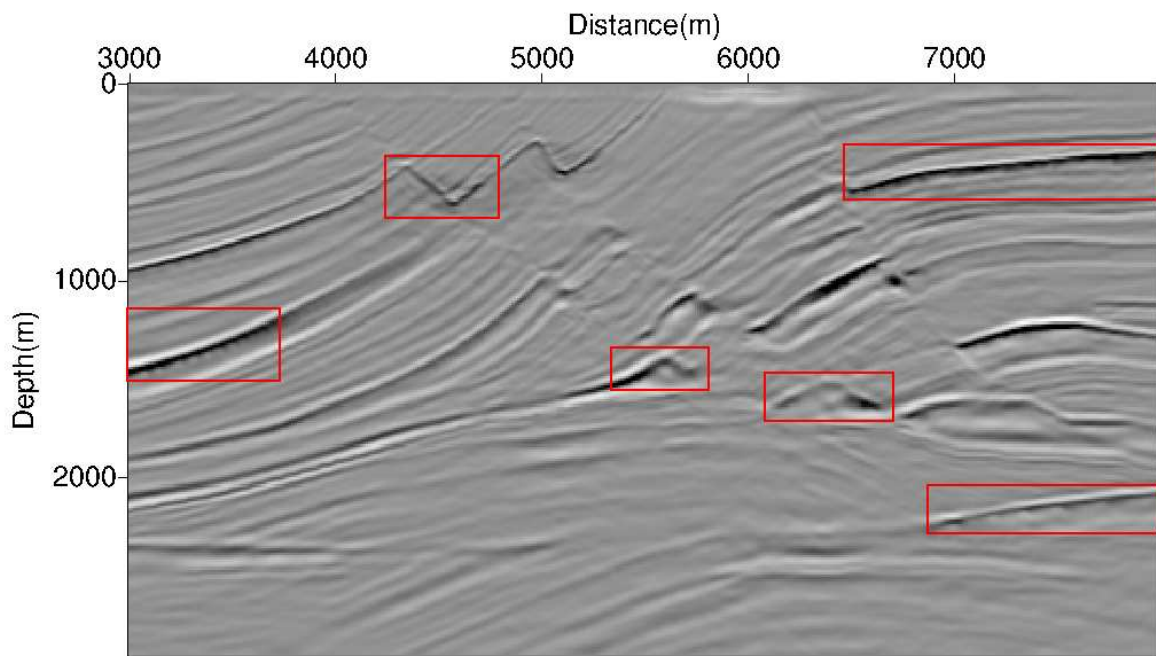


Figure 3.57: Pre-SDM of Marmousi data set using  $\sigma$  from polynomial in equation 3.10,  $N = 1$ ,  $\alpha = 10^\circ$ , and the optimized  $a$  and  $b$  parameters.

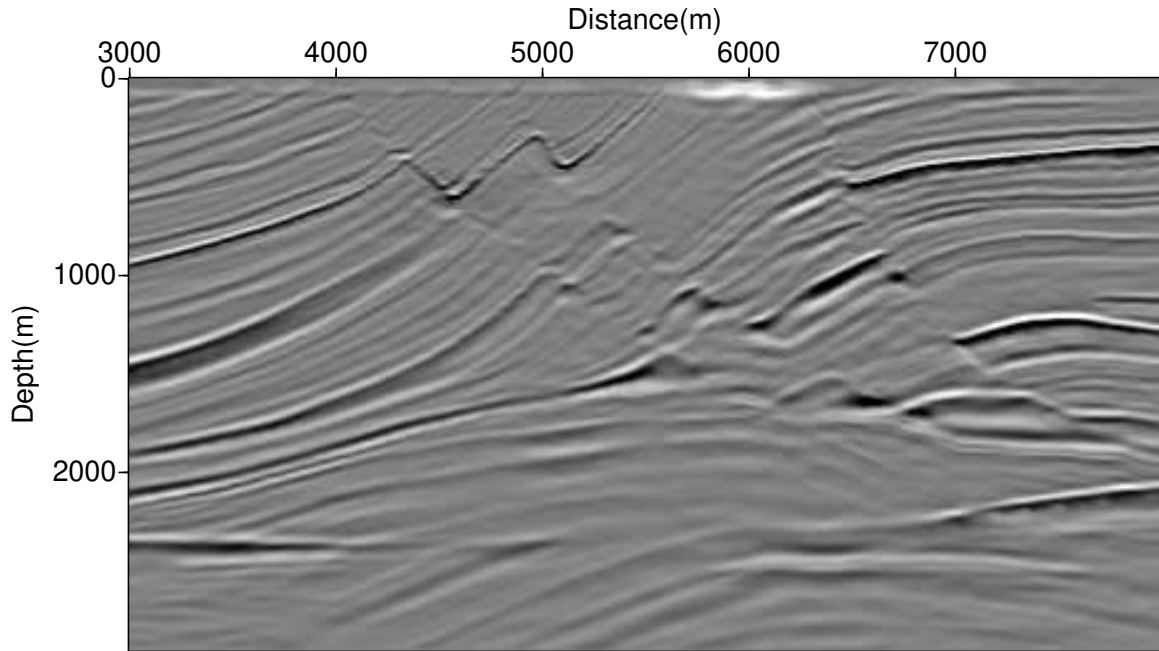


Figure 3.58: Pre-SDM of Marmousi data set using  $\sigma$  from equation 3.4,  $N = 1$ ,  $\alpha = 10^\circ$ .

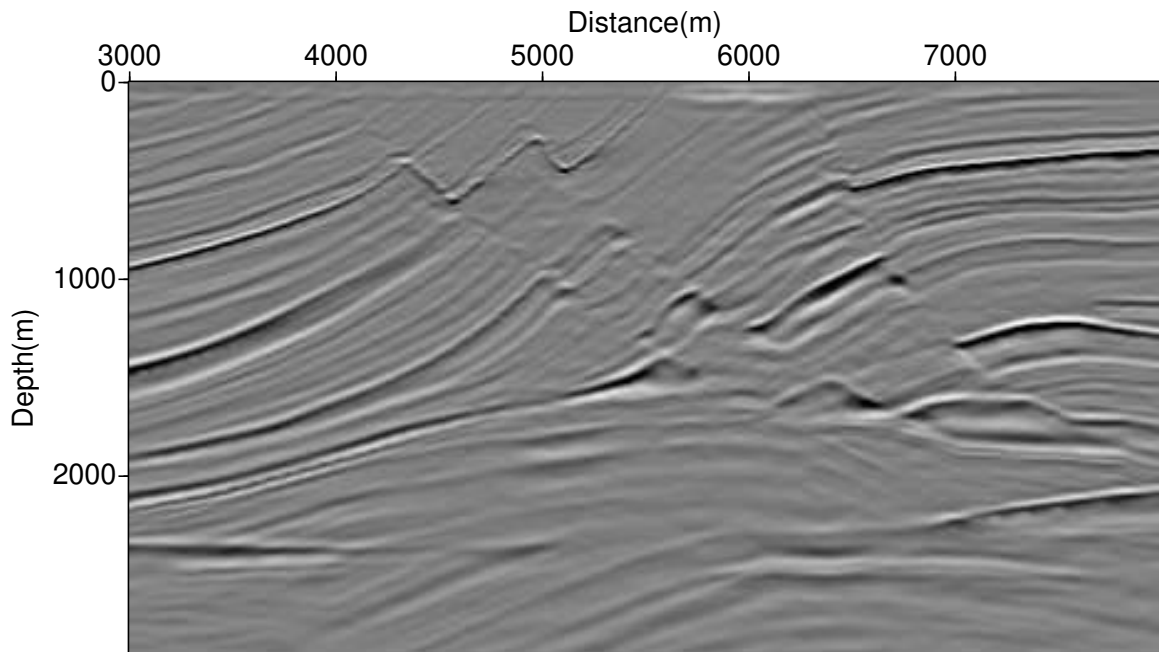


Figure 3.59: Pre-SDM of Marmousi data set using  $\sigma$  from equation 3.5,  $N = 2$ ,  $\alpha = 27^\circ$ .

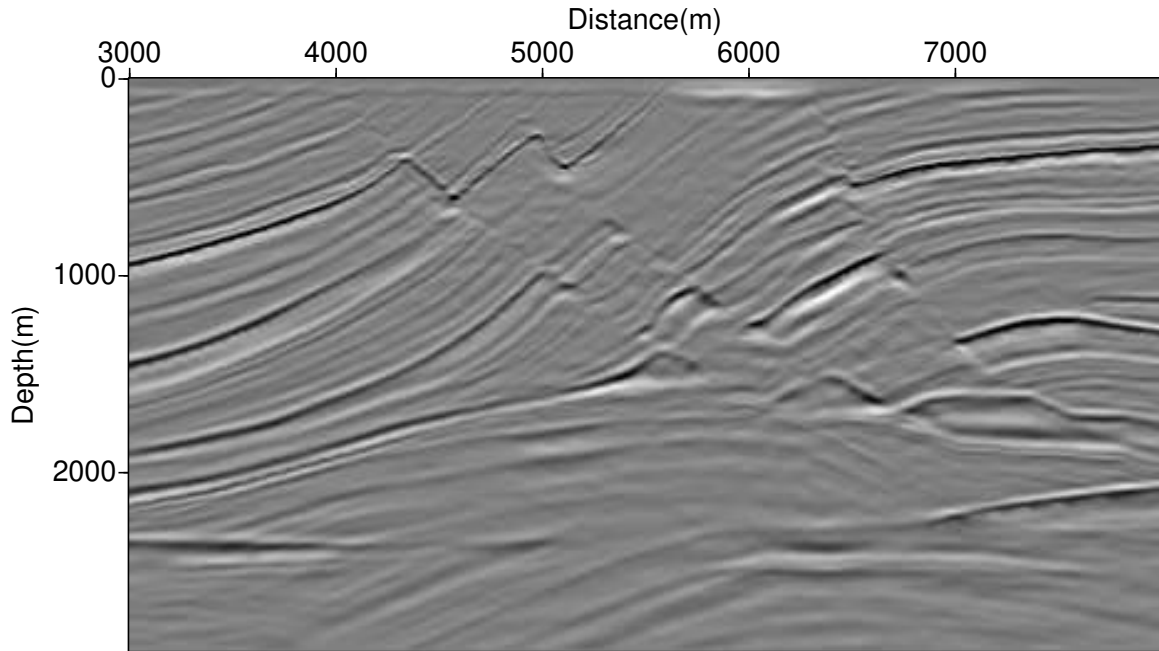


Figure 3.60: Pre-SDM of Marmousi data set using  $\sigma = 1 + p^3$ ,  $N = 3$ ,  $\alpha = 45^\circ$ .

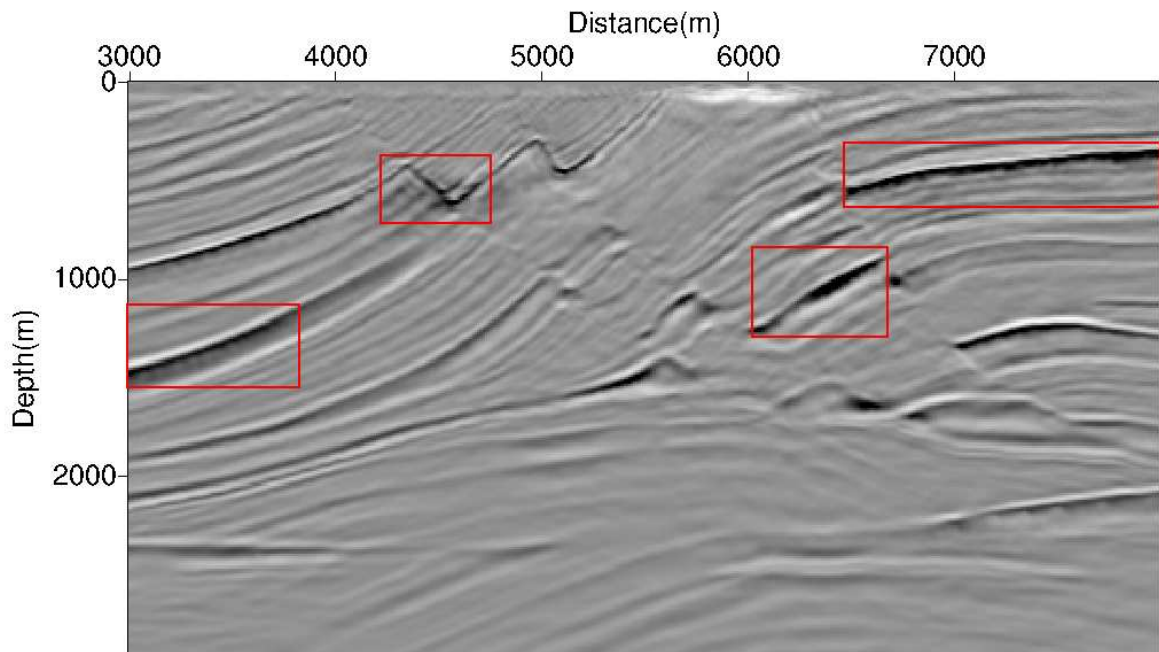


Figure 3.61: Pre-SDM of Marmousi data set using Real FFD and optimized  $\sigma$

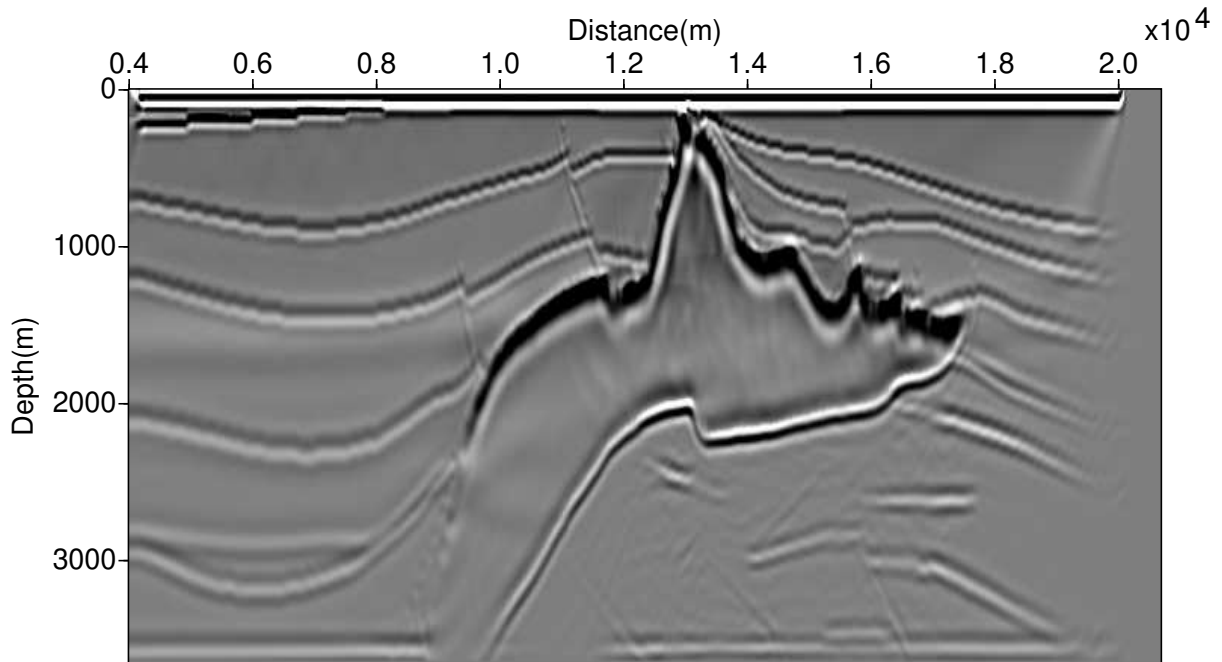


Figure 3.62: Pre-SDM from SEG/EAGE 2D data set using  $\sigma$  from polynomial in equation 3.10,  $N = 1$ ,  $\alpha = 10^\circ$ , and the optimized  $a$  and  $b$  parameters.

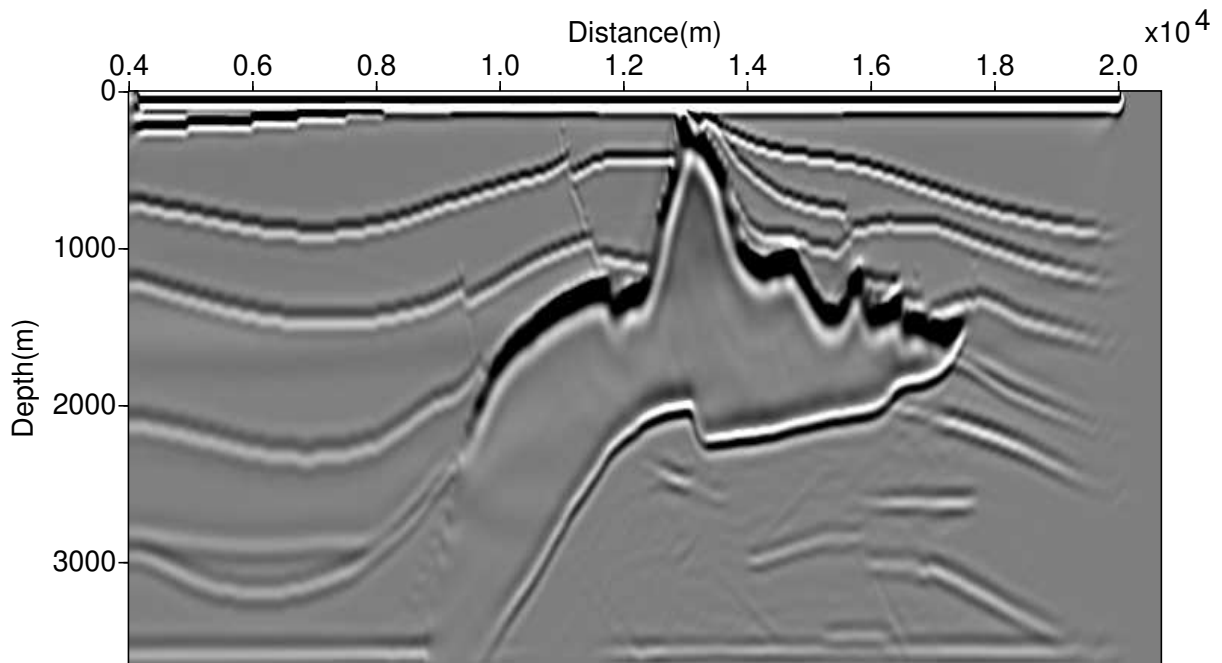


Figure 3.63: Pre-SDM from SEG/EAGE 2D data set using  $\sigma$  from equation 3.5,  $N = 2$  and  $\alpha = 27^\circ$ .

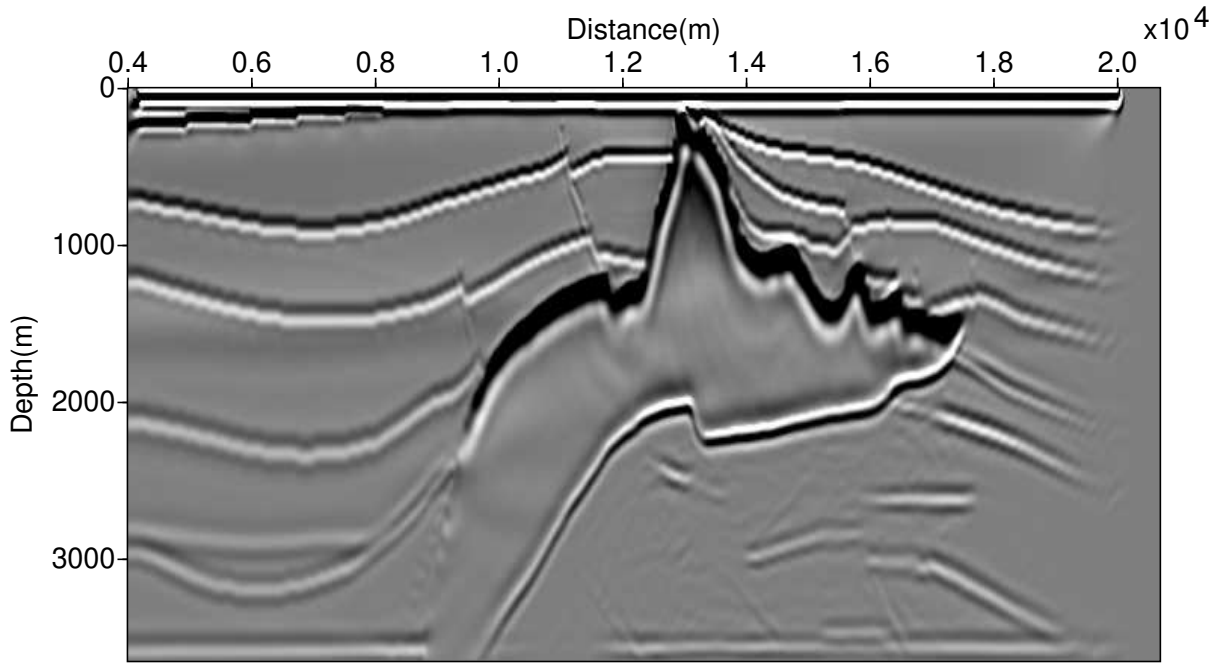


Figure 3.64: Pre-SDM from SEG/EAGE 2D data set using  $\sigma = 1 + p^3$ ,  $N = 3$ ,  $\alpha = 45^\circ$ .

### 3.10 Final recommendation for CPFFD migration

From the above analysis of CPFFD migration, we conclude that the best approximation of the square root is achieved by

$$\sqrt{1 - X^2} \approx \frac{\sqrt{1 - p^2 X^2}}{p} + \frac{(p - 1)}{p} - \frac{(1 - p)AX^2}{1 - B\sigma X^2},$$

where the parameters should be chosen according to

$$\begin{aligned} A &= \frac{ae^{-\frac{\alpha}{2}}}{[1 + b(e^{-\alpha} - 1)]^2}, & B &= \frac{be^{-\alpha}}{1 + (e^{-\alpha} - 1)}, \\ a &= 0.448, & b &= 0.445, \\ \alpha &= 10^\circ = 0.1745 \text{ radians}, \\ \sigma &= 0.9996 + 0.276p + 1.745p^2 - 2.64p^3 + 1.74p^4. \end{aligned}$$

The results using these parameters achieved the same quality as earlier parameterizations at 42% reduced computational cost.

## 4. Conclusions

In this work, we have investigated the optimization of the parameters used in the complex-Padé FFD algorithm in order to extend the range of imageable reflector dips. Our original aim was to optimize the velocity-dependent parameter  $\sigma$  in the complex Padé FFD approximation. For this purpose, we determined, for each velocity ratio, the value of  $\sigma$  that made a one-percent error of the dispersion relation occur at the largest possible dip angle. Using these optimized  $\sigma$  functions, we noticed the need to reevaluate the branch-cut rotation angle  $\alpha$  and the number of terms in the complex Padé expansion, because the algorithm behaves differently for better  $\sigma$  than for the theoretical expression or a heuristic function.

As a general observation, an increase in the rotation angle leads to a loss in imageable maximum dip angles. The use of a third term in the Padé expansion cannot compensate for this effect, except where the model velocity is larger than five times the reference velocity. Moreover, the third term adds significantly to the computation cost. Therefore the use of three Padé terms is not recommendable.

For the one and two-term Padé expansions, our study lead to recommendable rotation angles. These recommendations are based on the damping of the evanescent modes and the maximum dip angle. Our first result is that the highest maximum dip angles of more than 60 degrees can be reached with a one-term Padé approximation with a small branch-cut rotation angle of  $10^\circ$ . This angle is already sufficient to introduce acceptable damping of the evanescent waves, while at the same time reaching the same maximum dip angles as real-Padé FFD, if an optimized  $\sigma$  function is used. While smaller rotation angles allow to even reach slightly higher dip angles, they do not introduce sufficient damping to remove the artifacts caused by incorrect treatment of evanescent waves. Therefore, smaller rotation angles present no advantage over a real approximation. The best rotation angle for the two-term approximation is  $27^\circ$ . However, surprisingly, using two terms in the Padé expansion leads to higher maximum dip angles only for velocity ratios below 0.7.

Since the one-term approximation turned out to be the best option for velocity ratios above 0.7, and since it is the most economic operator anyway, we looked into further optimization. Instead of using the theoretical Padé coefficients, we also optimized the coefficients for the underlying Padé approximation of the square root. With these numerical values in the CPFFD operator and the corresponding

optimized  $\sigma$  values, it was possible to reach even higher dip angles.

The optimized values for  $\sigma$  in dependence on the velocity ratio can be well-adjusted by simple equations that make them readily accessible. The optimal  $\sigma$  function for the one-term,  $10^\circ$  approximation turned out to be a smooth curve that could be nicely adjusted with a 4th-order polynomial. For the two-term,  $27^\circ$  approximation, we added a logarithmic term in order to better adjust the numerical values.

We tested the so-constructed optimized CPFFD operator by means of migrating the Marmousi and SEG/EAGE sat data. The resulting migrated images are comparable in terms of quality to earlier results, obtained with a more expensive operator. On the other hand, the image using our fully optimized one-term operator shows remarkable differences with the one that uses the theoretical values. Thus, we conclude that it is possible to reach maximum dip angles up to 75 degrees upon the use of a one-term CPFFD operator that also reduces the artifacts caused by incorrect treatment of evanescent waves.

In terms of computational cost, in realistic velocity models like the Marmousi and SEG/EAGE models, the one and two-term approximations achieved a 42% and 13% reduction, respectively, over the three-term approximation of Amazonas et al. (2007).

## References

- Amazonas, D., Aleixo, R., Melo, G., Schleicher, J., Novais, A., and Costa, J. C. (2010). Including lateral velocity variations into true-amplitude common-shot wave-equation migration. *Geophysics*, 75(5):S175–S186.
- Amazonas, D., Costa, J. C., Schleicher, J., and Pestana, R. (2007). Wide-angle FD and FFD migration using complex Padé approximations. *Geophysics*, 72(6):S215–S220.
- Aminzadeh, F., Burkhard, N., Nicoletis, L., and Rocca, F. (1995). 3-D modeling project—3rd report. *The Leading Edge*, 14:125–128.
- Bamberger, A., Engquist, L. H., and Joly, P. (1988). Higher order paraxial wave equation approximations in heterogeneous media. *Journal of Applied Mathematics*, 48:129–154.
- Biondi, B. (2002). Stable wide-angle Fourier finite-difference downward extrapolation of 3-D wavefields. *Geophysics*, 67(3):872–882.
- Biondi, B. (2006). 3D seismic imaging. *SEG Investigations in Geophysics, No. 14*.
- Claerbout, J. F. (1985). Imaging the earth's interior. *Blackwell Scientific Publications, Inc.*
- Costa, J. C., Mondini, D., Schleicher, J., and Novais, A. (2011). A comparison of splitting techniques for 3d complex Padé Fourier finite difference migration. *International Journal of Geophysics*, 2011:Article ID 714781, 12 pages.
- Gazdag, J. (1978). Wave equation migration with the phase-shift method. *Geophysics*, 43:1342–1351.
- Gazdag, J. and Sguazzero, P. (1984). Migration of seismic data by phase-shift plus interpolation. *Geophysics*, 49:124–131.
- Han, B. (2000). A comparison of four closely related depth migration methods. *Master's thesis, Colorado School of Mines.*

- Kessinger, W. (1992). Extended split-step Fourier migration. *62nd Annual International Meeting of the Society of Exploration Geophysicists*. Expanded Abstract, 917–920.
- Milinazzo, F. A., Zala, C. A., and Brooke, G. H. (1997). Rational square-root approximations for parabolic equation algorithms. *The Journal of the Acoustical Society of America*, 101(2):760–766.
- Ristow, D. and Rühl, T. (1994). Fourier finite-difference migration. *Geophysics*, 59(12):1882–1893.
- Stoffa, P. L., Fokkema, J. T., de Luna Freire, R. M., and Kessinger, W. P. (1990). Split-step Fourier migration. *Geophysics*, 55:410–421.
- Versteeg, R. (1994). The Marmousi experience: Velocity model determination on a synthetic complex data set. *The Leading Edge*, 13(9):927–936.
- Wapenaar, K., Thorbecke, J., van der Neut, J., Broggini, F., Slob, E., and Snieder, R. (2014). Marchenko imaging. *GEOPHYSICS*, 79(3):WA39–WA57.

## A. Definition of the complex Padé coefficients

In this appendix we define the complex Padé coefficients of Milinazzo et al. (1997). The derivation follows the one of Amazonas et al. (2007).

In particular, rational approximations of the form

$$R_N(Z) = 1 + \sum_{n=1}^N \frac{a_n Z}{1 + b_n Z}, \quad (\text{A.1})$$

to  $\sqrt{1+Z} \approx R_N(Z)$  are of interest for parabolic equation algorithms since they can provide good estimates for use in equation 2.6, where  $Z = \frac{v(x,z)^2}{\omega^2} \frac{\partial^2}{\partial x^2}$ , and allow efficient numerical implementations. As shown in Bamberger et al. (1988), the real-valued coefficients

$$a_n = \frac{2}{2N+1} \sin^2 \left( \frac{n\pi}{2N+1} \right) \quad \text{and} \quad b_n = \cos^2 \left( \frac{n\pi}{2N+1} \right)$$

correspond to Padé approximations of the square root with branch cut along the negative real line from  $Z = -1$ . Rotating the principal branch into the lower complex plane, the square-root may be represented as

$$\begin{aligned} S_\alpha(Z) &= e^{i\frac{\alpha}{2}} \sqrt{(1+Z)e^{-i\alpha}} \\ S_\alpha(Z) &= e^{i\frac{\alpha}{2}} \sqrt{1 + [(1+Z)e^{-i\alpha} - 1]}. \end{aligned} \quad (\text{A.2})$$

Using equation A.1 to approximate the square root in equation A.2, we obtain

$$\begin{aligned}
S_\alpha(z) \approx R_{\alpha,N}(Z) &= e^{i\frac{\alpha}{2}} \left[ 1 + \sum_{n=1}^N \frac{a_n [(1+Z)e^{-i\alpha} - 1]}{1 + b_n [(1+Z)e^{-i\alpha} - 1]} \right] \\
&= e^{i\frac{\alpha}{2}} \left[ 1 + \sum_{n=1}^N \frac{a_n e^{-i\alpha} - a_n + a_n e^{-i\alpha} Z}{1 + b_n e^{-i\alpha} - b_n + b_n e^{-i\alpha} Z} \right] \\
&= e^{i\frac{\alpha}{2}} \left[ 1 + \sum_{n=1}^N \frac{a_n (e^{-i\alpha} - 1) + a_n e^{-i\alpha} Z}{1 + b_n (e^{-i\alpha} - 1) + b_n e^{-i\alpha} Z} \right] \\
&= e^{i\frac{\alpha}{2}} \left[ 1 + \sum_{n=1}^N \frac{a_n (e^{-i\alpha} - 1) + a_n e^{-i\alpha} Z}{[1 + b_n (e^{-i\alpha} - 1)] \left[ 1 + \frac{b_n e^{-i\alpha} Z}{1 + b_n (e^{-i\alpha} - 1)} \right]} \right].
\end{aligned}$$

Defining  $B_n \equiv \frac{b_n e^{-i\alpha}}{1 + b_n (e^{-i\alpha} - 1)}$  and separating the summation, we find

$$R_{\alpha,N}(Z) = e^{i\frac{\alpha}{2}} \left[ 1 + \sum_{n=1}^N \frac{a_n (e^{-i\alpha} - 1)}{[1 + b_n (e^{-i\alpha} - 1)] [1 + B_n Z]} + \sum_{n=1}^N \frac{a_n e^{-i\alpha} Z}{[1 + b_n (e^{-i\alpha} - 1)] [1 + B_n Z]} \right].$$

Adding and subtracting the summation  $\sum_{n=1}^N \frac{a_n (e^{-i\alpha} - 1)}{[1 + b_n (e^{-i\alpha} - 1)]}$ , we have

$$\begin{aligned}
R_{\alpha,N}(Z) &= e^{i\frac{\alpha}{2}} \left[ 1 + \sum_{n=1}^N \frac{a_n (e^{-i\alpha} - 1)}{[1 + b_n (e^{-i\alpha} - 1)]} + \sum_{n=1}^N \frac{a_n (e^{-i\alpha} - 1)}{[1 + b_n (e^{-i\alpha} - 1)] [1 + B_n Z]} - \right. \\
&\quad \left. \sum_{n=1}^N \frac{a_n (e^{-i\alpha} - 1)}{[1 + b_n (e^{-i\alpha} - 1)]} + \sum_{n=1}^N \frac{a_n e^{-i\alpha} Z}{[1 + b_n (e^{-i\alpha} - 1)] [1 + B_n Z]} \right].
\end{aligned}$$

Defining  $C_0 \equiv e^{i\frac{\alpha}{2}} \left[ 1 + \sum_{n=1}^N \frac{a_n (e^{-i\alpha} - 1)}{[1 + b_n (e^{-i\alpha} - 1)]} \right]$  we obtain

$$\begin{aligned}
R_{\alpha,N}(Z) &= C_0 + e^{i\frac{\alpha}{2}} \left[ \sum_{n=1}^N \frac{a_n (e^{-i\alpha} - 1) (1 - [1 + B_n Z])}{[1 + b_n (e^{-i\alpha} - 1)] [1 + B_n Z]} + \sum_{n=1}^N \frac{a_n e^{-i\alpha} Z}{[1 + b_n (e^{-i\alpha} - 1)] [1 + B_n Z]} \right], \\
&= C_0 + e^{i\frac{\alpha}{2}} \left[ \sum_{n=1}^N [-a_n B_n (e^{-i\alpha} - 1) + a_n e^{-i\alpha}] \cdot \psi \right],
\end{aligned}$$

where  $\psi = \frac{Z}{[1+b_n(e^{-i\alpha}-1)][1+B_nZ]}$ . Replacing  $B_n \equiv \frac{b_n e^{-i\alpha}}{1+b_n(e^{-i\alpha}-1)}$  in equation A.3, we can write

$$\begin{aligned} R_{\alpha,N}(Z) &= C_0 + e^{\frac{i\alpha}{2}} \left[ \sum_{n=1}^N \left[ \frac{a_n e^{-i\alpha} (1 + b_n (e^{-i\alpha} - 1)) - a_n b_n e^{-i\alpha} (e^{-i\alpha} - 1)}{1 + b_n (e^{-i\alpha} - 1)} \right] \cdot \psi \right] \\ &= C_0 + e^{\frac{i\alpha}{2}} \left[ \sum_{n=1}^N \left[ \frac{a_n e^{-i\alpha} [1 + b_n (e^{-i\alpha} - 1) - b_n (e^{-i\alpha} - 1)]}{1 + b_n (e^{-i\alpha} - 1)} \right] \cdot \psi \right] \\ &= C_0 + e^{\frac{i\alpha}{2}} \left[ \sum_{n=1}^N \frac{a_n e^{-i\alpha}}{1 + b_n (e^{-i\alpha} - 1)} \cdot \frac{Z}{[1 + b_n (e^{-i\alpha} - 1)][1 + B_n Z]} \right]. \end{aligned}$$

Moving the exponential factor into the summation and multiplying the denominator, this can be recast into the form

$$R_{\alpha,N}(Z) = C_0 + \sum_{n=1}^N \frac{a_n e^{-\frac{i\alpha}{2}}}{[1 + b_n (e^{-i\alpha} - 1)]^2} \cdot \frac{Z}{1 + B_n Z}.$$

Defining  $A_n \equiv \frac{a_n e^{-\frac{i\alpha}{2}}}{[1 + b_n (e^{-i\alpha} - 1)]^2}$ , we have the expression

$$\sqrt{1 + Z} \approx R_{\alpha,N}(Z) = C_0 + \sum_{n=1}^N \frac{A_n Z}{1 + B_n Z}.$$

Finally, using the Fourier transform  $\frac{\partial^2}{\partial x^2} \iff -k_x^2$  and defining  $X = \frac{v_{ref} k_x}{\omega}$ , the final expression is

$$\sqrt{1 - X} \approx R_{\alpha,N}(X) = C_0 - \sum_{n=1}^N \frac{A_n X}{1 - B_n X}, \quad (\text{A.3})$$

where

$$A_n \equiv \frac{a_n e^{-\frac{i\alpha}{2}}}{[1 + b_n (e^{-i\alpha} - 1)]^2}, \quad B_n \equiv \frac{b_n e^{-i\alpha}}{1 + b_n (e^{-i\alpha} - 1)},$$

and

$$C_0 \equiv e^{\frac{\alpha}{2}} \left[ 1 + \sum_{n=1}^N \frac{a_n (e^{-i\alpha} - 1)}{[1 + b_n (e^{-i\alpha} - 1)]} \right].$$